論文 / 著書情報
Article / Book Information

題目(和文)	MoOxで修飾したTiドープヒドロキシアパタイトの作製と光触媒活性
Title(English)	Preparation and photocatalytic activity of MoOx-modified titanium-doped hydroxyapatite
著者(和文)	JiraborvornpongsaNoppakhate
Author(English)	Noppakhate Jiraborvornpongsa
出典(和文)	学位:博士(工学), 学位授与機関:東京工業大学, 報告番号:甲第11284号, 授与年月日:2019年9月20日, 学位の種別:課程博士, 審査員:中島 章,宮内 雅浩,松下 伸広,生駒 俊之,松下 祥子
Citation(English)	Degree:Doctor (Engineering), Conferring organization: Tokyo Institute of Technology, Report number:甲第11284号, Conferred date:2019/9/20, Degree Type:Course doctor, Examiner:,,,,
学位種別(和文)	博士論文
Type(English)	Doctoral Thesis

Preparation and photocatalytic activity of MoO_x-modified titanium-doped hydroxyapatite

MoO_xで修飾したTiドープヒドロキシアパタイトの作製と光触媒活性

Department of Materials Science and Engineering

School of Materials and Chemical Technology

Tokyo Institute of Technology

Noppakhate Jiraborvornpongsa

Abstract

Titanium-doped hydroxyapatite (Ti-HAp) powders were modified with Mo-based solutions ($CaMoO_4$ or $MoO_2(C_5H_8O_2)_2$). The photocatalytic activity under UV illumination was evaluated by decomposition of gaseous 2-propanol (IPA). The crystal structure, morphology, light absorption, and specific surface area were almost identical after the modification, but the small MoO_x clusters were deposited on Ti-HAp surface. The photocatalytic activity of MoO_x-modified Ti-HAp samples increased concomitantly with increasing Mo concentration. The highest photocatalytic activity of MoO_x-modified Ti-HAp was about 13 times higher than that of Ti-HAp. The signal appearance of Mo(V) in electron spin resonance spectra and the decrease of photoluminescence intensity indicate that the electrons in Ti-hybridized band transfer to the MoO_x cluster, which suppresses recombination of the photoinduced electron and hole pairs, and provides higher photocatalytic activity.

Table of contents

CHAPTER 1

Introduction

1.1. Photocatalyst (Titanium dioxide, TiO_2)

1.1.1. Photocatalytic reaction

Photocatalytic materials have received more attentions in recent years because of its applications in environmental purification which is a promising approach to eliminate various volatile organic compounds (VOCs), organic wastewater, and bacteria by utilizing photon energy.

Photocatalytic reaction is the catalysis of a photochemical reaction at a solid surface, usually a semiconductor. Semiconductor is useful as a photocatalyst because of a favorable electronic structure, light absorption properties, change transfer characteristics, and excited-state lifetime [1, 2]. There is an energy gap exists between the top of filled valence band (VB) and the bottom of the empty conduction band (CB), which is called the bandgap. The electron transfer between these bands can occur by absorption of photon energy equal or higher than the bandgap energy of photocatalyst, the electrons (e^-) in the valance band are excited to the conduction band while the photoinduced holes (h^+) are generated in the valence band. The photoinduced electron and hole pairs can recombine with each other or transfer to electron donor or electron acceptor on the photocatalyst surface from solution or gas phase contact. Therefore, the photocatalytic reaction is usually a heterogeneous reaction. There must be at least two reactions occurring simultaneously, the first reaction involving oxidation from the photoinduced holes in the valence band, and the second reaction involving reduction from the photoinduced electrons in the conduction band as shown in **Fig. 1.1** [3]. The both reactions must be balanced in order for the photocatalyst itself not undergo change. For the

oxidation reaction, the potential of electron donor species should be more negative than that of the valence band of photocatalyst, whereas the reduction reaction, the potential of electron acceptor should be more positive than that of the conduction band of photocatalyst. For the general case, the photocatalytic reaction can be written as following [4]:

$$\text{Photocatalyst} + h\nu \rightarrow e^- + h^+ \quad (1)$$

The adsorbed oxygen on photocatalyst surface prevents the recombination of the photoinduced electron and hole pairs by trapping the photoinduced electrons. Superoxide radicals ($O_2^{\bullet-}$) are formed.

$$O_2 + e^- \rightarrow O_2^{\bullet-} \quad (2)$$

It is likely that H_2O_2 is formed from $O_2^{\bullet-}$ via perhydroxyl radical ($HO_2^{\bullet}$) according to the following reactions.

$$O_2^{\bullet-} + H^+ \rightarrow HO_2^{\bullet} \qquad pK_a = 4.88 \quad (3)$$

$$HO_2^{\bullet} + HO_2^{\bullet} \rightarrow H_2O_2 + O_2 \quad (4)$$

$$O_2^{\bullet-} + HO_2^{\bullet} \rightarrow O_2 + HO_2^- \quad (5)$$

$$HO_2^- + H^+ \rightarrow H_2O_2 \qquad pK_a = 1.5 \times 10^{-12} \quad (6)$$

On the other hand, the photoinduced holes react with either H_2O or OH^- adsorbed on the photocatalyst surface to give hydroxyl radical ($^{\bullet}OH$).

$$H_2O + h^+ \rightarrow {}^{\bullet}OH + H^+ \quad (7)$$

$$OH^- + h^+ \rightarrow {}^{\bullet}OH \quad (8)$$

These reactive oxygen species (ROS) may also contribute to the oxidative pathways such as the degradation of a pollutant due to their strong oxidation potential.

$$^{\bullet}OH + \text{pollutant} \rightarrow CO_2 + H_2O \quad (9)$$

$$HO_2^{\bullet} + \text{pollutant} \rightarrow CO_2 + H_2O \quad (10)$$

$$O_2^{\bullet-} + \text{pollutant} \rightarrow CO_2 + H_2O \quad (11)$$

The efficiency of the photocatalytic reaction is measured as a quantum yield which is defined as the number of reactions occurring per absorbed photon. It is difficult to measure the actual absorbed photon in heterogeneous system due to the scattering of light by photocatalyst surface. Usually, it is assumed that all photon is absorbed and the efficiency is quoted as an apparent quantum yield. If several products are formed from the photocatalytic reaction then the efficiency is sometimes measured as the yield of a particular product.

The ability of photocatalyst to undergo the photoinduced electron transfer to adsorbed species on its surface is governed by the band energy positions of photocatalyst or the redox potentials of the adsorbate. As mentioned above, the potential of electron donor species should be more negative than that of the valence band of photocatalyst in order to donate an electron to the vacant hole, whereas the potential of electron acceptor should be more positive than that of the conduction band of photocatalyst in order to accept an electron from the conduction band. The band edge positions of various semiconductors are presented in **Fig. 1.2** [3]. The internal energy scale is given on the left for comparison to the vacuum level and on the right for comparison to normal hydrogen electrode (NHE). The positions are derived from the flat band potentials in a contact solution of aqueous electrolyte at pH = 1. The pH of solution influences the band edge potentials of various photocatalysts compared to the redox potential for the adsorbate.

Quantum size effects occur for semiconductor particles on the order of 1–10 nm in size [3, 5]. The range of size for quantum size effect is dependent on the effective mass for semiconductor. The electron and hole produced in quantum size particles are confined in a potential well of small geometrical dimensions. The electron and hole do not experience the electronic delocalization present in a bulk semiconductor possessing the conduction band and the valence band. Instead, the confinement produces a quantization of discrete electronic

states and increases the effective bandgap of the semiconductor. Such effect can change the color of material and the photocatalytic properties.

1.1.2. Titanium dioxide photocatalyst

Titanium dioxide (TiO_2) is one of the most famous photocatalyst due to high photo-activity, low cost, low toxicity, good thermal stability and good chemical stability. Titanium dioxide exists as three different polymorphs: rutile (tetragonal), anatase (tetragonal), and brookite (orthorhombic). The most stable phase of TiO_2 is rutile. Typically, the metastable phase of anatase and brookite will transform to the thermodynamically stable rutile phase upon calcination at temperature higher than ca. 600°C [6]. In their structure, titanium atoms are coordinated to six oxygen atoms, forming TiO_6 octahedra. In rutile structure, the TiO_6 octahedra share edges at (001) planes to give a tetragonal structure (**Fig. 1.3(b)**), and in anatase structure, the TiO_6 octahedra share corners which form (001) planes (**Fig. 1.3(a)**) resulting in a tetragonal structure. For brookite structure, both edges and corners are shared to give an orthorhombic structure (**Fig. 1.3(c)**). The Ti–O bonding lengths of anatase are shorter than those of rutile. These differences in lattice structure cause difference in electronic structure among these polymorphs. The bandgap energy is 3.0 eV for rutile, 3.2 eV for anatase, and ~3.2 eV for brookite.

In photocatalytic reaction of TiO_2, when TiO_2 absorbs light of energy greater than the bandgap of TiO_2 ($\lambda \leq 380–400$ nm, UV range), the electrons in the valence band are excited to the conduction band generating positive holes in the valence band. The photoinduced electron and hole pair can be trapped as Ti^{3+} and O^- defect sites in TiO_2 lattice, or they can recombine with each other [7]. The photoinduced electron and hole pairs can migrate to the surface and initiate redox reactions with adsorbates (**Eq. 2–11**). These reactions may also contribute to the

oxidative pathways such as the degradation of a pollutant [8, 9]. Based on this property, TiO_2 can be used for environmental purification of organic waste in both gas phase and liquid phase [10, 11]. It can be applied into many applications as following.

In case of indoor air purification, the concentrations of individual VOCs are in the order of 0.1 parts per million by volume (ppmv), and that the total concentration of VOCs is around 0.5–2.0 ppmv [12]. Various VOCs such as formaldehyde, acetaldehyde, aromatic compounds, and hydrocarbon can be decomposed by the photocatalytic reaction of TiO_2. In general, the size of an average indoor facility is usually too large to rely on diffusion or natural convection. For the practical usage, the air purifier systems contain an air pump, a particulates filter, a light source, and a photocatalyst employed on a substrate (**Fig. 1.4**) that bring the contaminated air to the photocatalyst surface [13]. For outdoor air purification, the type of contaminants is different from indoor air purification (less VOCs and more NO_x, CO, SO_x). The photocatalyst can be applied in various forms such as cementitious modules (blocks) and over-coated thin layers. For TiO_2-coated surface, it can be used for both outdoor air purification and self-cleaning, which prevent the adsorption of soot or dust that tend to stick to the surface.

Regarding water purification, the operation needs to be performed at room temperature or pressure, complete mineralization without secondary pollution, repetitive cycles and low costs for operations. The photocatalytic reaction of TiO_2 can decompose most of organic compounds due to its strong oxidation power [4, 14, 15]. For the slurry of fine particle TiO_2, it provides high decomposition rate of organic compounds due to the high amount of TiO_2 active sites. However, the slurry of TiO_2 requires an additional process to separate TiO_2 powder from treated water [16]. To overcome this problem, TiO_2 was immobilized onto various substrate [17–19]. The good supporting material for TiO_2 should have the following

properties; transparent to UV light, favor strong chemical or physical bonding to TiO_2 particles, high specific surface area, good adsorption capability, favor the liquid–solid separation, and chemically inert [19]. However, the immobilized TiO_2 on supporting material may encounter various problems such as low photocatalytic activity due to low active sites and loss of deposited TiO_2 layer over time. To prevent the problems associated with immobilized TiO_2, a photocatalytic reactor membrane pilot is used [20]. **Figure 1.5** shows the schematic diagram of photocatalytic reactor pilot. Firstly, water enters the unit (Point 1), it is passes through a prefilter consisting of both a bag (Point 2) and cartridge filter (Point 3) having a nominal pore size of 10 μm. Then it is mixed with nanoparticle TiO_2 slurry (Point 5), and pass through the reactor (Point 6) with UV lamps. The unit's flow-through design is enabled by a TiO_2-recovery system. After exposure to the UV lamps, a cross-flow ceramic membrane (Point 8) removes TiO_2 particles from the flow stream and the treated water exits the unit (Point 9). Every 60 s the membrane is back-pulsed to prevent catalyst buildup. The rejected TiO_2 is mixed with influent (Point 5) prior the UV reactor. Thus, the unit recycles and reuses all of the TiO_2 particle, allowing for long-term operation.

The photocatalytic reaction of TiO_2 has been applied for antibacterial [21–27]. It was reported that various bacteria such as *E. Coli.* can be decomposed by photocatalytic reaction of TiO_2 under UV illumination. Two different photochemical processes are proposed which kill the bacteria for TiO_2 system. The first is the direct reaction between TiO_2 and the cells. It is noteworthy that the photoinduced hole has strong oxidation power. Therefore, it is expected that the cells are directly oxidized by the photoinduced holes in the valence band of TiO_2. The other process is the indirect reaction between TiO_2 and the cells. The reactive oxygen species are generated from water or oxygen (**Eq. 2–8**). These reactive oxygen species may attack the cell membrane and cellular components. From **Fig. 1.6**, the initial reaction is a partial

decomposition of the outer membrane resulting in the changes of permeability to these reactive oxygen species. The outer membrane enables radicals to reach the cytoplasmic membrane, leading to the peroxidation of membrane lipid. The structural and functional disorders of the cytoplasmic membrane due to lipid peroxidation lead to the loss of cell viability and cell death.

Titanium dioxide processes the photocatalytic hydrophilic surfaces by utilizing photon energy to decompose the dirt and other contaminations so called self-cleaning [28–32]. Under UV illumination, the water contact angle of TiO_2 surface can decrease to 0°, which is lower than the initial contact angle (ca. 30°), indicating that TiO_2 possesses highly hydrophilic property. The changes in wettability can be observed for both anatase and rutile TiO_2 irrespective to their photocatalytic activity. The photoinduced hydrophilicity of TiO_2 is attributed to some structural changes at the surface [30, 31], which is different from the photocatalytic reaction process. The photoinduced electron and hole pairs can lead to the reduction and oxidation of TiO_2 surface itself. The photoinduced electron tend to reduce Ti^{4+} ions to Ti^{3+} ions. On the other hand, the photoinduced holes react with the bridging site oxygen resulting in oxygen vacancy. The produced oxygen vacancies are favorable for water adsorption as shown in **Fig. 1.7**. Water molecules are adsorbed on defect sites to form singly coordinated or doubly coordinated surface hydroxyls, resulting in a highly hydrophilic surface is formed.

The water splitting of TiO_2 was firstly reported by Honda-Fujishima [33]. The photoinduced electron and hole pairs cause redox reactions similarly to electrolysis. Water molecules are reduced by the photoinduced electrons to form H_2, and oxidized by the photoinduced holes to form O_2 for overall water splitting [34, 35]. The width of the bandgap energy and the level of the conduction band and the valence band are important factors for

water splitting. The potential of the conduction band has to be more negative than the redox potential of H^+/H_2 (0 V vs. NHE), while the potential of the valence band has to be more positive than the redox potential of O_2/H_2O (1.23 V vs. NHE) as shown in **Fig. 1.8**. Efficiently water splitting into usable hydrogen could become a new industrial photosynthesis that would provide clean fuel which utilizes only water.

1.1.3. Advantages and drawbacks of photocatalysis for environmental purification by TiO_2

Titanium dioxide photocatalyst has been used in many applications as described above. It has strong oxidation power for decomposition most of organic pollutants. It also possesses superhydrophilicity, chemical stability, long durability, nontoxicity, low cost, and transparent to visible.

However, its application is limited because of various reasons [36, 37]. Firstly, TiO_2 has narrow light absorption range ($\lambda < 400$ nm, UV range), which is a small fraction (< 5%) of incident solar light and indoor light due to its wide bandgap (3.2 eV for anatase, 3.0 eV for rutile). Moreover, the photocatalytic degradation mainly occurs on the surface of TiO_2, mass transfer limitation has to be minimized for effective TiO_2 application in water treatment. It also has poor affinity against organic pollutants (especially the hydrophobic organic pollutants), which provides low photocatalytic degradation rates. During the photocatalytic degradation process, TiO_2 particles may undergo aggregation due to the instability of nanosized particle, resulting in lower activated sites consequently reduce its photocatalytic activity. For water treatment, it is noteworthy that small particles show high scattering, which can reduce their photocatalytic activity compared to larger particles. Furthermore, for water treatment, the nanosized TiO_2 particles are difficult to separate or recovery from the treated

water for both economic concern and safety concern. To overcome those limitations of TiO_2-based photocatalyst, various techniques have been applied onto TiO_2, which will be discussed in detail in the following sections.

1.1.4. Historical overview on the environmental purification by TiO_2

In previous, TiO_2 powder has been commonly used as white pigments. It is low cost, chemically stable, non-toxicity, and has no absorption in visible range. However, there was a chalking phenomenon occurred when using TiO_2 as a white pigment in organic paint, leading to the discover of photocatalytic degradation of TiO_2 [38].

In 1972, Honda and Fujishima reported the efficient hydrogen production from water by photocatalysis [33]. Thus, TiO_2 photocatalysis drew attention of many scientists as one of the promising method to obtain the new energy source. However, the reaction efficiency was very low because TiO_2 can absorb only UV light which is less than 5% in solar light. Kawai and Sakata [39] reported that the water photolysis could not proceed effectively in the powder system. Moreover, the produce H_2 and O_2 might recombine to regenerate water molecules because the production sites of H_2 and O_2 gases are located close to each other [39]. Therefore, TiO_2 photocatalysis is not very attractive for H_2 production technology. Recently, various novel photocatalyst materials have been studied for water splitting and H_2 production instead of TiO_2 [34]. On the other hand, the studies of TiO_2 powders have changed the direction to the utilization of the strong oxidation power of TiO_2 to decompose various organic pollutants both water and air in the 1980s [40]. Thus, the reduction reaction was not necessarily H_2 production anymore. Now, both the reduction and oxidation sites are located on the TiO_2 surface, and the reduction of adsorbed oxygen molecules also proceeds on the TiO_2 surface.

The immobilization of TiO_2 powders on supports was carried out to extend the practical

usage application. By coating TiO_2 powder onto the supports, the amount of usage TiO_2 powders decrease and the coated TiO_2 surface remains clean under UV illumination. For example, TiO_2 powder were coated on a ceramic tile or glass [41]. The coated substrates will have self-cleaning property. In Japan, the self-cleaning cover glass were used for tunnel light, which UV light was emitted from a sodium lamp that is sufficient to keep the cover glass surface clean.

By coating TiO_2 on the substrate also provides antibacterial property under UV illumination. The antibacterial property of TiO_2 powder is enhanced by the aid of either silver or copper [42], which is harmless to human body. The antibacterial ceramic tile coated with TiO_2 containing silver or copper was firstly manufactured by TOTO Ltd. in 1995.

During the studies of self-cleaning materials coated with TiO_2 film, the photoinduced hydrophilicity of TiO_2 was discovered. The change in the water wettability of TiO_2 surface before and after UV illumination leads to the new application range of TiO_2. Another application with assistance from photoinduced hydrophilicity is the anti-fogging function. The fogging of the mirror or glass surface occurs when steam cools down on these surfaces to form many water droplets, resulting in the high light scattering. On a hydrophilic surface, no water droplet is formed. There is only a uniform thin water film formed on the surface. This uniform water film prevents the fogging. This application was applied for side-view mirrors of Japanese-made cars.

Until today, the studies of photocatalyst is still being developed. There are many challenges to improve the practical usage of photocatalyst. One of the most challenging study is to achieve the high performance of photocatalyst that will be discussed in next sections.

1.1.5. Research on the high performance photocatalyst

1.1.5.1. Phase mixture or vacancy control of TiO_2

Ohno *et al*. reported the effects of mixing anatase and rutile phases of TiO_2 [43, 44]. It is noteworthy that anatase phase of TiO_2 has higher photocatalytic activity than that of rutile phase. The TiO_2 powder (Degussa, P-25), which is a standard photocatalyst, contains anatase and rutile phases in a ratio of about 3 : 1. By mixing both anatase and rutile phases of TiO_2, they show higher photocatalytic activity than that of pure anatase or rutile. Under UV illumination, the photoinduced electrons can transfer between anatase and rutile while the photoinduced holes can transfer between anatase and rutile, which suppresses the recombination of the photoinduced electron and hole pairs.

Nakamura *et al*. investigated the role of oxygen vacancy in TiO_2 [45]. By the plasma treatment, the oxygen vacancies were form in the TiO_2 structure. The plasma-treated TiO_2 exhibited higher light absorption in visible range. The oxygen vacancy states in anatase TiO_2 were determined to be located 2.02–2.45 eV above the valence band. Under visible illumination, the electrons in the valence band can be excited to the oxygen vacancy states. The plasma-treated TiO_2 showed photocatalytic activity for NO removal under visible illumination.

1.1.5.2. Other element doping

Mechanisms of photocatalytic activity of pure TiO_2 and ion-doped TiO_2 are presented in **Fig. 1.9** [46]. The visible light photocatalytic activity of ion-doped TiO_2 can be explained by a new energy level located in the bandgap of TiO_2 by dispersion of dopants in the TiO_2 structure. The electrons can be excited either from the defect state to the conduction band, or the electrons can be excited from the valence band to the defect state.

1.1.5.2.1. Metal doping

Choi *et al*. have prepared metal ion doping in quantum size TiO_2 [47]. Various metal ions

have been investigated. Their photocatalytic activity and the transient charge carrier recombination dynamics of doped-TiO_2 were measured. Doping with Fe^{3+}, Mo^{5+}, Ru^{3+}, Os^{3+}, Re^{5+}, V^{4+}, and Rh^{3+} at 0.1–0.5 atomic % significantly increases the photocatalytic activity for both oxidation and reduction while doping with Co^{3+} and Al^{3+} decreases the photocatalytic activity. The photocatalytic activities are shown to increase with the concentration of trapped charge carriers that remain after an initial fast recombination of the photoinduced electron and hole pairs. The influences of doping metal ions depends on whether it serves as a mediator of interfacial charge transfer or as a recombination center. The ability of a dopant to function as an effective trap is related to the dopant concentration, the energy of dopants within the TiO_2 lattice, their d electronic configuration, the distribution of dopants within the particles, the electron donor concentration, and the incident light intensity. Enhanced interfacial charge transfer in the presence of effective dopants appears to be the most important factor in enhancement of photocatalytic activity of doped TiO_2.

Wilke and Breuer investigated the influence of transition metal doped TiO_2 [48]. Either Cr^{3+} or Mo^{5+} ions have been doped into anatase phase of TiO_2. The bandgap energy of Cr-doped TiO_2 and Mo-doped TiO_2 decreased to 2.00 and 2.85 eV, respectively at dopant concentration of 0.1 atomic%. However, the charge carrier lifetimes of Cr-doped TiO_2 and Mo-doped TiO_2 were shorter than that of pure TiO_2 because the doped transition metals act as recombination centers. The adsorption capability of Mo-doped TiO_2 against Rhodamine B markedly increased due to the five-fold positive charge on Mo^{5+}, there is a strong electrostatic interaction with the dye. Whereas Cr-doped TiO_2 had poor adsorption capability same as pure TiO_2. The photocatalytic degradation of Rhodamine B rates for both Cr-doped TiO_2 and Mo-doped TiO_2 were lower than that of pure TiO_2 due to the shorter charge carrier life time.

Doping with transition metals has shown both positive and negative effects. Although

transition metal doping decreases the bandgap energy of TiO_2, the doping metal ions also act as recombination centers for the photoinduced electron and hole pairs, resulting in the lower overall photocatalytic activity.

1.1.5.2.2. Nonmetal doping

The studies of C-doped TiO_2 have been investigated by many scientists [49–51]. The C-doped TiO_2 shows light absorption in visible range. It also has high visible light photocatalytic activity compares with pure TiO_2. It is considered that the bandgap narrowing was occurred in C-doped TiO_2. The top of the valence band shifted toward the negative potential which lower the oxidation power of C-doped TiO_2. The energy level of interstitial C atom is localized between the valence band and the conduction band of TiO_2, resulting light absorption in visible range.

Umebayashi *et al*. synthesized S-doped TiO_2 by oxidation annealing of TiS_2 [52]. After annealing at 600°C, TiS_2 turned into anatase phase of TiO_2. The residual S atoms occupied at O atom sites in TiO_2 to form Ti–S bonds. The doping S caused the light absorption in visible range. Based on the theoretical calculation, mixing of the S 3p states with the valence band (O 2p) was found to contribute the bandgap narrowing. The oxidation state of S atoms is determined to be S^{2-}. On the other hand, Ohno *et al*. prepared S-doped TiO_2 and investigated photocatalytic degradation of methylene blue (MB) and 2-propanol (IPA) [53, 54]. They have synthesized modified TiO_2 powder in which S^{4+} ion substitutes for Ti^{4+} ion in the structure. The S-doped TiO_2 showed light absorption in visible range and high photocatalytic degradation of MB and IPA under visible illumination at wavelength longer than 440 nm. From XPS, the oxidation state of S atoms incorporated into the TiO_2 particles is determined to be mainly S^{4+}. Ho *et al*. reported that the oxidation state of S-dopant is dependent on the preparation routes [55]. In case of Umebayashi, most of the sulfur in TiS_2 was oxidized and

the residual sulfur would naturally remain as S^{2-}. On the other hand, Ohno used titanium tetraisopropoxide and thiourea as the titanium and sulfur precursors, the substitution of Ti^{4+} by S^{6+} would be chemically more favorable than replacing O^{2-} with S^{2-}.

Many scientists have reported that N-doped TiO_2 shows photocatalytic activity in various reactions under visible illumination [56–60]. The energy level of doped N ions (N 2p) is localized slightly above top of the valence band of TiO_2 (O 2p), resulting in lower bandgap energy. Under visible illumination, the electrons in localized N 2p level can be excited to the conduction band of TiO_2. However, the effects of N-doping are different between anatase and rutile because of different structures and densities. In case of anatase, N-doping provides a redshift due to the mixing of N 2p and O 2p states. On the other hand, in case of rutile, N-doping provides a blueshift because the shift of the top of the valence band towards lower energies leads to an increase of the bandgap energy [59].

1.1.5.3. Hybridization with different materials

1.1.5.3.1. Hybridization with high adsorption materials

Due to the low adsorption capability of TiO_2, it was impregnated on three different types of adsorbents, mesoporous (MCM-41), microporous (β-zeolite), and pillared structure (montmorillonite) where different loading amounts (10–80 wt%) of TiO_2 were obtained using sol–gel method. The photocatalytic activity of supported TiO_2 on three types of adsorbents was compared with that of bare TiO_2 prepared by sol–gel method and commercial Degussa P-25 [61]. The supported TiO_2 showed significantly higher photodegradation rate of orange II than that of bare TiO_2 both sol–gel method and P-25. The performance improvement can be attributed to the high specific surface areas of adsorbents. In case of montmorillonite supported TiO_2, it has the highest adsorption capability due to the interlayer surface of the pillared clay is hydrophobic and facilitate the adsorption of organics, and shape selectivity

because of its pore structure. The slight differences among these adsorbents are due to the nature of the substrate used.

Gao *et al*. prepared TiO_2 supported on activated carbons (TiO_2/AC) [62]. The adsorption and photodegradation of Acid Red 88 (AR) were compared with bare TiO_2. The TiO_2/AC composites exhibited higher efficiency for photodegradation of AR than that of bare TiO_2 because of the enrichment of target molecules around TiO_2 by adsorption from AC. In TiO_2/AC composite system, AC promotes mass transfer of the target pollutant to the surface of TiO_2, reduces the detrimental effects of matrix ionic species such as anions which can deactivate TiO_2, disperses TiO_2 particles which prevents their agglomeration, and enable easy separation of the micron-size TiO_2/AC from treated water.

The studies of TiO_2 and hydroxyapatite (HAp) composite revealed that it promoted the photocatalytic activity of TiO_2 due to the higher adsorption capability [63, 64]. It is noteworthy that HAp possesses high affinity against organic compounds. The high adsorption capability of HAp enhances the possibility of target molecules to contact with TiO_2 surface, resulting in higher photocatalytic activity.

1.1.5.3.2. Hybridization with other photocatalysts (Z-scheme)

Z-scheme photocatalysts are named as their charge transfer mechanism is similar to natural photosynthesis in green plants, in which the charge transfer pathway involves a two-step photoexcitation that resembles the English letter "Z" as shown in **Fig. 1.10** [65]. The valence band potential and the conduction band potential of PS I are more negative than those of PS II. The photoinduced electron in PS II, which have low reduction potential, will recombine with the photogenerated holes in PS I, which have low oxidation potential. Thus, the photoinduced electrons in the conduction band of PS I and the photoinduced holes in the valence band of PS II can remain their respective potential to achieve the charge separation

and optimize the redox ability of the photocatalytic reaction. The migration of electrons from the conduction band of PS II to the valence band of PS I is thermodynamically favored by the electrostatic attraction. The direct Z-scheme system provides higher photocatalytic activity due to the charge separation. Yu *et al*. reported the enhanced photodegradation of formaldehyde by Z-scheme g-C_3N_4-TiO_2 photocatalysts [66]. They successfully introduced g-C_3N_4 nanoparticles onto TiO_2 (P-25) particles. The g-C_3N_4-TiO_2 photocatalyst showed higher decomposition rate of formaldehyde under UV illumination than that of TiO_2 due to higher charge separation from Z-scheme. However, when the content of introduced g-C_3N_4 exceeds a critical value, the photocatalytic activity significantly decreases. The g-C_3N_4 will cover TiO_2 resulting in lower photon energy in TiO_2. Also, the photoinduced holes cannot transfer to the surface of g-C_3N_4-TiO_2 composite and the surface of g-C_3N_4 layer will become the recombination center.

1.1.5.3.3. Hybridization with metal oxide cluster

To obtain visible light sensitive photocatalyst, Irie *et al*. have proposed an idea of direct electron transfer from the valence band composed of O 2p orbitals to the metal ions atomically grafted on the oxide surface via visible illumination [67–70]. This electron transfer corresponds to a type of interfacial charge transfer (IFCT) between the discrete energy levels of molecular species and the continuous ones of solids. They have prepared metal cluster grafted TiO_2 using simple impregnation method by soaking rutile phase of TiO_2 into $CuCl_2{\cdot}2H_2O$ or $FeCl_3{\cdot}6H_2O$ aqueous solution. The metal oxide cluster with size of few nanometer was formed on the surface of TiO_2. Under visible illumination, the electrons in the valence band are directly excited to reduce the metal ions on the surface while the photoinduced holes are formed in the valence band. In case of TiO_2, the valence band of is composed of O 2p orbitals which has the potential of 3.04 V. Therefore, the photoinduced

holes have strong oxidation power which can decompose most of organic compound. The photoinduced electrons can reduce oxygen depend on its redox potential. The redox potential of Cu(II)/Cu(I) is E^0 = 0.16 V (vs. SHE, pH = 0) [67], and the redox potential of Fe(III)/Fe(II) is E^0 = 0.771 V (vs. SHE, pH = 0) [70], which are more positive than that of one-electron oxygen reduction ($O_2 + H^+ + e^- \rightarrow HO_2^\bullet$, -0.046 V vs SHE, pH = 0) as shown in **Fig. 1.11**. Thus, the oxygen reduction is expected to proceed via multielectron reduction which has more positive potential than that of Cu(II)/Cu(I) or Fe(III)/Fe(II). Additional reports have revealed that the direct electron transfer via IFCT is more effective for rutile than anatase [69].

Tada *et al*. have investigated the chemisorption calcination cycle (CCC) technique, by which chemical bond adsorb metal complex. Additionally, the organic (ligand) part is oxidized by post-heating to prepare metal oxide cluster or ultrathin film at a molecular scale [71–74]. They prepared Fe-modified TiO_2 by CCC technique using P-25 as a TiO_2 source [73]. The visible photocatalytic activity was obtained due to the excitation from the surface d sub-band, yielded by mixing between the surface Fe(III) levels and O 2p by the Ti–O–Fe interfacial bond, to the conduction band of TiO_2 via IFCT mechanism. The photoinduced holes generated in the surface d sub-band take part in the oxidation process, while the photoinduced electrons in the conduction band effectively reduce oxygen. From XPS analysis, it revealed that after Fe-modification by CCC technique, the O 2p valence band position rises to more negative value suggesting that the mixing between the surface Fe(III) levels and O 2p by the Ti–O–Fe interfacial bond as shown in **Fig. 1.12**. However, the rise of the valence band top leads to the lower oxidation power of TiO_2.

1.2. Hydroxyapatite (HAp)

1.2.1. Crystal structure of HAp

Hydroxyapatite (HAp, $Ca_{10}(PO_4)_6(OH)_2$) has two possible structures [75–80]. It can be either monoclinic ($P2_1/b$) or hexagonal ($P6_3/m$) depends on the nature of the order/disorder of OH^- ions along the *c*-axis from one formula unit to the next. The stoichiometry structure of HAp is a monoclinic. Due to the lattice deficiencies, hexagonal phase is the most common structure for HAp as shown in **Fig. 1.13**. One unit cell of hydroxyapatite crystal is composed of six PO_4^{3-} groups surrounded by ten calcium atoms with two OH^- ions located along the *c*-axis. The oxygen atoms have three different environments (O1, O2, and O3). The calcium atoms are separated into two different positions. The first calcium positions (Ca1), consist of four calcium atoms, are columnar site parallel to the *c*-axis which have ionic bond with the PO_4 groups via O1 and O2 atoms. Each Ca1 atom is surrounded by nine oxygen atoms (three O1, three O2, and three O3). The second calcium positions (Ca2), consist of six calcium atoms, form equilateral triangles centered at the unit cell corners. Each Ca2 atom is surrounded by seven oxygen atoms (one O1, one O2, four O3 and one OH^- ion). The large size of the Ca2 triangle allow motion of the hydroxyl ion along the column axis [79].

1.2.2. Ion exchange

Due to a complicated structure of HAp, various cations such as lead, copper, zinc, and cadmium can be introduced into the crystal structure of HAp by ion exchange mechanism [81–85]. There are two possible ion exchange mechanisms have been proposed. The first mechanism is the adsorption of cations on the HAp surface, followed by ion exchange reaction between adsorbed cations and Ca^{2+} ions of HAp. For example, in case of ion exchange of Pb^{2+} ions [83], the ion exchange mechanism is expressed as:

$$Ca_{10}(PO_4)_6(OH)_2 + xPb^{2+} \rightarrow xCa^{2+} + Ca_{10-x}Pb_x(PO_4)_6(OH)_2 \qquad (12)$$

The second mechanism is dissolution-precipitation mechanism which is the dissolution of

HAp in aqueous solution containing cations, followed by precipitation of new compound. The dissolution-precipitation mechanism is revealed as:

Dissolution: $Ca_{10}(PO_4)_6(OH)_2 + 14H^+ \rightarrow 10Ca^{2+} + 6H_2PO_4^- + 2H_2O$ (13)

Precipitation: $10Pb^{2+} + 6H_2PO_4^- + 2H_2O \rightarrow Pb_{10}(PO_4)_6(OH)_2 + 14H^+$ (14)

Additionally, the oxyanions such as CO_3^{2-}, VO_4^{3-}, and SO_4^{2-} can replace structural PO_4^{3-} groups and anions such as F^- and Cl^- can exchange with OH^- ions [86, 87]. Based on this property of HAp, the ion exchange of various ions into the HAp structure have been studies [88–92].

1.2.3. Adsorption capability

Hydroxyapatite has been reported that it has high adsorption capability and high affinity against organic compounds. Kresak *et al.* reported the adsorption of amino acids onto HAp [93]. Four different acidic amino acids (L-Aspartic acid, L-Glutamic acid, DL-α-amino adipic acid, and DL-α-amino pimelic acid) have been investigated. The affinity of four different amino acids are very similar, indicating that similar functional groups (carboxyl groups) in the amino acids and the adsorption sites (calcium ions) in the HAp structure are involved in the adsorption phenomenon. They have assumed that the amino acid molecules are anchored to the HAp surface by their terminal carboxyl groups attached to the calcium ions belonging to the HAp surface by the electrostatic attraction force. Luo and Andrade investigated the adsorption of proteins on HAp powder [94]. The adsorption of lysozyme, albumin, transferrin, and lactoferrrin onto HAp powders suggested the calcium sites can bind with carboxyl groups in protein, but the affinity of the negative charge in PO_4^{3-} site for NH_3^+ in proteins is not high. So, the affinity of the calcium site for negative charge (carboxyl groups) is larger than that of PO_4^{3-} site for positive charge (NH_3^+). These properties of HAp make protein adsorption onto

HAp complicated.

Lin *et al*. studied the adsorption of phenol from aqueous solution on HAp [95]. The adsorption of phenol on HAp powders was also investigated at different initial pH between 2 and 11. The maximum adsorption capacity of phenol on HAp powder was at pH 2. The adsorption capacity decreased with increasing pH up to 8.2 then increased with further increasing pH to alkaline value. The surface potential of HAp became positive at low pH values by surrounded hydrogen ions. Then, phenol was adsorbed through attractive force between surrounded hydrogen ions on HAp and the aromatic ring of phenol [96]. At high pH values, the phenol would be ionized in the solution resulted in the increasing of ionic strength, which increased the adsorption capacity [97].

Berry and Siragusa examined the adsorption of bacteria on HAp [98]. Since most bacteria are negatively charged, the adsorption of bacteria on HAp appears to be similar to the adsorption of negatively charged proteins. The negatively charged bacteria is adsorbed to the positively charged calcium ions of HAp by the electrostatic attraction force.

Kawai *et al*. reported the removal of gaseous formaldehyde by HAp layer on polyamide film [99]. The adsorption of gaseous formaldehyde was compared among three samples; HAp deposited on polyamide, activated charcoal, and calcined HAp powder. The decrease in concentration of formaldehyde was in the order of calcined HAp < activated charcoal < HAp deposited on polyamide. The different of adsorption capacity between HAp deposited on polyamide and calcined HAp powder corresponded to the higher specific surface area of HAp deposited on polyamide. Despite the higher specific surface area of activated charcoal, the adsorption capacity of activated charcoal was lower than that of HAp deposited on polyamide due to the difference in the number of activated site available for the adsorption of formaldehyde. It is noteworthy that formaldehyde is easily adsorbed by adsorbents possessing

a polar surface. The hydroxyl group of HAp may play an important role in adsorption of gaseous formaldehyde [100].

1.2.4. Photocatalytic activity of HAp

Stoichiometric defect-free HAp is not a good electrical conductor. Tsukada *et al*. reported that HAp has band gap energy more than 6 eV [101]. Due to its wide band gap, HAp does not possess photocatalytic activity under UV light or visible light. However, the presence of either defects or dopants in HAp structure can change the electronic structure of HAp leading to the lower band gap energy. Therefore, HAp can possess photocatalytic activity. Nishikawa *et al*. reported that HAp powder heated at 200°C effectively decomposed methyl mercaptane under deep UV illumination (λ = 254 nm) [102, 103]. On the other hand, HAp powder heated at 1150°C did not possess photocatalytic activity under UV irradiation. The signal superoxide radical was detected by electron spin resonance (ESR) measurement using the spin trapping reagent (5,5-dimethyl-1-pyrroline-1-oxide, (DMPO)) under UV irradiation for both HAp heated at 200°C and HAp heated at 1150°C. However, the signal of trapped electron was observed only for HAp heated at 200°C. From XRD patterns, the crystallinity of HAp heated at 200°C was lower than that of HAp heated at 1150°C. Further experiments suggested that the changes of PO_4^{3-} groups on the HAp surface and the generation of a trapped electron of HAp heated at 200°C suggest that the oxygen vacancy was induced by UV irradiation. Then the superoxide radical was generated from the electron transfer from the trapped electron in oxygen vacancy to atmospheric oxygen. The photocatalytic behavior of HAp would be due to the formation of superoxide radicals by UV illumination [104].

Piccirillo *et al*. prepared HAp from natural origin (cod fish bone) [105]. The cod fish bones were treated in a solution of calcium acetate or calcium chloride followed by annealing

at 1000°C. The obtained HAp powder, treated in calcium acetate solution, showed photocatalytic activity under UV irradiation for degradation of methylene blue solution. The oxygen vacancies in HAp lattice may form during the calcination in reducing environment due to the presence of organic fragments derived from calcium acetate. The existence of oxygen vacancies in HAp lattice can cause the light absorption and the radical generation under UV illumination that provides photocatalytic activity. On the other hand, the HAp powder, treated in calcium chloride solution, did not possess light absorption and photocatalytic activity. Bystrov *et al*. compared the calculated bandgap energy of HAp created by various possible oxygen vacancies in HAp lattice with the measured bandgap energy of HAp prepared from cod fish bones and commercial HAp powder [**106**]. In non-photocatalytic HAp, if any vacancies exist, they are O atoms from OH group. The calculated bandgap energy of HAp, which possesses oxygen deficiency in phosphate groups, was matched with the HAp treated in calcium acetate solution. This result confirmed the hypothesis described above. The oxygen vacancies in phosphate group play an important role for the photocatalytic activity of HAp.

1.3. Titanium-doped hydroxyapatite (Ti-HAp)

The presence of dopants in HAp structure can decrease the bandgap energy of HAp. Wakamura *et al*. prepared Ti-doped hydroxyapatite (Ti-HAp) by hydrothermal method using $Ti(SO_4)_2$ as a titanium source [**107**]. The obtained Ti-HAp possessed light absorption in UV range and photocatalytic activity under UV illumination. Ti-HAp retains surface chemical properties of HAp. Therefore, it possesses higher adsorption capability than other normal oxide against various organic compounds.

1.3.1. Crystal and electronic structures of Ti-HAp

The crystal structure of Ti-HAp is hexagonal ($P6_3/m$) type due to the lattice deficiency from substitution of Ti atoms at Ca sites. The maximum amount of doped Ti atoms is 10 mol% against Ca atoms to retain HAp structure [107]. The position of Ti atom in HAp structure was still unclear. It can be located at either Ca1 site, Ca2 site or both of them. Yin *et al*. investigated the electronic structure of Ti-HAp using density functional theory (DFT) [108]. The doped Ti ions have been considered into two different Ti species; Ti^{4+} ion and $Ti(OH)_2^{2+}$ ion. Regarding Ti^{4+} ion, it has a smaller ionic radius and a larger electronegativity compared to Ca^{2+} ion and it can be doped at both Ca1 site and Ca2 site without site preference. For the charge compensation, two H atoms were removed from the OH^- channel. Due to the removal of H atoms, Ti^{4+} ions preferred to substitute at Ca2 site and a large shift of O atom forming a strong Ti–O bond. However, the Ti^{4+} substitution and occupation is not thermodynamically. In case of $Ti(OH)_2^{2+}$ substitution, $Ti(OH)_2^{2+}$ ion preferred to substitute at Ca2 site and induced a large geometry relaxation and distortion within the OH^- channel and Ca^{2+} column. The $Ti(OH)_2^{2+}$ substitution on Ca2 site has a strong thermodynamic favorability. These results corresponded to the ICP analysis suggesting that divalent ion ($Ti(OH)_2^{2+}$) substituted Ca^{2+} ions in Ti-HAp. This prediction of Ti substitution in HAp structure provided lower crystallinity similar to Wakamura's experimental results [107].

Tsukada *et al*. experimentally and theoretically evaluated the effect of Ti substitution in HAp on the bandgap energy [101]. They used Ti-HAp (with 10 mol% of Ti), pure HAp, and typical anatase phase TiO_2 as the samples. The obtained optical bandgap energies of Ti-HAp, HAp, and TiO_2 measured by diffuse reflectance spectroscopy were 3.65 eV, >6 eV, and 3.27 eV, respectively. The Ti substitution in this report was considered as one Ti^{4+} ion substituted at Ca site with one Ca^{2+} ion deficiency for charge compensation. Depending on total energy

evaluation and structure optimization by the first principle density functional calculation, the Ti^{4+} position in HAp structure was predicted to be at Ca1 site with one Ca^{2+} ion deficiency at Ca1 site. In Ti-HAp, Ti 3d orbital and O 2p orbital formed a hybrid orbital located between the valence band and the conduction band of HAp as shown in **Fig. 1.14**. However, the hybrid orbital was caused by weak covalent bonding of the Ti atom and O atoms. This hybrid orbital reduced the bandgap energy and increased light absorption edge of Ti-HAp compared with HAp. The electrons in the valence band can be excited to hybridized state by absorption of photon in UV range and then subsequently excited to the conduction band by absorption of additional photon. However, the second excitation seem rarely to occur. These prediction of Ti position was obtained by DFT calculation. It is necessary to determine the Ti position in Ti-HAp experimentally using the neutron diffraction technique and X-ray absorption fine structure (XAFS) analysis.

Kandori *et al*. examined Ti-HAp particles by using XRD and FTIR measurement [109]. From XRD results, the dimension *a* of original Ti-HAp and heat treated Ti-HAp do not vary with increasing Ti content. On the other hand, the dimension *c* of original Ti-HAp decreased with increasing Ti content. It can be explained by replacement of larger Ca^{2+} ions by smaller Ti^{4+} ions. However, after heat treatment, the dimension *c* increased with increasing Ti content, indicating that crystal structure expanded along *c* direction. This expansion of crystal structure may induce the formation of dislocated OH^- ions. From FTIR results, a new band appeared at 3428 cm^{-1} close to the peak at 3570 cm^{-1} of OH^- ions after heat treated Ti-HAp over 600°C for 1 h. It indicated that the dislocated OH^- ions were formed by substitution of Ti atoms. The band at 3737 cm^{-1} corresponding to Ti–OH groups was observed for Ti-HAp samples. The produced dislocated OH^- ions by heat treatment induce the photocatalytic activity of Ti-HAp.

1.3.2. Adsorption capability and photocatalytic activity

Ti-HAp has been reported that it has high affinity against various organic compound similar to HAp. Moreover, Ti-HAp also possesses photocatalytic activity under UV irradiation to decompose the adsorbed organic compounds such as acetaldehyde, methylene blue, and proteins. Wakamura *et al*. firstly examined the photocatalytic degradation of albumin protein and gaseous acetaldehyde using Ti-HAp [107]. **Figure 1.15** shows the results of albumin adsorption and photocatalytic decomposition of albumin under UV illumination of TiO_2, HAp, and Ti-HAp. Ti-HAp possessed high adsorption against albumin similar to HAp and it showed photocatalytic activity to decompose albumin similar to TiO_2. Furthermore, Ti-HAp exhibited photocatalytic activity to decompose acetaldehyde into CO_2 under UV illumination.

Kandori *et al*. investigated the proteins adsorption behaviors onto Ti-HAp, HAp, and TiO_2 (TKP-101) and the effect of calcination at 650°C onto Ti-HAp (Ti-HAp650) and HAp (HAp650) samples [110, 111]. Three types of proteins were used in this experiments; acidic bovine serum albumin (BSA), neutral myglobin (MGB), and basic lysozyme (LSZ). All the adsorption isotherms of BSA, MGB, and LSZ from 1×10^{-4} mol/dm^3 KCl solution were the Langmuirian type. The electrostatic interaction is the most important interaction that determine protein structure and their influence on protein adsorption. Among these samples, TiO_2 possesses the lowest adsorption capacity for these proteins because it has small particle diameter (ca. 4nm) which is too small for adsorbing large protein molecules. The solution pH of the system was around 8 in all measurements. The adsorption capacity of BSA was in the order of HAp650 > Ti-HAp650 > HAp > Ti-HAp > TiO_2. At pH 8, BSA is negatively charged. BSA was adsorbed easily at positively charged (calcium site) of HAp650 and Ti-HAp650 since the HAp and Ti-HAp particles were grown by calcination at 650°C which increased the amount of exposed calcium sites. The adsorption capacity of LSZ was in the order of

Ti-HAp650 > Ti-HAp > HAp650 > HAp > TiO_2. At pH 8, LSZ is positively charged. The amounts of adsorbed proteins are depended on the zeta potential of samples. The negative zeta potential of Ti-HAp (-18 mV) is much larger than that of HAp (-6 mV) at pH 8. This large negative zeta potential of Ti-HAp gives a proof that surface Ti–OH group induced a strong surface acidity in aqueous solution. The adsorption capacity of MGB was similar among these samples because isostatic point of MGB is 7 which close to pH 8 in the system and the number of the fundamental function groups in MGB are less than those of BSA and LSZ. The adsorption of MGB was independent from the zeta potential of samples due to the electrical neutrality of MGB molecules. After the heat treatment at 650°C, small amount of tricalcium phosphate (β-TCP) phase might appear which cannot be detected by XRD. Since the solubility of β-TCP is 10 times higher than that of HAp around pH 8, β-TCP can dissolve to attain Ca^{2+} and PO_4^{3-} ions in the solutions. These dissolved ions can act as binders between proteins and HAp surface. From this reason, HAp650 and Ti-HAp650 exhibited higher adsorption capacity than those of HAp and Ti-HAp.

The decomposition of adsorbed protein molecules (BSA, MGB, and LSZ) on the Ti-HAp surface was evaluated under UV irradiation [**112–114**]. The ability of decomposition of proteins is strongly depended on the molecular weight and rigidity of proteins molecules but not on the electrostatic interaction. The decomposition rates of the three proteins followed the order LSZ > MGB > BSA. No change in BSA concentration under UV irradiation was observed for Ti-HAp samples. This result indicated that the decomposition of BSA molecules is difficult to take place due to its large molecular weight. The LSZ with low molecular weight and rigid structure is easier to decompose by Ti-HAp under UV irradiation.

Kandori *et al*. reported the decomposition of surfactants by the photocatalytic activity of Ti-HAp under UV irradiation [**115**]. Three types of surfactants were used in this studies;

cationic cetyltrimethylammonium bromide (CTAB), anionic sodium dodecyl sulfate (SDS), and nonionic polyoxyethylene nonylphenyl ether (NP-15). The order of decomposition rates of the three surfactants can be written as CTAB > SDS >> NP-15. These differences may explained by (i) differences in chemical bond energies of the surfactants, i.e., N–C (358 kJ/mol) < S–O (433 kJ/mol) << C–O (1071 kJ/mol), and (ii) electrostatic attractive or repulsive forces between surfactants molecules and Ti-HAp surface.

Li *et al*. investigated the photocatalytic degradation of bisphenol A (BPA) using Ti-HAp and TiO_2 (P25) [**116**]. Ti-HAp particles exhibited higher adsorption capacity of BPA than that of TiO_2 about 19 times under the same conditions. This high adsorption capacity of Ti-HAp came from the hydrogen bond between the hydroxyl groups of BPA and the hydroxyl groups on the Ti-HAp surface. Due to the higher adsorption capacity, Ti-HAp provided the higher photocatalytic degradation of BPA under UV illumination.

Anmin *et al*. reported the photocatalytic degradation of methylene blue (MB) using Ti-HAp and TiO_2 [**117**]. Ti-HAp particles exhibited higher adsorption capacity of MB than that of TiO_2 despite they have similar specific surface area. It indicated that Ti-HAp possesses higher affinity against MB than that of TiO_2. The photocatalytic properties of Ti-HAp have been observed by the decomposition of MB under UV illumination. The photocatalytic activity of Ti-HAp increased with increasing Ti content up to 20 mol% against Ca. The photocatalytic activity of Ti-HAp may related with the particle size, crystallinity, morphology, specific surface area, and surface state.

Tsuruoka *et al*. investigated the photocatalytic degradation of gaseous 2-propanol (IPA) using Ti-HAp and TiO_2 (anatase, ST-21) [**118**]. Before UV illumination, Ti-HAp exhibited higher IPA adsorption capacity than TiO_2 despite its smaller specific surface area. This result indicated that Ti-HAp possesses better affinity against gaseous IPA than that of TiO_2. Under

UV irradiation, both Ti-HAp and TiO_2 decomposed IPA into acetone and CO_2. However, the IPA decomposition rate of Ti-HAp is inferior to that for TiO_2 although Ti-HAp has excellent affinity against organic compound. This result is expected to be related to the difference in crystallinity and the bandgap energy of the powders. The photocatalytic activity of Ti-HAp is given by Ti substitution and resultant formation of impurity level in the original bandgap of HAp. Therefore, the photocatalytic activity of Ti-HAp is expected to be limited by doping amount. Photocatalytic activity might not exceed TiO_2, even if the adsorbed photon amount is the same.

1.3.3. Recent studies and problems on Ti-HAp

Ti-HAp possesses high photocatalytic activity to decompose various organic compounds under UV irradiation due to its high affinity against those organic compounds. However, the original photocatalytic activity of Ti-HAp is inferior to that of TiO_2 because the doping amount of Ti is limited at around 10 mol% against Ca atoms to retain HAp structure. Moreover, due to the light absorption only in UV range, the application of Ti-HAp is limited. To improve the photocatalytic activity of Ti-HAp, several attempts have been conducted in previous as following.

Gangarajula *et al*. investigated the photocatalytic activity of Ti-substituted strontium hydroxyapatite (SrHAp) and TiO_2 loaded SrHAp [**119**]. The Ti-substituted SrHAp was prepared by using $SrCO_3$, $TiCl_4$, and H_3PO_4 as starting materials. In case of TiO_2 loaded SrHAp, SrHAp powder was added to the solution of $TiCl_4$ at pH 10 adjusted by adding ammonium dioxide. From UV-vis spectra, SrHAp shows light absorption edge around 320 nm which is attributed to a change in the surface energy state of SrHAp. For Ti-substituted SrHAp at 5 mol% of Ti (Ti-SrHAp), the light absorption of Ti-SrHAp was similar to that of

Ti-HAp indicated that Ti 3d orbital and O 2p orbital formed a hybrid orbital located between the valence band and the conduction band of SrHAp similar to Ti-HAp. The photocatalytic activity was evaluated by decomposition of *p*-nitrophenol solution under UV illumination. The results showed that the photocatalytic activity among there samples were in the order of TiO_2-loaded SrHAp > Ti-SrHAp > SrHAp. SrHAp is found to exhibit promising photocatalytic activity unlike CaHAp due to the difference in the Sr−O and Ca−O bond nature and Sr−O bonding lengths could influence the surface phosphate group which enables a change in electronic structure. However, the photocatalytic activity of Ti-SrHAp is inferior to that of TiO_2-loaded SrHAp. Furthermore, the comparison of photocatalytic activity of Ti-HAp and Ti-SrHAp is needed to examine.

Liu *et al*. prepared Fe-doped HAp by treating HAp in $FeCl_3$ aqueous solution [**120**]. The obtained sample can absorb light in visible range because the doped Fe ions introduced an impurity energy level between the conduction band and the valence band of HAp. However, the photocatalytic activity of Fe-doped HAp was not particularly high due to its low crystallinity. The rhodamine B (RhB) was degraded by around 44% under 4 h of visible irradiation. The degradation of RhB increased to 86% by adding a small amount of H_2O_2 (0.5 mM), which suppresses the recombination of photoinduced electron and hole pairs, and promotes the generation of hydroxyl radicals with strong oxidation power [**121**].

Nishikawa *et al*. prepared V-doped HAp by hydrothermal method using VCl_3 aqueous solution as a vanadium source [**122**]. The obtained V-doped HAp possessed absorption edge in visible range indicated that new energy level due to V ion was formed between the conduction band and the valence band of HAp as shown in **Fig. 1.16(b)**. Its light absorption edge was shifted to longer wavelength with increasing V content. The light absorption edge reached to around 530 nm at 10 mol% of V amount. At 10 mol% of V amount, the HAp

structure was kept after calcination at 400°C. On the other hand, after calcination at 650°C, the HAp structures of V-doped HAp samples with V content at 5 and 10 mol% were decomposed into tricalcium phosphate ($Ca_3(PO_4)_3$) and vanadium oxide (V_2O_5). Unlike Ti-HAp at 10 mol% of Ti, it can retain the HAp structure after calcination at 650°C. It indicated that V-doped HAp was unstable at temperature higher than 400°C. However, V-doped HAp can decompose gaseous acetaldehyde under visible irradiation. The V ions in HAp structure acted as an electron acceptor and the redox potential was negative enough to reduce O_2 molecule into H_2O_2 via two-electron reduction process (**Fig. 1.16(a)**).

Wakamura *et al*. modified Cr^{3+} onto Ti-HAp particles by impregnation method using $Cr(NO_3)_3 \cdot 9H_2O$ aqueous solution [**123**]. The crystal structure and morphology of the Cr^{3+}-modified Ti-HAp did not change after modification. The obtained Cr^{3+}-modified Ti-HAp exhibited the light absorption peaks at 446 and 623 nm in visible range. The light absorption increased with increasing Cr^{3+} concentration. The photocatalytic decomposition of gaseous acetaldehyde into CO_2 was observed under visible irradiation and the activity was suppressed by the formation $Cr(OH)_3$-like layer on the particle surface with high Cr^{3+} concentration. From FTIR results, the Cr^{3+} modification provided the surface Cr-OH group on the surface that played a role in the visible light photocatalytic activity of this sample.

Nishikawa *et al*. modified Cu^{2+} onto Ti-HAp particles by impregnation method using $CuCl_2$ aqueous solution [**124**]. This Cu modification method was successfully improved visible photocatalytic activity of TiO_2 via direct electron transfer from the valence band of TiO_2 to the grafted metal ions (IFCT) [**67, 68**]. However, in case of Cu-modified Ti-HAp, the rate of IFCT excitation was extremely small compared to that of TiO_2 because the valence band of Ti-HAp composes of P and O atoms which form the PO_4 group. The P–O bond shows a covalent nature, the electrons in the valence band are somewhat localized between P and O

atoms. The visible light photocatalytic activity was not obtained. However, the photocatalytic degradation of the materials against gaseous acetaldehyde under UV illumination was increased about three times compared to that of Ti-HAp. From ESR measurement, it revealed that valence band electrons transfer to Cu^{2+} via Ti-hybridized band, which suppressed the recombination of electron-hole pairs (**Fig. 1.17**).

In previous, we have tried to doped various elements (Zn, Fe, Cu, Mn, Ce, Si, Nb) or co-doped with Ti into HAp structure by hydrothermal synthesis. However, none of these elements could provide visible light photocatalytic activity or higher UV light photocatalytic activity than that of Ti-HAp. The other method is needed to investigate.

1.4. Objective and strategy of present work

The objective of this research is to enhance photocatalytic activity of Ti-HAp. We found that doping of various elements into HAp or Ti-HAp was ineffective. This time, we changed the strategy to use surface modification techniques, which are effective on TiO_2, instead of doping. There are two different surface modification techniques will be studied in this research. The first surface modification technique is simple impregnation technique, which the sample will be soaked in the aqueous solution of metal ion. The other modification technique is chemisorption calcination cycle (CCC), which using metal organic compound. The metal complexes are chemically adsorbed on the surface then the organic parts are oxidized by post-heating.

In **Chapter 2**, we clarified the differences between these modification techniques by introducing same element (Fe) onto the same TiO_2 powders (same phase and same specific surface area). These Fe-modification techniques were also employed on Ti-HAp powder. Then the photocatalytic activity was evaluated by the decomposition of IPA under visible

illumination. The role of Fe-modification on different substrates will be discussed.

In **Chapter 3**, we modified Ti-HAp and HAp by impregnation technique using aqueous solution of $CaMoO_4$. The photocatalytic activity was measured by the decomposition of IPA under UV illumination. The computational method using density functional theory (DFT) was conducted to clarify the state of Mo-modification whether it was doped into Ti-HAp structure or formed a cluster on the surface. The clusters are expected to be either $CaMoO_4$ or MoO_x based on the starting material. It was found that the Mo-modified Ti-HAp provided higher photocatalytic activity than that of Ti-HAp by several times. The role of Mo-modification will be discussed.

In **Chapter 4**, we modified Ti-HAp and HAp by CCC technique using ethanol solution of $MoO_2(acac)_2$. The photocatalytic activity was measured by the decomposition of IPA under UV illumination. By using CCC technique, we could directly modify MoO_x onto Ti-HAp or HAp surface, and control the surface modifiable amount. The results were compared with those in **Chapter 3** to clarify the Mo state of Mo-modified Ti-HAp prepared in **Chapter 3**. The role of Mo-modification onto Ti-HAp and HAp will be discussed.

In **Chapter 5**, the obtained results through this research will be summarized.

References

[1] J. Schneider, M. Matsuoka, M. Takeuchi, J. Zhang, Y. Horiuchi, M. Anpo, D.W. Bahnemann, Understanding TiO_2 photocatalysis: mechanisms and material, *Chem. Rev*., **114** (2014) 9919−9986.

[2] O. Carp, C.L. Huisman, A. Reller, Photoinduced reactivity of titanium dioxide, *Prog. Solid State Chem*., **32** (2004) 33−177.

[3] A.L. Linsebigler, G. Lu, J.T. Yates, Photocatalysis on TiO_2 surfaces: principles, mechanisms, and selected results, *Chem. Rev*., **95** (1995) 735−758.

[4] K. Okamoto, Y. Yamatomo, H. Tanaka, M. Tanaka, A. Itaya, Heterogeneous photocatalytic decomposition of phenol over TiO_2 powder, *Bull. Chem. Soc. Jpn*., **58** (1985) 2015−2022.

[5] M. Anpo, T. Shima, S. Kodama, Y. Kubokawa, Photocatalytic hydrogenation of CH_3CCH with H_2O on small-particle TiO_2: size quantization effects and reaction intermediates, *J. Phys. Chem*., **91** (1987) 4305−4310.

[6] Y. Hu, H.L. Tsai, C.L. Huang, Effect of brookite phase on the anatase−rutile transition in titania nanoparticles, *J. Euro. Cera. Soc*., **23** (2003) 691−696.

[7] T. Tachikawa, M. Fujitsuka, T. Majima, Mechanistic insight into the TiO_2 photocatalytic reactions: design of new photocatalysts, *J. Phys. Chem. C*, **111** (2007) 5259−5275.

[8] A.J. Hoffman, E.R. Carraway, M.R. Hoffman, Photocatalytic production of H_2O_2 and organic peroxides on quantum-sized semiconductor colloids, *Environ. Sci. Technol*., **28** (1994) 776−785.

[9] C.A. Emilio, M.I. Litter, M. Kunst, M. Bouchard, C. Colbeau-Justin, Phenol photodegration on platinized-TiO_2 photocatalysts related to charge-carrier dynamics, *Langmuir*, **22** (2006) 3606−3613.

[10] P. Pichat, J. Disdier, C. Hoand-Van, D. Mas, G. Goutialler, C. Gaysse, Purification/deodorization of indoor air and gaseous effluents by TiO_2 photocatalysis, *Catal. Today*, **63** (2000) 363−369.

[11] J.M. Herrmann, Heterogeneous photocatalysis: fundamentals and applications to the removal of various types of aqueous pollutants, *Catal. Today*, **53** (1999) 115−129.

[12] T.N. Obee, R.T. Brown, TiO_2 photocatalysis for indoor air applications: effects of humidity and trace contaminant levels on the oxidation rates of formaldehyde, toluene, and 1,3-butadiene, *Environ. Sci. Technol*., **29** (1995) 1223−1231.

[13] Y. Paz, Application of TiO_2 photocatalysis for air treatment: patents' overview, *Appl. Catal. B: Environ*., **99** (2010) 448−460.

[14] S.Y. Lee, S.J. Park, TiO_2 photocatalyst for water treatment applications, *J. Indus. Eng. Chem*., **19** (2013) 1761−1769.

[15] J.G. Yu, H.G. Yu, B. Cheng, X.J. Zhao, J.C. Yu, W.K. Ho, The effect of calcination temperature on the surface microstructure and photocatalytic activity of TiO_2 thin films prepared by liquid phase deposition, *J. Phys. Chem. B*, **107** (2003) 13871−13879.

[16] P. Fernandez-Ibanez, J. Blanco, S. Malato, F.J. de las Nieves, Application of the colloidal stability of TiO_2 particles for recovery and reuse in solar photocatalysis, *Water Research*, **37** (2003) 3180−3188.

[17] J.C. Yu, J. Yu, J. Zhao, Enhanced photocatalytic activity of mesoporous and ordinary TiO_2 thin films by sulfuric acid treatment, *Appl. Catal. B: Environ.*, **36** (2002) 31−43.

[18] J.A. Byrne, B.R. Eggins, N.M.D. Brown, B. McKinney, M. Rouse, Immobilisation of TiO_2 powder for the treatment of polluted water, *Appl. Catal. B: Environ*., **17** (1998) 25−36.

[19] R.L. Pozzo, M.A. Baltanas, A.E. Cassano, Supported titanium oxide as photocatalyst in

water decomtamination: state of the art, *Catal. Today*, **39** (1997) 219−231.

[20] M.J. Benotti, B.D. Stanford, E.C. Wert, S.A. Snyder, Evaluation of a photocatalytic reactor membrane pilot system for the removal of pharmaceuticals and endocrine disrupting compounds from water, *Water Research*, **43** (2009) 1513−1522.

[21] K. Sunada, Y. Kikuchi, K. Hashimoto, A. Fujishima, Bactericidal and detoxification effects of TiO_2 thin film photocatalysts, *Environ. Sci. Technol*., **32** (1998) 726−728.

[22] C. Wei, W.Y. Lin, Z. Zainal, N.E. Williams, K. Zhu, A.P. Kruzic, R.L. Smith, K. Rajeshwar, Bactericidal activity of TiO_2 photocatalyst in aqueous media: toward a solar-assisted water disinfection system, *Environ. Sci. Technol*., **28** (1994) 934−938.

[23] R. Cai, K. Hashimoto, K. Itoh, Y. Kubota, A. Fujishima, Photokilling of malignant cells with ultrafine TiO_2 powder, *Bull. Chem. Soc. Jpn*., **64** (1991) 1268−1273.

[24] Y. Kikuchi, K. Sunada, T. Iyoda, K. Hashimoto, A. Fujishima, Photocatalytic bactericidal effect of TiO_2 thin films: dynamic view of the active oxygen species responsible for the effect, *J. Photochem. Photobio. A: Chem*., **106** (1997) 51−56.

[25] T. Matsunaga, R. Tomoda, T. Nakajima, N. Nakamura, T. Komine, Continuous-sterilization system that uses photosemiconductor powders, *Appl. Environ. Microbiol*., **54** (1988) 1330−1333.

[26] K. Sunada, T. Watanabe, K. Hashimoto, Studies on photokilling of bacteria on TiO_2 thin film, *J. Photochem. Photobio. A: Chem.*, **156** (2003) 227−233.

[27] B. Kim, D. Kim, D. Cho, S. Cho, Bactericidal effect of TiO_2 photocatalyst on selected food-borne pathogenic bacteria, *Chemosphere*, **52** (2003) 277−281.

[28] M. Miyauchi, A. Nakajima, A. Fujishima, K. Hashimoto, T. Watanabe, Photoinduced surface reactions on TiO_2 and $SrTiO_3$ films: photocatalytic oxidation and photoinduced hydrophilicity, *Chem. Mater*., **12** (2000) 3−5.

[29] K. Guan, Relationship between photocatalytic activity, hydrophilicity and self-cleaning effect TiO_2/SiO_2 films, *Surface & Coating Technol*., **191** (2005) 155−160.

[30] T. Watanabe, A. Nakajima, R. Wang, M. Minabe, S. Koizumi, A. Fujishima, K. Hashimoto, Photocatalytic activity and photoinduced hydrophilicity of titanium dioxide coated glass, *Thin Solid Films*, **351** (1999) 260−263.

[31] R. Wong, N. Sakai, A. Fujishima, T. Watanabe, K. Hashimoto, Studies of surface wettability conversion on TiO_2 single-crystal surfaces, *J. Phys. B*, **103** (1999) 2188−2194.

[32] S. Banerjee, D.D. Dionysiou, S.C. Pillai, Self-cleaning applications of TiO_2 by photo-induced hydrophilicity and photocatalysis, *Appl. Catal. B: Environ*., **176−177** (2015) 396−428.

[33] A. Fujishima, K. Honda, Electrochemical photolysis of water at a semiconductor electrode, *Nature*, **238** (1972) 37−38.

[34] A. Kudo, Y. Miseki, Heterogeneous photocatalyst materials for water splitting, *Chem. Soc. Rev*., **38** (2009) 253−278.

[35] M.G. Walter, E.L. Warren, J.R. McKone, S.W. Boettcher, Q. Mi, E.A. Santori, N.S. Lewis, Solar water splitting cells, *Chem. Rev*., **110** (2010) 6446−6473.

[36] H. Dong, G. Zeng, L. Tang, C. Fan, C. Zhang, Z. He, Y. He, An overview on limitations of TiO_2-based particles for photocatalytic degradation of organic pollutants and the corresponding countermeasures, *Water Research*, **79** (2015) 128−146.

[37] N. Serpone, Relative photonic efficiencies and quantum yields in heterogeneous photocatalysis, *J. Photochem. Photobio. A: Chem*., **104** (1997) 1−12.

[38] A.E. Jacobsen, Titanium dioxide pigments correlation between photochemical reactivity and chalking, *Indus. Eng. Chem*., **41** (1949) 523−526.

[39] T. Kawai, T. Sakata, Conversion of carbohydrate into hydrogen fuel by a photocatalytic process, *Nature*, **286** (1980) 474−476.

[40] S.N. Frank, A.J. Bard, Heterogeneous photocatalytic oxidation of cyanide ion in aqueous solutions at TiO_2 powder, *J. Amer. Chem. Soc*., **99** (1977) 303−304.

[41] A. Heller, Chemistry and applications of photocatalytic oxidation of thin organic films, *Acc. Chem. Res.*, **28** (1995) 503−508.

[42] K. Sunada, T. Watanabe, K. Hashimoto, Bactericidal activity of copper-deposited TiO_2 thin film under weak UV light illumination, *Environ. Sci. Technol*., **37** (2003) 4785−4789.

[43] T. Ohno, K. Sarukawa, K. Tokieda, M. Matsumura, Morphology of a TiO_2 photocatalyst (Degussa, P-25) consisting of anatase and rutile crystalline phases, *J. Catal*., **203** (2001) 82−86.

[44] T. Ohno, K.Tokieda, S. Higashida, M. Matsumura, Synergism between rutile and anatase TiO_2 particles in photocatalytic oxidation of naphthalene, *Appl. Catal. A: Gen.*, **244** (2003) 383−391.

[45] I. Nakamura, N. Negishi, S. Kutsuna, T. Ihara, S. Sugihara, K. Takeuchi, *J. Molecu. Catal. A: Chem.*, **161** (2000) 205−212.

[46] A. Zaleska, Doped-TiO_2: a review, *Recent Patents on Eng*., **2** (2008) 157−164.

[47] W. Choi, A. Termin, M.R. Hoffmann, The role of metal ion dopants in quantum-sized TiO_2: correlation between photoreactivity and charge carrier recombination dynamics, *J. Phys. Chem*., **98** (1994) 13669−13679.

[48] K. Wilke, H.D. Breuer, The influence of transition metal doping on the physical and photocatalytic properties of titania, *J. Photochem. Photobio. A: Chem*., **121** (1999) 49−53.

[49] H. Irie, Y. Watanabe, K. Hashimoto, Carbon-doped anatase TiO_2 powders as a visible-light sensitive photocatalyst, *Chem. Lett.*, **32** (2003) 772−773.

[50] W. Ren, Z. Ai, F. Jia, L. Zhang, X. Fan, Z. Zou, Low temperature preparation and visible light photocatalytic activity of mesoporous carbon-doped crystalline TiO_2, *Appl. Catal. B: Environ*., **69** (2007) 138−144.

[51] G. Wu, T. Nishikawa, B. Ohtani, A. Chen, Synthesis and characterization of carbon-doped TiO_2 nanostructures with enhanced visible light response, *Chem. Mater*., **19** (2007) 4530−4537.

[52] T. Umebayashi, T. Yamaki, H. Itoh, K. Asai, Band gap narrowing of titanium dioxide by sulfur doping, *Appl. Phys. Lett*., **81** (2002) 454−456.

[53] T. Ohno, T. Mitsui, M. Matsumura, Photocatalytic activity of S-doped TiO_2 photocatalyst under visible light, *Chem. Lett.*, **32** (2003) 364−365.

[54] T. Ohno, M. Akiyoshi, T. Umebayashi, K. Asai, T. Mitsui, M. Matsumura, Preparation of S-doped TiO_2 photocatalysts and their photocatalytic activities under visible light, *Appl. Catal. A: Gen.*, **265** (2004) 115−121.

[55] W. Ho, J.C. Yu, S. Lee, Low-temperature hydrothermal synthesis of S-doped TiO_2 with visible light photocatalytic activity, *J. Solid State Chem*., **179** (2006) 1171−1176.

[56] H. Irie, Y. Watanabe, K. Hashimoto, Nitrogen-concentration dependence on photocatalytic activity of $TiO_{2-x}N_x$ powders, *J. Phys. Chem. B*, **107** (2003) 5483−5486.

[57] R. Asahi, T. Morikawa, T. Ohwaki, K. Aoki, Y. Taga, Visible-light photocatalysis in nitrogen-doped titanium oxides, *Science*, **293** (2001) 269−271.

[58] C. Burda, Y. Lou, X. Chen, A.C.S. Semia, J. Stout, J.L. Gole, Enhanced nitrogen doping in TiO_2 nanoparticles, *Nano Lett*., **3** (2003) 1049−1051.

[59] C.D. Valentin, G. Pacchioni, A. Selloni, Origin of the different photoactivity of

N-doped anatase and rutile TiO_2, *Phys. Rev. B*, **70** (2004) 1−4.

[60] M. Mrowetz, W. Balcerski, A.J. Colussi, M.R. Hoffmann, Oxidation power of nitrogen-doped TiO_2 photocatalysts under visible illumination, *J. Phys. Chem. B*, **108** (2004) 17269−17273.

[61] A. Bhattacharyya, S. Kawi, M.B. Ray, Photocatalytic degradation of orange II by TiO_2 catalysts supported on adsorbents, *Catal. Today*, **98** (2004) 431−439.

[62] B. Gao, P.S. Yap, T.M. Lim, T.T. Lim, Adsorption-photocatalytic degradation of Acid Red 88 by supported TiO_2: effect of activated carbon support and aqueous anions, *Chem. Eng. J.*, **171** (2011) 1098−1107.

[63] T. Nonami, H. Hase, K. Funakoshi, Apatitte-coated titanium dioxide photocatalyst for air purification, *Catal. Today*, **96** (2004) 113−118.

[64] M. Hu, Z. Yao, X. Liu, L. Ma, Z. He, X. Wang, Enhancement mechanism of hydroxyapatite for photocatalytic degradation of gaseous formaldehyde over TiO_2/hydroxyapatite, *J. Taiwan Inst. Chem. Eng.*, **85** (2018) 91−97.

[65] K. Qi, B. Cheng, J. Yu, W. Ho, A review on TiO_2-based Z-scheme photocatalysts, *Chn. J. Catal*., **38** (2017) 1936−1955.

[66] J. Yu, S. Wang, J. Low, W. Xiao, Enhanced photocatalytic performance of direct Z-scheme g-C_3N_4-TiO_2 photocatalysts for the decomposition of formaldehyde in air, *Phys. Chem. Chem. Phys*., **15** (2013) 16883−16890.

[67] H. Irie, S. Miura, K. Kamiya, K. Hashimoto, Efficient visible light-sensitive photocatalysts: grafting Cu(II) ions onto TiO_2 and WO_3 photocatalysts, *Chem. Phys. Lett*., **457** (2008) 202−205.

[68] H. Irie, K. Kamiya, T. Shibanuma, S. Miura, D.A. Tryk, T. Yokoyama, K. Hashimoto, Visible light-sensitive Cu(II)-grafted TiO_2 photocatalysts: activities and X-ray

absorption fine structure analyses, *J. Phys. Chem. C*, **113** (2009) 10761−10766.

[69] M. Miyauchi, Z. Liu, Z.G. Zhao, S. Anandan, H. Tokudome, Visible-light-driven superhydrophilicity by interfacial charge transfer between metal ions and metal oxide nanostructures, *Langmuir*, **26** (2010) 796−801.

[70] H. Yu, H. Irie, Y. Shimodaira, Y. Hosogi, Y. Kuruda, M. Miyauchi, K. Hashimoto, An efficient visible-light-sensitive Fe(III)-grafted TiO_2 photocatalyst, *J. Phys. Chem. C*, **114** (2010) 16481−16487.

[71] M. Nolan, A. Iwaszuk, H. Tada, Molecular metal oxide cluster-surface modified titanium(IV) dioxide photocatalysts, *Aust. J. Chem.*, **65** (2012) 624−632.

[72] Q. Jin, M. Fujishima, A. Iwaszuk, M. Nolan, H. Tada, Loading effect in copper(II) oxide cluster-surface-modified titanium(IV) oxide on visible- and UV-light activities, *J. Phys. Chem. C*, **117** (2013) 23848−23857.

[73] H. Tada, Q. Jin, H. Nishijima, H. Yamamoto, M. Fujishima, S. Okuoka, T. Hattori, Y. Sumida, H. Kobayashi, Titanium(IV) dioxide surface-modified with iron oxide as a visible light photocatalyst, *Angew. Chem. Int. Ed.*, **50** (2011) 3501−3505.

[74] Q. Jin, T. Ikeda, M. Fujishima, H. Tada, Nickel(II) oxide surface-modified titanium(IV) dioxide as a visible-light-active photocatalyst, *Chem. Commun.*, **47** (2011) 8814−8816.

[75] P. Rulis, L. Ouyang, W. Y. Ching, Electronic structure and bonding in calcium apatite crystals: hydroxyapatite, fluorapatite, chloraptite, and bromapatite, *Phys. Rev. B*, **70** (2004) 155104−8.

[76] D. Haverty, S. A. M. Tofail, K. T. Stanton, J. B. McMonagle, Structure and stability of hydroxyapatite: density functional calculation and Rietveld analysis, *Phys. Rev. B*, **71** (2005) 094103−9.

[77] T. I. Ivanova, O. V. Frank-Kamenetskaya, A. B. Kol'tsov, V. L. Ugolkov, Crystal

structure of calcium-deficient carbonated hydroxyapatite thermal decomposition, *J. Solid state Chem.*, **160** (2001) 340−349.

[78] J. C. Elliott, P. E. Mackie, R. A. Young, Monoclinic hydroxyapatite, *Science*, **180** (1973) 1055−1057.

[79] H. E. Feki, J. M. Savariault, A. B. Salah, Structure refinements by the Rietveld method of partially substituted hydroxyapatite: $Ca_9Na_{0.5}(PO_4)_{4.5}(CO_3)_{1.5}(OH)_2$, *J. Alloys Compounds*, **287** (1999) 114−120.

[80] K. Sudarsanan, R. A. Young, Significant precision in crystal structural details: Holly Springs hydroxyapatite, *Acta Crys*., **B25** (1969) 1534−1543.

[81] T. Suzuki, K. Ishigaki, M. Miyake, Synthetic hydroxyapatites as inorganic cation exchangers, *J. Chem. Soc. Faraday Tran.*, **80** (1984) 3157−3165.

[82] X. Chen, J. V. Wright, J. L. Conca, L. M. Peurrung, Evaluation of heavy metal remediation using mineral apatite, *Water Air Soil Pollu*., **98** (1997) 57−78.

[83] S. H. Jang, B. G. Min, Y. G. Jeong, W. S. Lyoo, S. C. Lee, Removal of lead ions in aqueous solution by hydroxyapatite/polyurethane composite foams, *J. Hazz. Mater*., **152** (2008) 1285−1292.

[84] T. Suzuki, T. Hatsushika, Y. Hayakawa, Synthetic hydroxyapatites employed as inorganic cation-exchangers, J. Chem. Soc. *Faraday Trans*., **77** (1981) 1059−1062.

[85] Y. Takeuchi, H. Arai, Removal of coexisting Pb^{2+}, Cu^{2+} and Cd^{2+} ions from water by addition of hydroxyapatite powder, *J. Chem. Eng. Jpn*., **23** (1990) 75−80.

[86] Q. Y. Ma, T. J. Logan, S. J. Traina, Effects of NO_3^-, Cl^-, F^-, SO_4^{2-}, and CO_3^{2-} on Pb^{2+} immobilization by hydroxyapatite, *Environ. Sci. Tech*., **28** (1994) 408−418.

[87] N. S. Resende, M. Nele, V. M. M. Salim, Effects of anion substitution on the acid properties of hydroxyapatite, *Thermo. Acta*, **451** (2006) 16−21.

[88] A. Yasukawa, E. Ueda, K. Kandori, T. Ishikawa, Preparation and characterization of carbonated barium-calcium hydroxyapatite solid solutions, *J. Coll. Interface Sci.*, **288** (2005) 468−474.

[89] S. Kulanthaivel, B. Roy, T. Agarwal, S. Giri, K. Pramanik, K. Pal, S. S. Ray, T. K. Maiti, I. Banerjee, Cobalt doped proangiogenic hydroxyapatite for bone tissue engineering application, *Mater. Sci. Eng. C*, **58** (2016) 648−658.

[90] A. Yasukawa, S. Ouchi, K. Kandori, T. Ishikawa, Preparation and characterization of magnesium-calcium hydroxyapatites, *J. Mater. Chem*., **6** (1996) 1401−1405.

[91] T. Ishikawa, H. Saito, A. Yasukawa, K. Kandori, Adsorption of CO_2, CH_3OH, and H_2O on Fe(III)-substituted calcium hydroxyapatites, *Bull. Chem. Soc. Jpn*., **69** (1996) 899−907.

[92] M. Wakamura, K. Kandori, T. Ishikawa, Surface composition of calcium hydroxyapatite modified with metal ions, *Coll. Sur. A: Phys. Eng. Aspects*, **142** (1998) 107−116.

[93] M. Kresak, E. C. Moreno, R. T. Zahradnik, D. I. Hay, Adsorption of amino acids onto hydroxyapatite, *J. Coll. Int. Sci.*, **59** (1977) 283−293.

[94] Q. Luo, J. D. Andrade, Cooperative adsorption of proteins onto hydroxyapatite, *J. Coll. Int. Sci.*, **200** (1998) 104−113.

[95] K. Lin, J. Pan, Y. Chen, R. Cheng, X. Xu, Study the adsorption of phenol from aqueous solution on hydroxyapatite nanopowders, *J. Hazz. Mater.*, **161** (2009) 231−240.

[96] C. Xiaoli, Z. Youcai, Adsorption of phenolic compound by aged-refuse, *J. Hazz. Mater*., **137** (2006) 410−417.

[97] A. Dabrowski, P. Podkoscielny, Z. Hubicki, M. Barczak, Adsorption of phenolic compounds by activated carbon a critical review, *Chemosphere*, **58** (2005) 1049−1070.

[98] E. D. Berry, G. R. Siragusa, Hydroxyapatite adherence as a means to concentrate

bacteria, *Appl. Environ. Micro*., **63** (1997) 4069−4074.

[99] T. Kawai, C. Ohtsuki, M. Kamitakahara, M. Tanihara, T. Miyazaki, Y. Sakaguchi, S. Konagaya, Removal of formaldehyde by hydroxyapatite later biomimetically deposited on polyamide film, *Environ. Sci. Tech.*, **40** (2006) 4281−4285.

[100] J. Xu, T. White, P. Li, C. He, Y. F. Han, Hydroxyapatite foam as a catalyst for formaldehyde combustion at room temperature, *J. Am. Chem. Soc*., **132** (2010) 13172−13173.

[101] M. Tsukada, M. Wakamura, N. Yoshida, T. Watanabe, Band gap and photocatalytic properties of Ti-substituted hydroxyapatite: comparison with anatase-TiO_2, *J. Mole. Catal. A: Chem.*, **338** (2011) 18−23.

[102] H. Nishikawa, K. Omamiuda, Photocatalytic activity of hydroxyapatite for methyl mercaptane, *J. Mole. Catal. A: Chem.*, **179** (2002) 193−200.

[103] H. Nishikawa, Surface changes and radical formation on hydroxyapatite by UV irradiation for inducing photocatalytic activation, *J. Mole. Catal. A: Chem.*, **206** (2003) 331−338.

[104] H. Nishikawa, Photo-induced catalytic activity of hydroxyapatite based on photo-exciation, *Phos. Res. Bull.*, **21** (2007) 97−102.

[105] C. Piccirillo, C. W. Dunnill, R. C. Pullar, D. M. Tobaldi, J. A. Labrincha, I. P. Parkin, M. M. Pintado, P. M. L. Castro, Calcium phosphate-based materials of natural origin showing photocatalytic activity, *J. Mater. Chem. A*, **1** (2013) 6452−6461.

[106] V. S. Bystrov, C. Piccirillo, D. M. Tobaldi, P. M. L. Castro, J. Coutinho, S. Kopyl, R. C. Pullar, Oxygen vacancies, the optical band gap (E_g) and photocatalysis of hydroxyapatite: comparing modelling with measured data, *Appl. Catal. B: Envi.*, **196** (2016) 100−107.

[107] M. Wakamura, K. Hashimoto, T. Watanabe, Photocatalysis by calcium hydroxyapatite modified with Ti(IV): albumin decomposition and bactericidal effect, *Langmuir*, **19** (2003) 3428−3431.

[108] S. Yin, D. E. Ellis, First-principles investigations of Ti-substituted hydroxyapatite electronic structure, *Phys. Chem. Chem. Phys.*, **12** (2010) 156−163.

[109] K. Kandori, M. Oketani, Y. Sakita, M. Wakamura, FTIR studies on photocatalytic activity of Ti(IV)-doped calcium hydroxyapatite particles, *J. Mole. Catal. A: Chem*., **360** (2012) 54−60.

[110] K. Kandori, T. Kuroda, M. Wakamura, Protein adsorption behaviors onto photocatalytic Ti(IV)-doped calcium hydroxyapatite particles, *Col. Sur. B: Biointerfaces*, **87** (2011) 472−479.

[111] K. Kandori, M. Oketani, M. Wakamura, Effect of Ti(IV) substitution on protein adsorption behaviors of calcium hydroxyapatite particles, *Col. Sur. B: Biointerfaces*, **101** (2013) 68−73.

[112] K. Kandori, M. Oketani, M. Wakamura, Decomposition of proteins by photocatalytic Ti(IV)-doped calcium hydroxyapatite particles, *Coll. Sur. B: Biointer.*, **102** (2013) 908−914.

[113] K. Kandori, H. Hamazaki, M. Wakamura, Selective decomposition of proteins by photocatalytic Ti(IV)-doped calcium hydroxyapatite particles from mixed-protein systems, *Coll. Polym. Sci.*, **292** (2014) 59−65.

[114] K. Kandori, H. Wada, M. Wakamura, Acceleration of protein decomposition by photocatalytic Ti(IV)-doped calcium hydroxyapatite particles and its application for reduction of pathogenic proteins, *Coll. Polym. Sci.*, **292** (2014) 2261−2268.

[115] K. Kandori, Y. Yamaguchi, M. Wakamura, Photodecomposition of surfactants using

Ti(IV)-doped calcium hydroxyapatite particles, *Coll. Polym. Sci*., **295**, 2017, 1079−1087.

[116] Q. Li, X. Feng, X. Zhang, H. Song, J. Zhang, J. Shang, W. Sun, T. Zhu, M. Wakamura, M. Tsukada, Y. Lu, Photocatalytic degradation of bisphenol A using Ti-substituted hydroxyapatite, *Chn. J. Catal*., **35** (2014) 90−98.

[117] H. Amin, L. Ming, C. Chengkang, M. Dali, Preparation and characterization of a titanium-substituted hydroxyapatite photocatalyst, *J. Mole. Catal. A: Chem.*, **267** (2007) 79−85.

[118] A. Tsuruoka, T. Isobe, S. Matsushita, M. Wakamura, A. Nakajima, Comparison of photocatalytic activity and surface friction force variation on Ti-doped hydroxyapatite and anatase under UV illumination, *J. Photochem. Photobio. A: Chem.*, **311** (2015) 160−165.

[119] Y. Gangarajula, R. Kedharnath, B. Gopal, Investigation of photocatalytic activity of pure strontium hydroxyapatite and its Ti-substituted and TiO_2 loaded forms, *Appl. Catal. A: Gen*., **506** (2015) 100−108.

[120] X. Liu, J. Ma, J. Yang, Visible-light-driven amorphous Fe(III)-substituted hydroxyapatite photocatalyst: characterization and photocatalytic activity, Mater. Lett., **137** (2014) 256−259.

[121] M. Huang, C. Xu, Z. Wu, Y. Huang, J. Lin, J. Wu, Photocatalytic discolorization of methyl orange solution by Pt modified TiO_2 loaded on natural zeolite, *Dyes and Pigments*, **77** (2008) 327−334.

[122] M. Nishikawa, L. H. Tan, Y. Nakabayashi, T. Hasegawa, W. Shiroishi, S. Kawahara, N. Saito, A. Nosaka, Y. Nosaka, Visible light responsive vanadium-substituted hydroxyapatite photocatalysts, *J. Photochem. Photobio. A: Chem.*, **311** (2015) 30−34.

[123] M. Wakamura, H. Tanaka, Y. Naganuma, N. Yoshida, T. Watanabe, Surface structure and visible light photocatalytic activity of titanium-calcium hydroxyapatite modified with Cr(III), *Adv. Pow. Tech*., **22** (2011) 498−503.

[124] M. Nishikawa, W. Yang, Y. Nosaka, Grafting effects of Cu^{2+} on the photocatalytic activity of titanium-substituted hydroxyapatite, *J. Mole. Catal. A: Chem*., **378** (2013) 314−318.

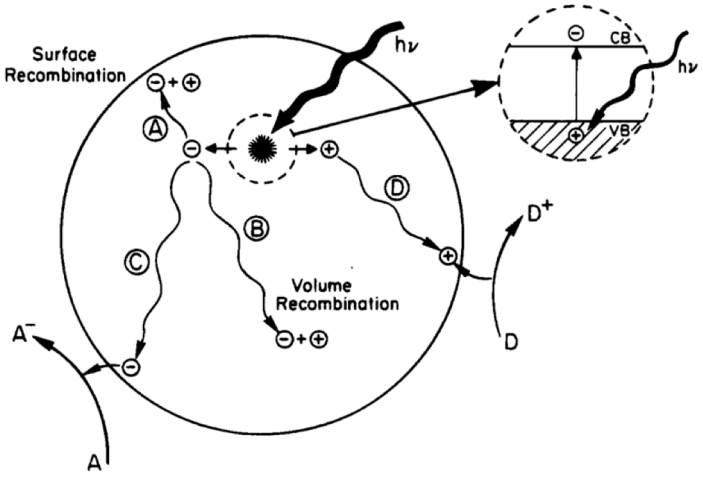

Figure 1.1 Schematic of photocatalytic reaction in a solid followed by recombination of the photoinduced electron and hole pairs [3].

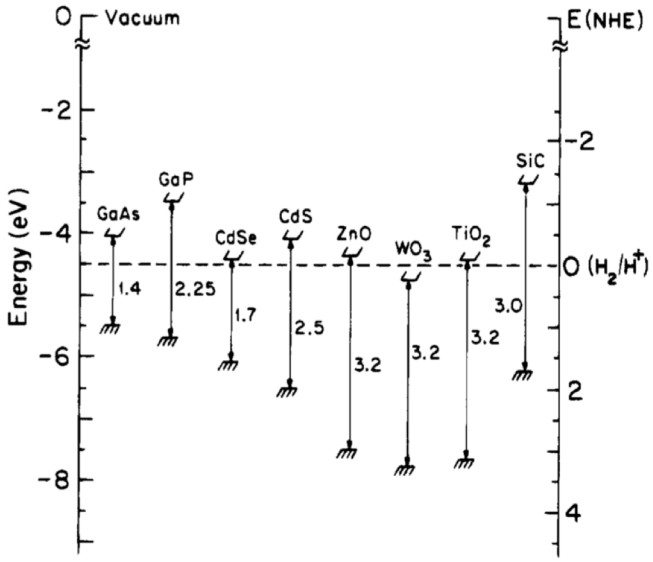

Figure 1.2 Energies for various semiconductors in aqueous electrolytes at pH = 1 [3].

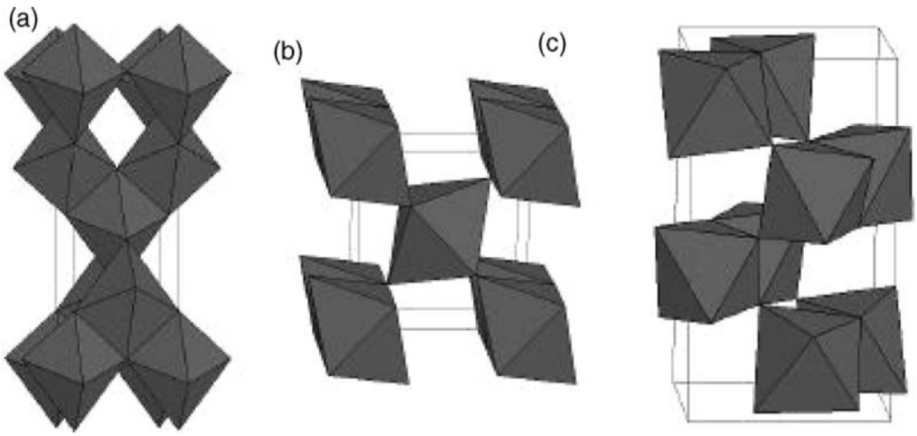

Figure 1.3 Bulk structures of TiO_2 polymorphs: (a) anatase, (b) rutile, and (c) brookite [2].

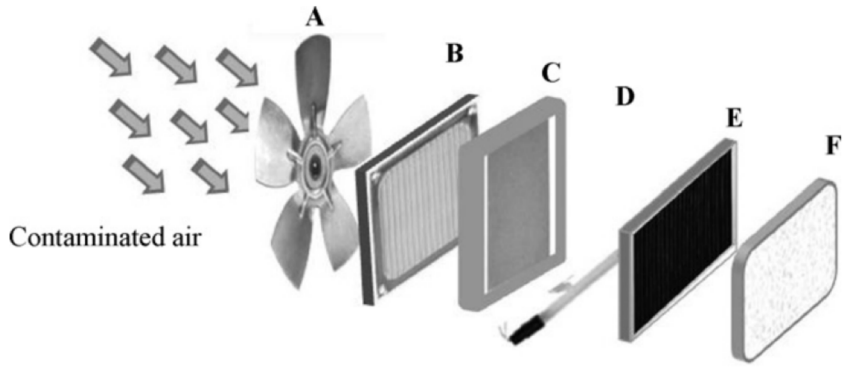

Figure 1.4 A schematic view of a photocatalytic indoor air treatment device. Changes may vary from product to product. (A) fan, (B) particulates (HEPA) filter, (C) photocatalyst, (D) light source, (E) activated carbon filter (optional), and (F) ionizer generator (optional) [13].

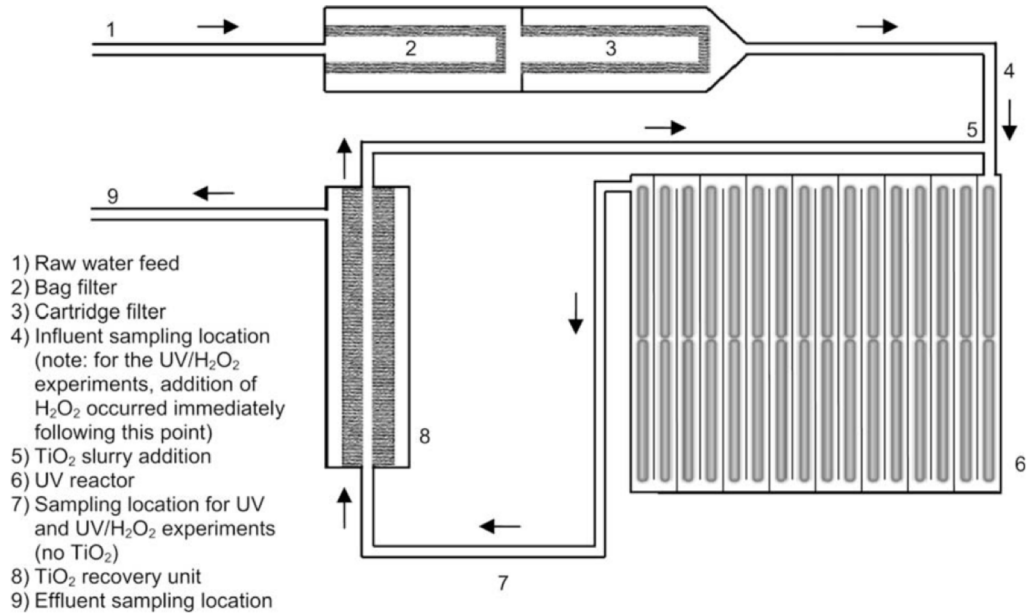

Figure 1.5 Schematic photocatalyst membrane reactors for water purification [20].

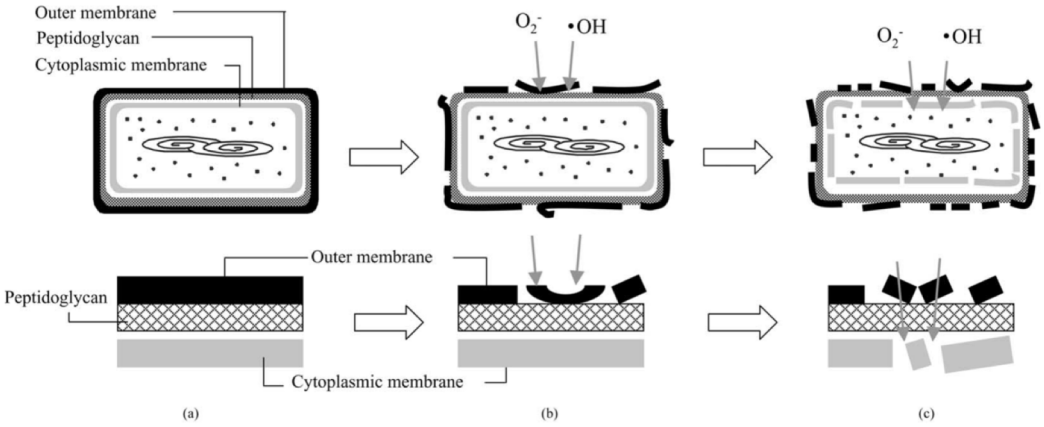

Figure 1.6 Schematic illustration of the process of *E. Coli.* photokilling on TiO_2 film [26].

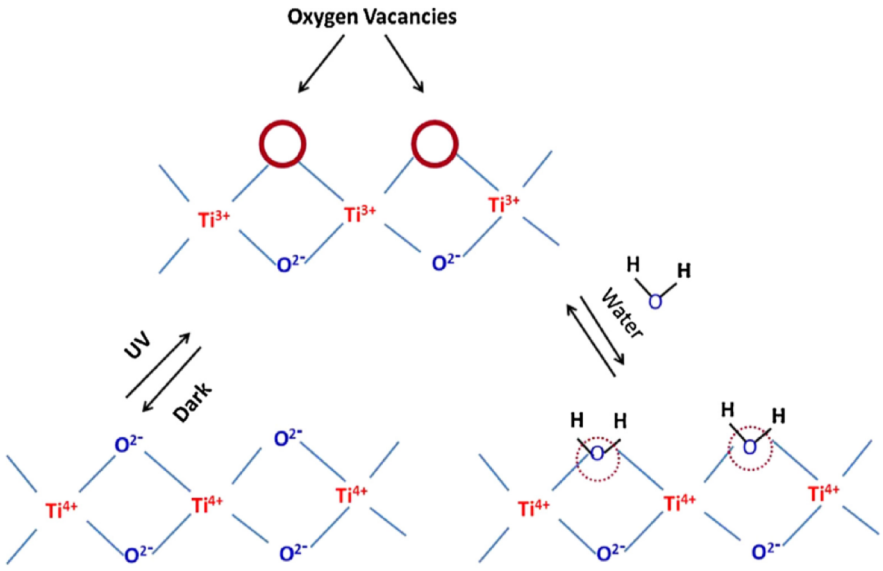

Figure 1.7 Schematic of photoinduced hydrophilicity. Electrons reduce the Ti^{4+} to Ti^{3+} state and thereby the oxygen atoms will be ejected (creation of oxygen vacancies). Oxygen vacancies will increase the affinity for water molecules and thereby transforming the surface hydrophilic [32].

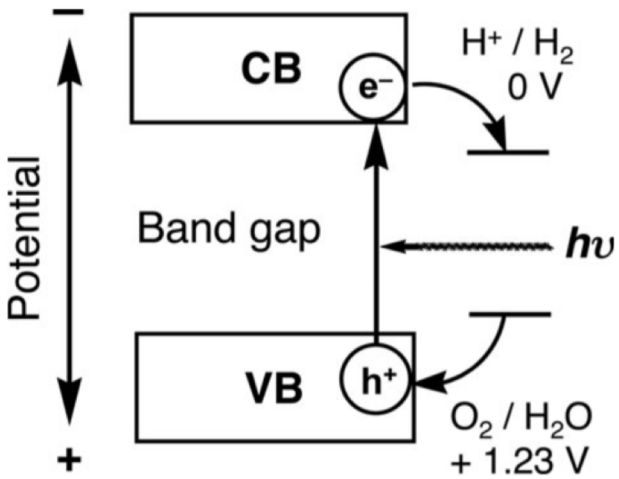

Figure 1.8 Principle of water splitting using semiconductor photocatalyst [34].

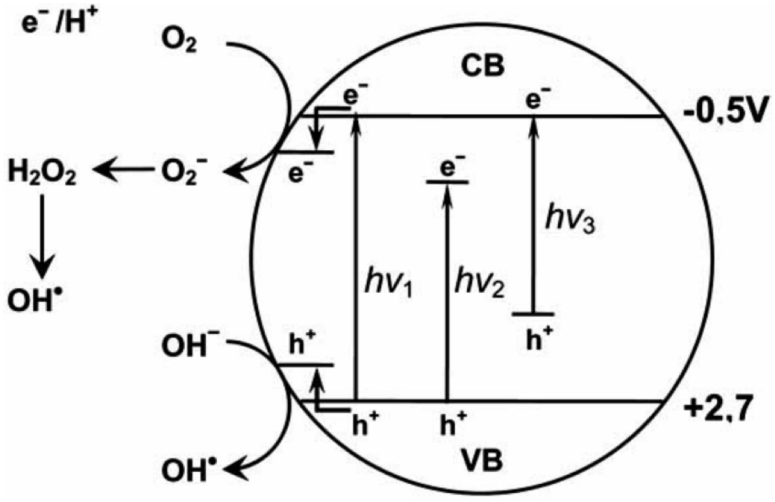

Figure 1.9 Mechanism of TiO_2 photocatalysis: hv_1: pure TiO_2; hv_2: metal-doped TiO_2 and hv_3: nonmetal-doped TiO_2 [46].

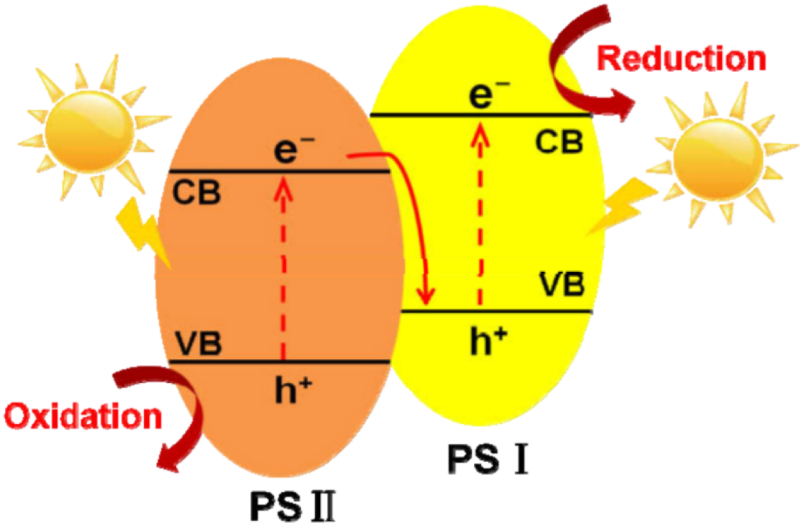

Figure 1.10 Charge carrier separation mechanism in direct Z-scheme photocatalyst built from two different semiconductors [65].

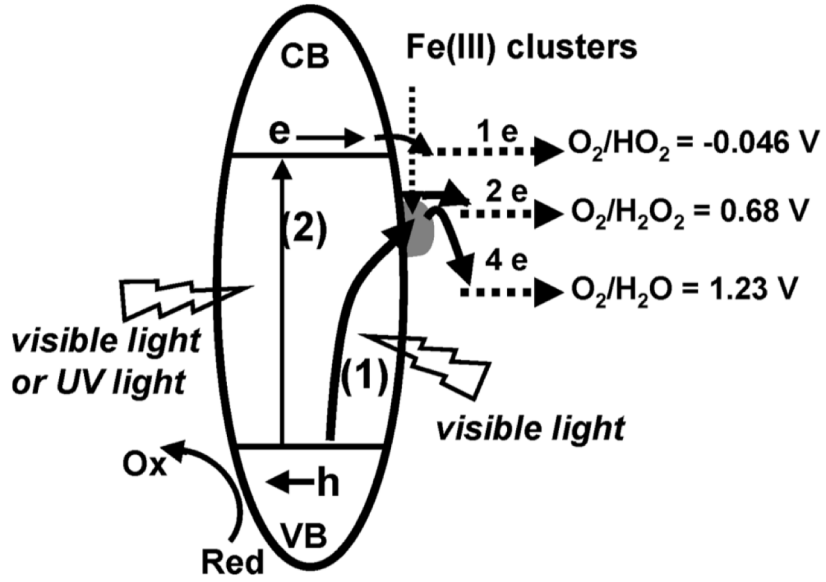

Figure 1.11 Schematic diagram illustrating the possible photocatalytic mechanism of Fe(III)/TiO_2, involving IFCT (arrow 1) and multielectron reduction processes. The bandgap excitation is indicated by arrow 2 [70].

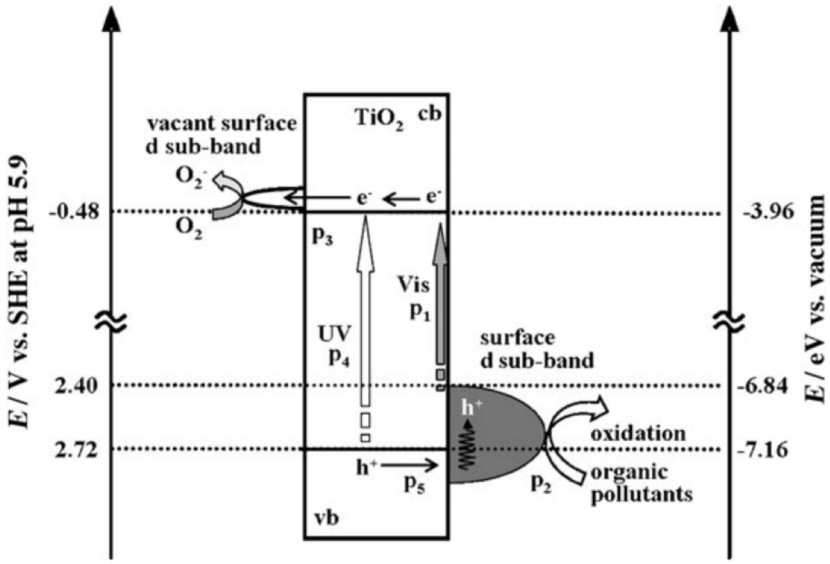

Figure 1.12 Energy band diagram for Fe-modified TiO_2. The position of the vacant d levels is assumed to be close to that of iron doped into rutile [73].

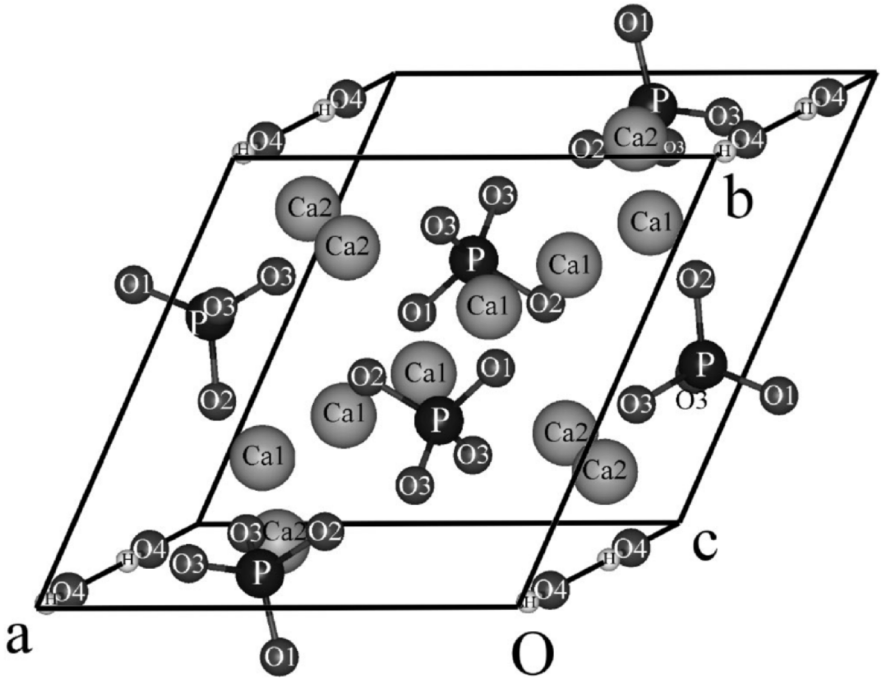

Figure 1.13 Model of HAp crystal with atoms labeled according to element and symmetric type [75].

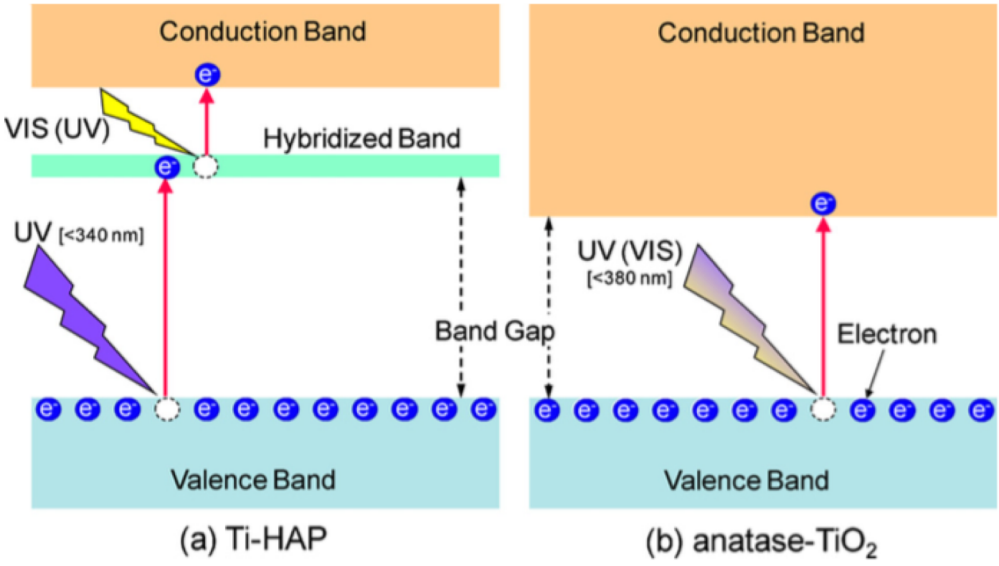

Figure 1.14 Schematic photocatalytic model of (a) Ti-HAp, and (b) anatase [101].

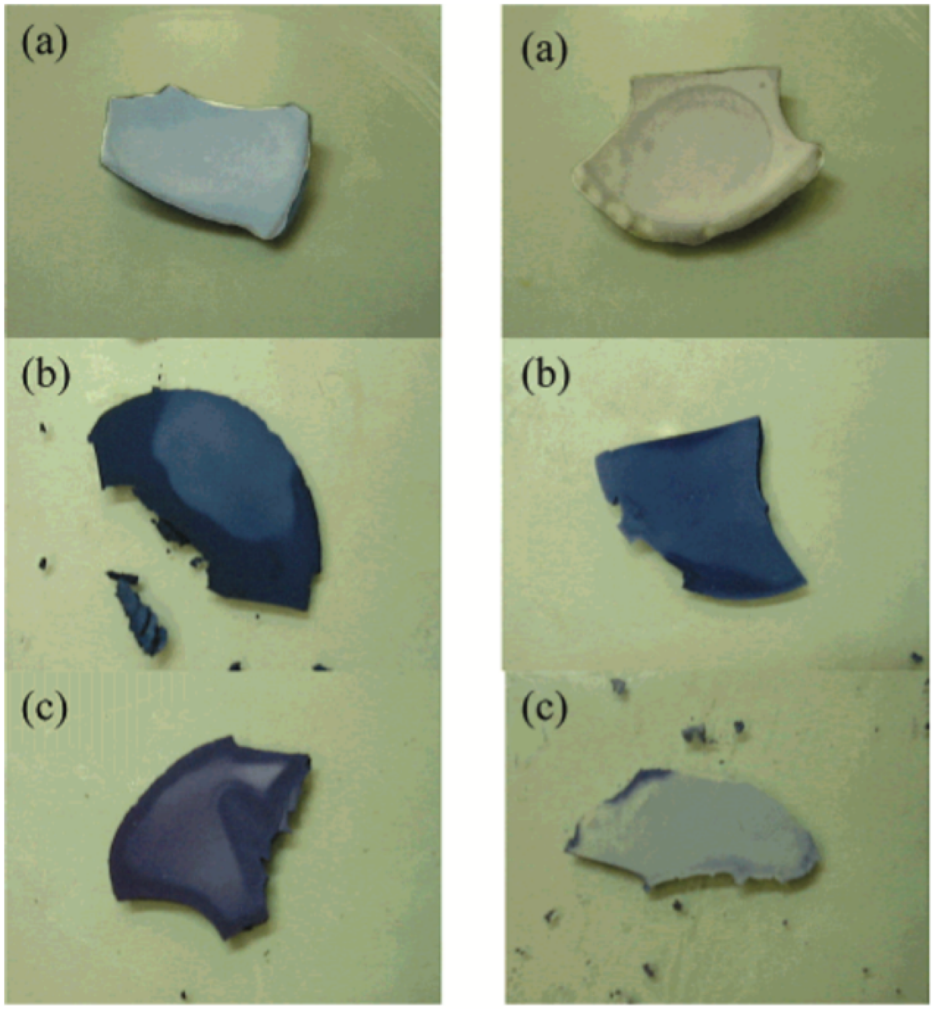

Figure 1.15 Results of adsorption and photocatalysis decomposition of albumin obtained by ninhydrin colored tests: (a) TiO_2, (b) HAp, and (c) Ti-HAp [107].

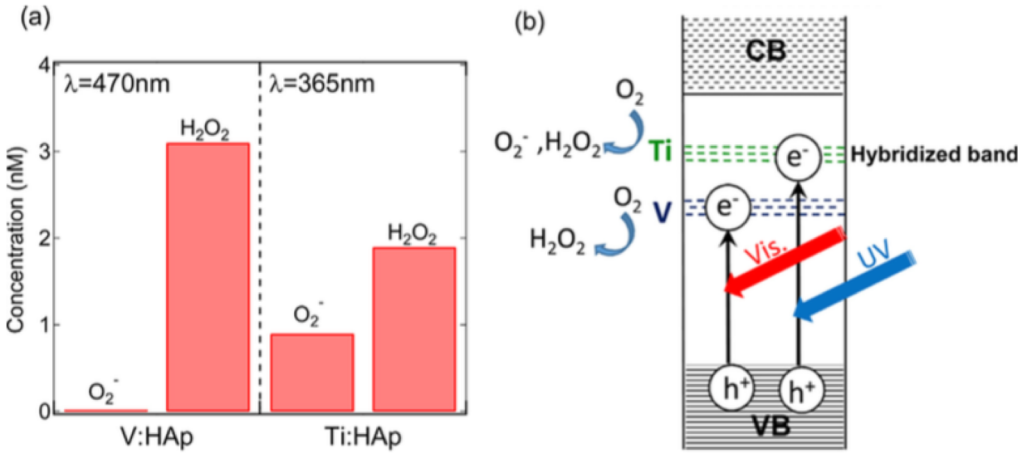

Figure 1.16 (a) Amounts of O_2^- and H_2O_2 generated on V-HAp and Ti-HAp under light irradiation for 10 s, (b) Suggested electronic band structure of V-HAp [122].

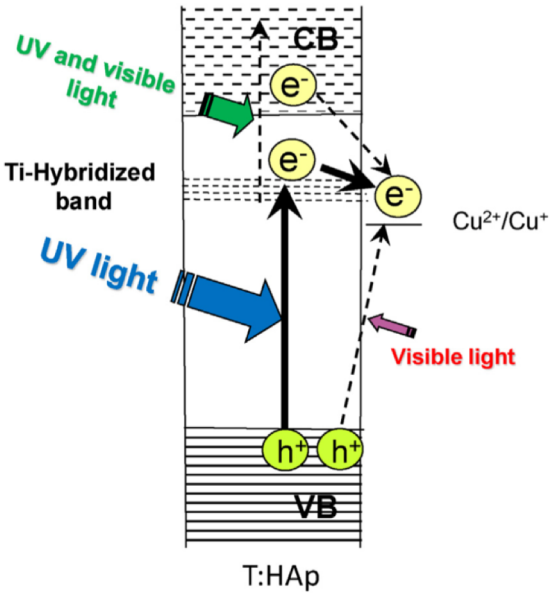

Figure 1.17 A plausible charge transfer process under light irradiation of Cu^{2+} grafted Ti-HAp [124].

CHAPTER 2

Comparative study on the effect of Fe-modification onto TiO_2 and Ti-HAp powders

2.1. Introduction

To enhance photocatalytic activity under visible light of TiO_2, the surface modification techniques of transition metals were applied in this study. Recently, Irie *et al*. reported grafting of Cu(II) ions onto TiO_2 as an effective approach to improve TiO_2 sensitivity to visible light by the interfacial charge transfer (IFCT) mechanism [1, 2]. For their studies, they prepared this catalyst merely using impregnation technique by soaking TiO_2 into an aqueous solution of $CuCl_2$ and then drying it. They reported that the grafted metal species has a distorted metal oxide cluster [2]. Hereinafter in this research, the process is designated as metal cluster grafting (MCG). In their report, the charge transfer from the valence band of TiO_2 to Cu(II) ions on the surface, not via the excited state, is feasible by visible light (ca. 450 nm) because of the redox potential of Cu(II)/Cu(I) (0.16 V vs. SHE). The photoinduced holes in the valence band of TiO_2 oxidize organic compounds with their oxidation power, whereas the produced Cu(I) reduce the adsorbed O_2 by a multielectron process. Additional investigations have revealed that IFCT is more effective for rutile than anatase [3]. A similar effect was reported for Fe(III) ion grafting onto TiO_2 through the redox reaction of Fe(III)/Fe(II) [4].

On the other hand, Tada *et al*. provided visible light photocatalytic activity to TiO_2 by grafting FeO_x onto TiO_2 using the chemisorption calcination cycle (CCC) technique, by which metal complexes are adsorbed onto the surface of TiO_2 and the organic (ligand) part is oxidized by post-heating to prepare metal oxide clusters [5]. They used Degussa P-25

(anatase/rutile = 4/1 w/w) as a TiO_2 source, and proposed that electronic excitation from the surface d sub-band, yielded by mixing between the surface Fe(III) levels and O 2p by the Ti–O–Fe interfacial bond to the conduction band of TiO_2, plays an important role for visible light photocatalytic activity.

Although both cases used Fe as a modification element and suggested Fe-cluster formation on the surface of TiO_2, different mechanisms were proposed. These investigations were conducted using different TiO_2 sources and modification processes. For this study, we prepared Fe-modified TiO_2 using MCG and CCC following procedures described in previous reports [**4, 5**] using the same TiO_2 powder. Then, photocatalytic decomposition activity was evaluated using gaseous 2-propanol (IPA) under visible light. The role of Fe modification for these cases was discussed.

These Fe modification techniques were also conducted onto Ti-HAp to enhance visible light photocatalytic activity of Ti-HAp. Because the photocatalytic activity of Ti-HAp is originated from TiO_6 octahedral in the structure, which is similar to that of TiO_2. The modification techniques that effectively improve visible light photocatalytic activity of TiO_2 might be effective onto Ti-HAp as well. The role of Fe modification for Ti-HAp was discussed.

2.2. Experimental procedure

2.2.1. Materials

For this study, we used commercial TiO_2 powders (rutile; MT-150A, Tayca Corp., Osaka, Japan: anatase; ST-01, Ishihara Sangyo Kaisha Ltd., Mie, Japan) and commercial Ti-HAp (Hautoform; Fuji Chemical Ind. Co. Ltd., Osaka, Japan) as starting materials. Calcination in ambient air at 600°C (MT-150A) or 650°C (ST-01) for 1 h provides rutile or anatase

single-phase powder with almost identical specific surface area (around 35 m^2/g). The calcined TiO_2 powders were used for Fe modification. Ti-HAp powders were used without further calcination because of similar specific surface area (ca. 39 m^2/g).

2.2.2. Fe modification by metal cluster grafting (MCG)

Reagent grade iron chloride ($FeCl_3 \cdot 6H_2O$; Wako Pure Chemical Industries Ltd., Osaka, Japan) was dissolved into distilled water (10 mL) at 90°C. Then rutile or anatase powders were added to the Fe solution (Fe/TiO_2 = 0.03 or 0.05 mass%); they were stirred for 1 h at room temperature. The powder was filtered and washed several times with distilled water. Then Fe-modified TiO_2 powder by MCG was obtained after drying at 100°C for 24 h. We also prepared sample for comparison using Ti-HAp instead of TiO_2 under the same conditions. These samples are denoted as X-M1 or X-M2, with X representing the base material (Ru for rutile, An for anatase, or TH for Ti-HAp), and M1 and M2 respectively correspond to 0.03 and 0.05 mass% solution.

2.2.3. Fe modification by chemisorption calcination cycle (CCC)

Reagent grade iron acetylacetonate ($Fe(C_5H_8O_2)_3$, $Fe(acac)_3$; Strem Chemicals Inc., MA, USA) was dissolved into ethanol/hexane (3:17 v/v) mixture solvent (100 mL, 0.65 mM) at room temperature. After rutile or anatase powders (1 g) were added to the solution, they were allowed to stand for 24 h at room temperature. The resulting samples were washed repeatedly using the same solvent and were then dried at 100°C for 24 h, followed by heating in air at 500°C for 1 h in ambient air. These procedures were conducted once (C1) or two times (C2) to change the Fe loading amount. We also prepared sample for comparison using Ti-HAp instead of TiO_2 under the same conditions. These samples that were Fe-modified by CCC are

designated in this report as X-C1 or X-C2, with X representing the base material (Ru for rutile, An for anatase, or TH for Ti-HAp).

2.2.4. Characterization

The crystalline phase was evaluated using X-ray diffraction (XRD; XRD-6100, Shimadzu Corp., Japan). Using a UV–vis scanning spectrophotometer (V-660; Jasco Corp., Tokyo, Japan), the UV-vis absorption spectra were evaluated. Powder morphology was observed using a field-emission scanning electron microscope (JSM-7500F; JEOL Ltd., Tokyo Japan) and a transmission electron microscope (JEM-2010F; JEOL Ltd., Tokyo Japan) equipped with EDS (Genesis, EDAX Inc., Mahwah, NJ U.S.A.). The surface chemical composition and element binding energy were measured using X-ray photoelectron spectroscopy (XPS, ESCA 5500MT; PerkinElmer Inc., U.S.A.) with an Al Kα X-ray line (1486.6 eV). Specific surface areas were measured using Brunauer–Emmett–Teller (BET) method with N_2 (BEL SORP mini; Bel Japan Inc., Japan).

2.2.5. Photocatalytic activity

The photocatalytic activity was evaluated according to the decomposition of gaseous IPA. The sample powder (40 mg) was dispersed into a petri dish with area of 8.35 cm^2. Before evaluation, UV pre-illumination (ca. 0.7 mW/cm^2 at 355 nm) onto the sample powder was conducted for one night to remove organic compounds that might have been adsorbed onto the sample. Then the sample dish was set at the center of a Pyrex glass (500 mL in volume). Subsequently, the vessel was sealed with a quartz lid and was filled with air (20°C, 80% relative humidity). Then IPA gas (300 ppm) was injected into it. The vessel was kept in the dark for one night to achieve the adsorption equilibrium. Subsequently, visible light

illumination (42,000 Lux) was produced using a illuminator (LA-410UV-3; Hayashi Watch Works, Tokyo, Japan) equipped with a Xe lamp through a liquid light guild with an L-42 filter (absorbed light < 420 nm (50% transmittance); Asahi Glass Co. Ltd., Japan) to create a large amount of light within the wavelength range that is feasible for excitation. The light spectra was shown in **Fig 2.1**. The concentrations of IPA and CO_2 were measured every 2 h using a gas chromatograph (GC-2014; Shimadzu Corp., Tokyo, Japan) equipped with a flame ionization detector (FID), methanizer, and column (Sunpak-A; Shimadzu Corp., Tokyo, Japan). Action spectra was also measured for this reaction (initial IPA concentration: 200 ppm) using a monochromator (wavelength dispersion from the center one was approximately ±50 nm.) at 450, 500, and 550 nm.

2.3. Results and discussion

The specific surface areas of all these TiO_2 powders were almost equivalent (33–38 m^2/g). No specific crystalline phase except rutile structure with $P4_2/mnm$ (No. 136) space group or anatase structure with $I4_1/amd$ (No. 141) space group was identified from samples using XRD as shown in **Fig. 2.2** and **2.3**. The specific surface area of all Ti-HAp powder (ca. 39 m^2/g) were close to those of TiO_2. The XRD patterns showed the peaks attributable to a HAp structure with $P6_3/m$ (No. 176) space group. No marked difference was observed after Fe-modification. **Figure 2.4** shows SEM images of TiO_2 before and after Fe-modification. Both anatase and rutile samples have spherical morphology with 50 nm average particle diameter. However, Fe-clusters were not observed using SEM in the microstructure after Fe-modification. Using TEM, we were able to identify them on the TiO_2 surface modified by MCG (**Fig. 2.5**). Their size was around 3–5 nm, which corresponds to the recent report by Miyauchi *et al.* [6]. The signal of Cu in the EDS spectra of **Fig. 2.5** is that from the sample

mesh used for this observation. Nevertheless, we were unable to identify the Fe-clusters clearly on the TiO_2 surface modified by CCC, as was done in a previous study by Tada *et al.* [5], probably because of the extremely small size as shown in **Fig. 2.6**. These results imply that the Fe-cluster size and morphology differ between MCG and CCC.

Figure 2.7 presents UV–Vis spectra of the Fe-modified TiO_2 powders. New light absorption (370–640 nm) by Fe modification was attributed to the d–d transition and to the electronic transition from Fe(III) ions to the conduction band of TiO_2 [7]. XPS analysis revealed the surface atomic ratios (%) of Fe against Ti (Fe/(Fe+Ti)) for the samples as 3.1(An-C1), 2.4(An-C2), 1.6(An-M1), 3.9(An-M2), 2.0(Ru-C1), 4.6(Ru-C2), < 1(Ru-M1), and 1.3(Ru-M2). Although Fe concentrations for An-C1 and An-C2 are reversed, for reasons that remain unclear, the samples from the 0.05 mass% solution (An-M2, and Ru-M2) and twice-coated sample (Ru-C2) provide high Fe concentration on the surface. **Figure 2.8** presents UV–vis spectra of the Fe-modified Ti-HAp powders. New light absorption (360–600 nm) by Fe modification of TH-M2 was attributed to the d–d transition or the substitution of Fe(III) for Ca(II) in Ti-HAp structure. The doped Fe(III) ions can introduce an impurity energy level into the electronic band structure of Ti-HAp [8]. For TH-C1 sample, light absorption was slightly increased in visible range indicated that the electron transfer via IFCT mechanism was insufficient [9]. However, these Fe-modified Ti-HAp samples were not analyzed by XPS.

Figure 2.9 presents the concentration change of IPA and CO_2 against the light illumination time. The C_0 in the *y*-axis of the figure denotes the initial IPA concentration before light illumination. The slight decrease of IPA for pure anatase and rutile is expected to be attributable to the small amount of light leakage through the long-pass (L-42) filter. The Fe-modified anatase provides weak photocatalytic activity under visible illumination.

However, Fe-modified rutile possesses high decomposition activity. The IPA concentration reaches zero within 2 h for Ru-C2 and Ru-M2, and within 4 h for Ru-C1 and Ru-M1. The respective C_0 values of these samples were 147 ppm (Ru-C1), 193 ppm (Ru-C2), 153 ppm (Ru-M1) and 110 ppm (Ru-M2).

The CO_2 generation rates of Ru-C1 (3.6 ppm/h) and Ru-C2 (4.0 ppm/h) are lower than those of Ru-M1 (4.5 ppm/h) and Ru-M2 (15.2 ppm/h) despite higher surface Fe concentration. This rate was calculated in the linear range (0–6 h) of the relation between the CO_2 concentration and the illumination time. Actually, Ru-C2 exhibits a higher IPA decomposition rate and a higher CO_2 generation rate than those of Ru-C1. Therefore, excess grafting and a resultant decrease of oxidation sites on the surface should not be the main reason for this trend. A plausible explanation for the difference among rutile-based samples is the rise in the top of the surface d sub-band leading to decreased oxidation power of the photoinduced holes for the samples from CCC. It is noteworthy that Ru-C2 shows a higher IPA decomposition rate than Ru-M1, although its CO_2 generation rates are lower than that of Ru-M1. These results suggest a difference of photocatalytic decomposition mechanisms between samples processed using MCG and using CCC.

The results of action spectra also support this inference (**Fig. 2.10**). This measurement was conducted of Ru-M1 and Ru-C1 samples. The thresholds of the activity for Ru-C1 by CCC are longer than those of Ru-M1 by MCG (see inset, **Fig. 2.10**). This result suggests that the absorption band ranges differ between Ru-C1 and Ru-M1. For the Fe-modified Ti-HAp samples, they did not provide photocatalytic activity under visible illumination as shown in **Fig. 2.11**.

Figure 2.12 shows XPS spectra of the binding energy of O 2p, VB of the samples. Emission from the O 2p extends from 2 eV to 9 eV. Detailed inspection of the VB top (inset

in **Fig. 2.12**) shows its decrease concomitantly with increasing surface Fe concentration for C1 and C2 samples, which corresponds to a bandgap decrease with surface modification. This trend is obtainable from both anatase and rutile, suggesting effective mixing between the surface Fe(III) levels and O 2p by formation of a Ti–O–Fe interfacial bond yielding a surface d sub-band, which disperses around the energy level to overlap with the valence band of TiO_2 proposed by Tada *et al*. [5]. However, such a valence band top change was not detected in M1 and M2 samples. The new absorption by Fe modification for the samples prepared by MCG process can be attributed to the IFCT from the valence band of TiO_2 to the Fe(III) ions. These samples were not fired but merely dried after soaking in a $FeCl_3$ aqueous solution. Therefore, Fe(III) ions in the form of FeO(OH)-like clusters are merely attached onto the TiO_2 surface [2]. In this IFCT mechanism, the photoinduced electrons are transferred directly to Fe(III) ions, producing Fe(II) ions capable of reducing oxygen by multielectron reduction processes because of the redox potential of Fe(III)/Fe(II) (0.771 V vs. SHE, pH = 0) [10], whereas the photoinduced holes remain in the valence band of TiO_2 and oxidize organic compounds such as IPA and acetone. The suggested mechanism difference in modified Fe clusters between MCG and CCC is presented schematically in **Fig. 2.13**. In case of the Fe-modified Ti-HAp, the direct electron transfer via IFCT is insufficient due to the valence band of Ti-HAp comprises the covalent bonding of PO_4^{3-}. The valence electrons are localized between P and O atoms, leading to the difficulty in electronic excitation from O atom to Fe(III) ion [9]. Moreover, the formation of the Ti–O–Fe interfacial bond yielding a surface d sub-band by CCC technique might be insufficient due to the covalent nature of the valence band of Ti-HAp. The expected energy diagram of Fe-modified Ti-HAp was presented in **Fig. 2.14**.

The K–M function of UV-Vis spectra revealed that the bandgap of starting materials was 3.00 eV (rutile) and 3.19 eV (anatase). Because of the smaller initial band-gap, Fe

modification by both methods is expected to more effective for rutile than for anatase. However, despite being the same element (Fe), differences in the modification process engender different mechanisms for photocatalytic activity under visible light. Based on the expected mechanism, it was inferred that not only the oxidation power, but also the entire reaction yield might differ among samples according to these processes. Such differences are expected to affect the rate difference in IPA decomposition and CO_2 generation because the reported photocatalytic decomposition pathway of gaseous IPA includes several reaction steps [11, 12]. Detailed analysis of the relation between characteristics of Fe-modified TiO_2 and the decomposition performance of various organic compounds should be undertaken in future work. The both Fe-modification processes could not provide visible light photocatalytic activity of Ti-HAp due to the difference in the bonding nature of the valence band of Ti-HAp and TiO_2.

2.4. Summary

In this chapter, anatase and rutile phases of TiO_2 with almost identical specific surface area were modified with Fe-base solutions using two different modification processes (MCG or CCC). Their photocatalytic activities under visible illumination were evaluated by the decomposition of gaseous IPA to CO_2. The Fe-modified rutile powders exhibited high visible light photocatalytic activity. The binding energy of O 2p by XPS analysis revealed that the valence band top of the samples prepared from CCC decreases concomitantly with increasing Fe concentration. These results suggest that a difference in modification process engenders different mechanisms of photocatalytic activity for Fe-modified TiO_2 under visible light. In case of MCG process, the electrons in the valence band are transferred directly to Fe(III) ions via IFCT, producing Fe(II) ions capable of reducing oxygen by multielectron reduction

processes. On the other hand, CCC process, the electrons are excited from the surface d sub-band, yielded by mixing between the surface Fe(III) levels and O 2p by the Ti–O–Fe interfacial bond to the conduction band of TiO_2. Because of the smaller initial bandgap, Fe modification by both processes is expected to be more effective for rutile than for anatase.

These Fe-modification processes were employed on Ti-HAp particles. The photocatalytic activities under visible illumination were evaluated by the decomposition of gaseous IPA. However, the Fe-modified Ti-HAp did not provide the visible light photocatalytic activity. The direct electron transfer from the valence band to Fe(III) via IFCT was insufficient because the valence band of Ti-HAp comprises the covalent bonding of PO_4^{3-}. The valence electrons are localized between P and O atoms, leading to the difficulty in electronic excitation from O atom to Fe atom. Moreover, the formation of the Ti–O–Fe interfacial bond yielding a surface d sub-band by CCC process might be insufficient due to the covalent nature of the valence band of Ti-HAp.

References

[1] H. Irie, S. Miura, K. Kamiya, K. Hashimoto, Efficient visible light-sensitive photocatalysts: grafting Cu(II) ions onto TiO_2 and WO_3 photocatalysts, *Chem. Phys. Lett.*, **457** (2008) 202–205.

[2] H. Irie, K. Kamiya, T. Shibanuma, S. Miura, D. A. Tryk, T. Yokoyama, K. Hashimoto, Visible light-sensitive Cu(II)-grafted TiO_2 photocatalysts: activities and X-ray absorption fine structure analyses, *J. Phys. Chem. C*, **113** (2009) 10761–10766.

[3] M. Miyauchi, Z. Liu, Z-G. Zhao, S. Anandan, H. Tokudome, Visible-light-driven superhydrophilicity by interfacial charge transfer between metal ions and metal oxide nanostructures, *Langmuir*, **26** (2010) 796–801.

[4] H. Yu, H. Irie, Y. Shimodaira, Y. Hosogi, Y. Kuroda, M. Miyauchi, K. Hashimoto, An efficient visible-light-sensitive Fe(III)-grafted TiO_2 photocatalyst, *J. Phys. Chem. C*, **114** (2010) 16481–16487.

[5] H. Tada, Q. Jin, H. Nishijima, H. Yamamoto, M. Fujishima, S. Okuoka, T. Hattori, Y. Sumida, H. Kobayashi, Titanium(IV) dioxide surface-modified with iron oxide as a visible light photocatalyst, *Angew. Chem. Int. Ed.*, **50** (2011) 3501–3505.

[6] M. Miyauchi, H. Irie, M. Liu, X. Qiu, H. Yu, K. Sunada, K. Hashimoto, Visible-light-sensitive photocatalysts: nanocluster-grafted titanium dioxide for indoor environmental remediation, *J. Phys. Chem. Lett.*, **7** (2016) 75–84.

[7] N. Serpone, D. Lawless, Spectroscopic, photoconductivity, and photocatalytic studies of TiO_2 colloids: naked and with the lattice doped with Cr^{3+}, Fe^{3+}, and V^{5+} cations, *Langmuir*, **10** (1994) 643–652.

[8] X. Liu, J. Ma, J. Yang, Visible-light-driven amorphous Fe(III)-substituted hydroxyapatite photocatalyst: characterization and photocatalytic activity, *Mater. Lett.*,

137 (2014) 256–259.

[9] M. Nishikawa, W. Yang, Y. Nosaka, Grafting effects of Cu^{2+} on the photocatalytic activity of titanium-substituted hydroxyapatite, *J. Mole. Catal. A: Chem.*, **378** (2013) 314–318.

[10] K. Pruethiarenun, T. Isobe, S. Matsushita, J. Ye, A. Nakajima, Comparative study of photoinduced wettability conversion between $[PW_{12}O_{40}]^{3-}$/brookite and $[SiW_{12}O_{40}]^{4-}$/brookite hybrid films, *Mater. Chem. Phys.*, **144** (2014) 327–334.

[11] Y. Ohko, K. Hashimoto, A. Fujishima, Kinetics of photocatalytic reactions under extremely low-intensity UV illumination on titanium dioxide thin films, *J. Phys. Chem. A*, **101** (1997) 8057–8062.

[12] S. A. Larson, J. A. Widegren, J. L. Falconer, Transient studies of 2-propanol photocatalytic oxidation on titania, *J. Catal.*, **157** (1995) 611–625.

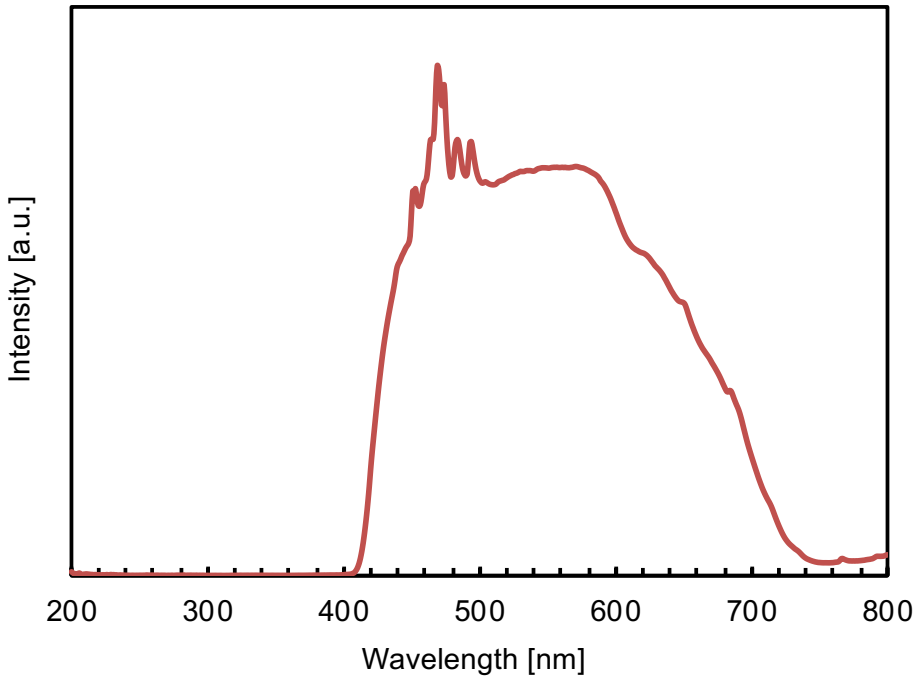

Figure 2.1 Light spectra of Xe lamp through the long-pass (L-42) filter.

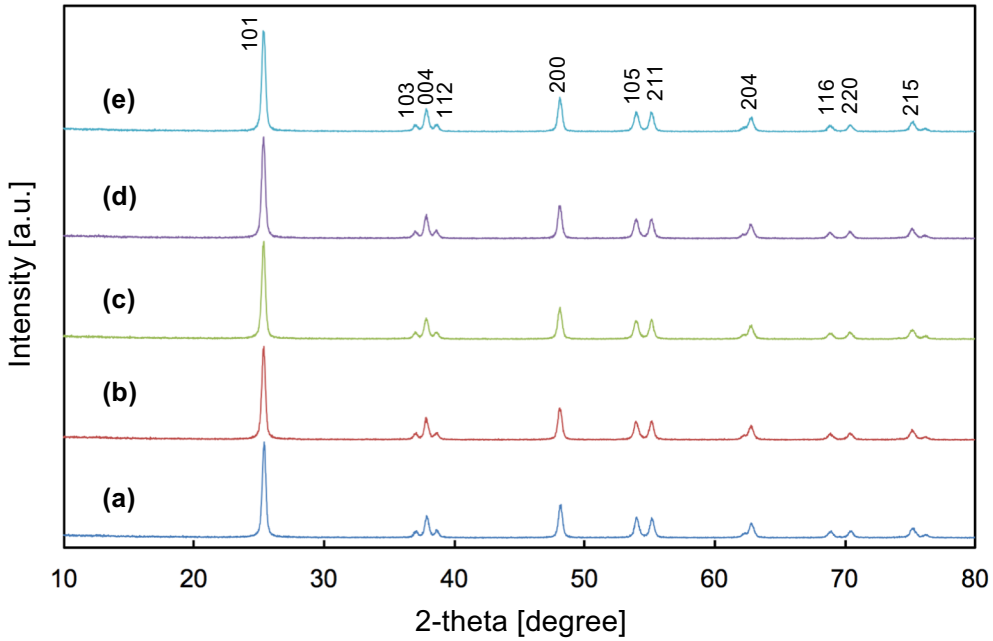

Figure 2.2 XRD pattern of the obtained powders: (a) anatase, (b) An-M1, (c) An-M2, (d) An-C1, and (e) An-C2.

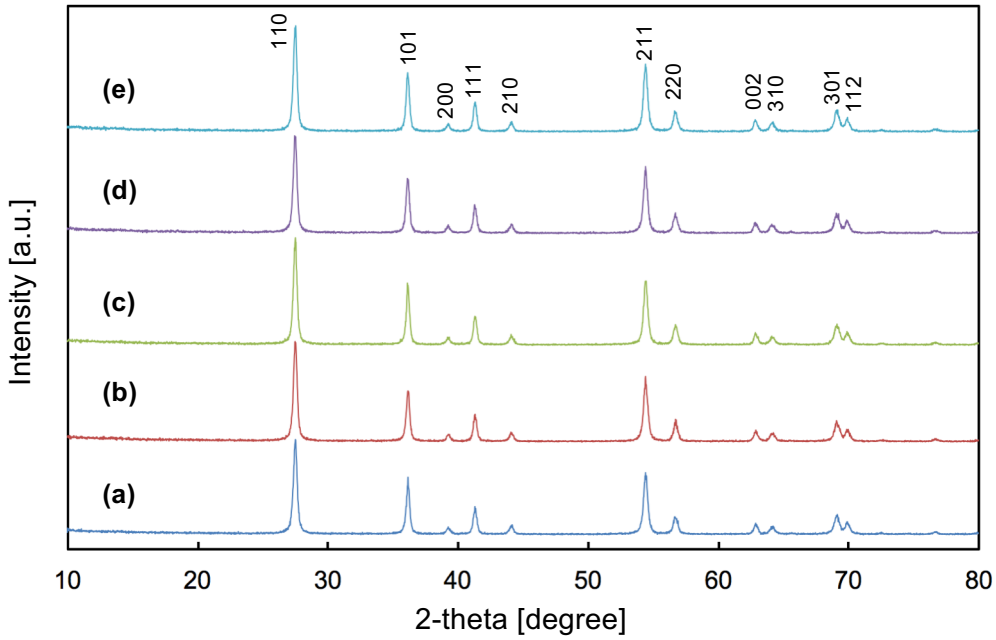

Figure 2.3 XRD pattern of the obtained powders: (a) rutile, (b) Ru-M1, (c) Ru-M2, (d) Ru-C1, and (e) Ru-C2.

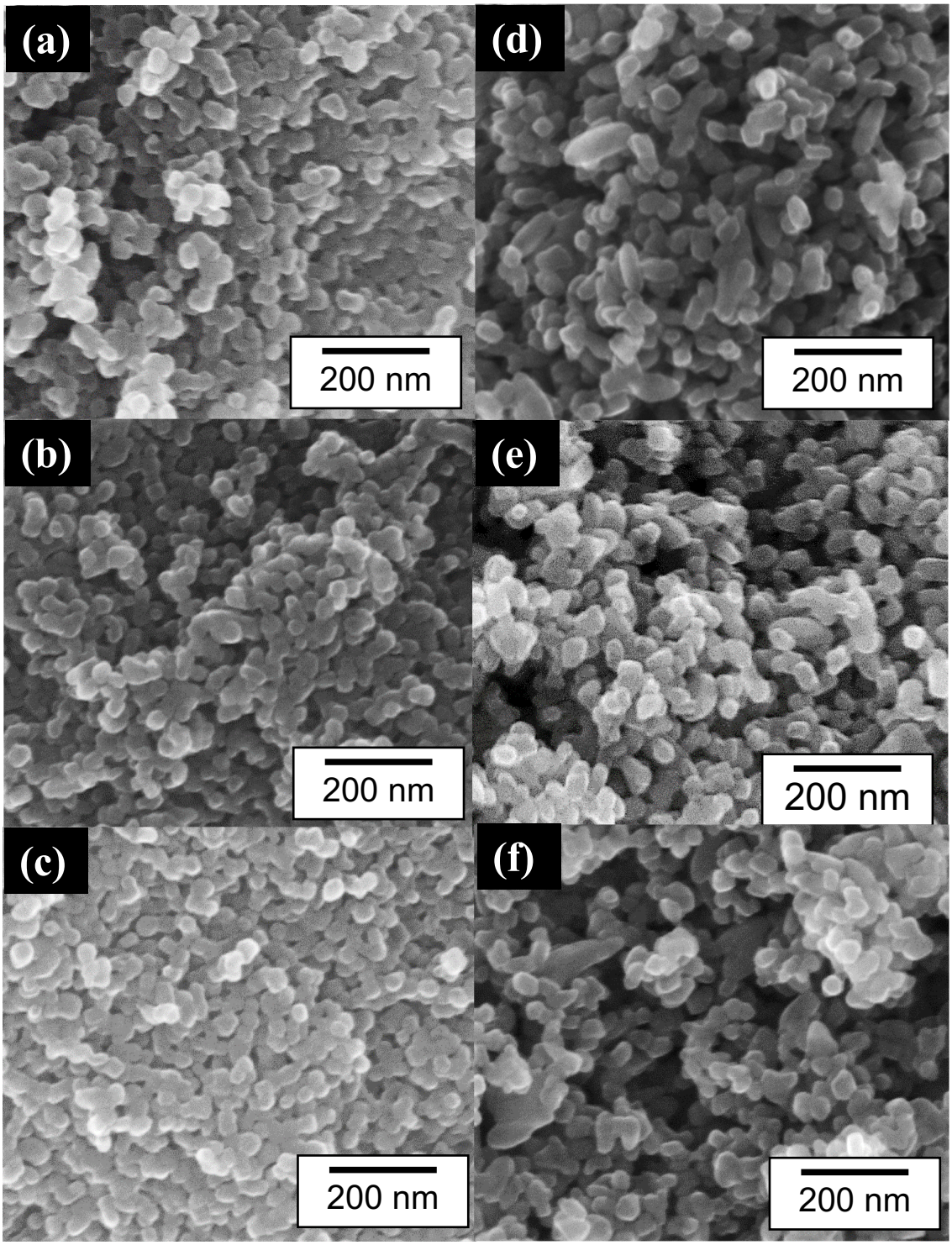

Figure 2.4 SEM micrographs of TiO_2 powders before and after Fe modification: (a) anatase, (b) An-C2, (c) An-M2, (d) rutile, (e) Ru-C2, and (f) Ru-M2.

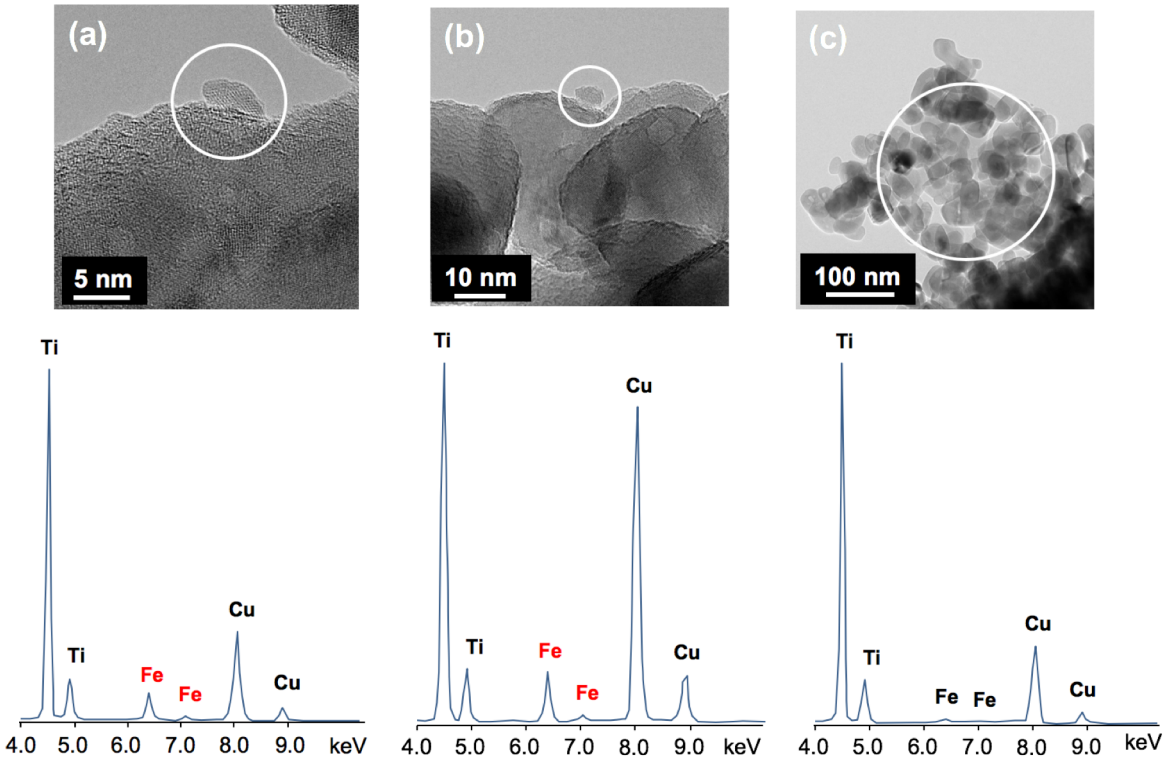

Figure 2.5 TEM micrographs and EDS spectra of Fe clusters on the surface of TiO_2 modified by MCG processing: (a) and (b) Fe-clusters and (c) entire particles. The white circles in the figure were areas of EDX analysis.

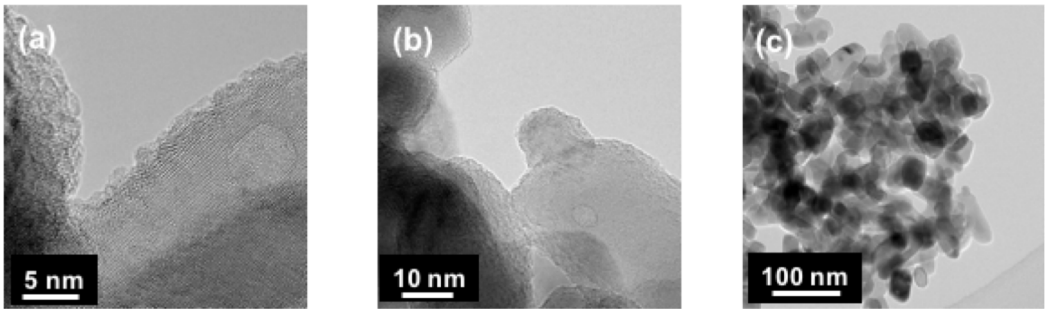

Figure 2.6 TEM micrographs of TiO_2 modified by CCC processing: (a) and (b) surface of particles, and (c) entire particles.

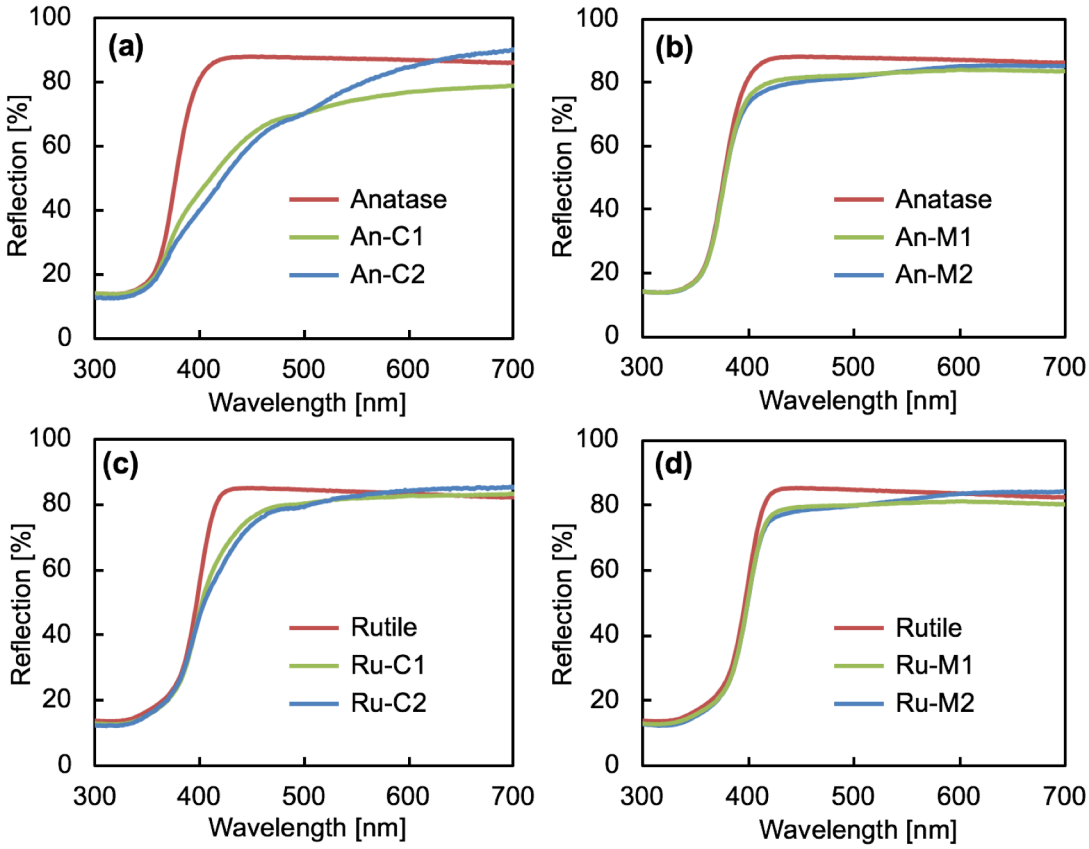

Figure 2.7 UV-vis spectra of obtained powders: (a) An-C1 and C2, (b) An-M1 and M2, (c) Ru-C1 and C2, and (d) Ru-M1 and M2.

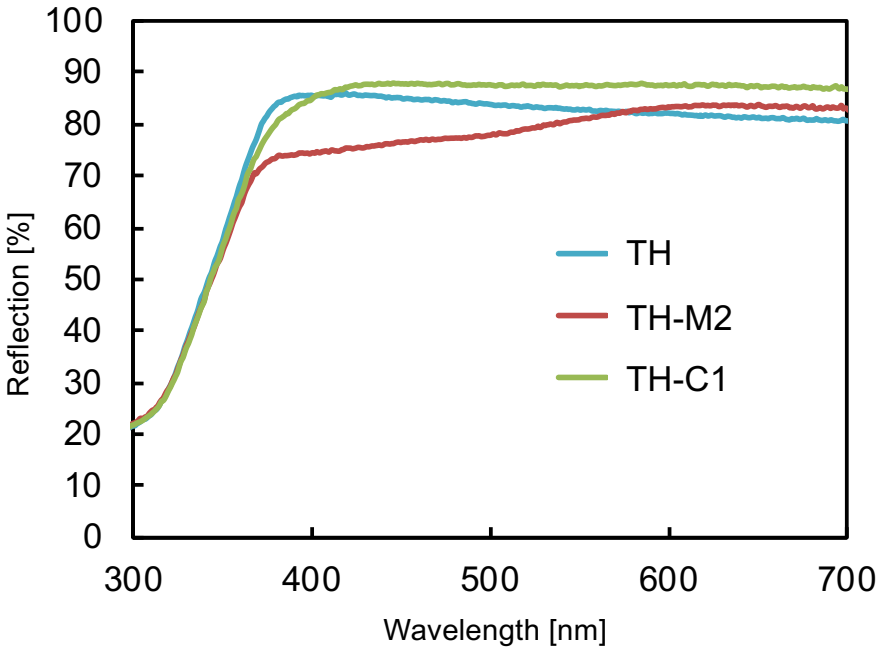

Figure 2.8 UV-vis spectra of Fe-modified Ti-HAp powders.

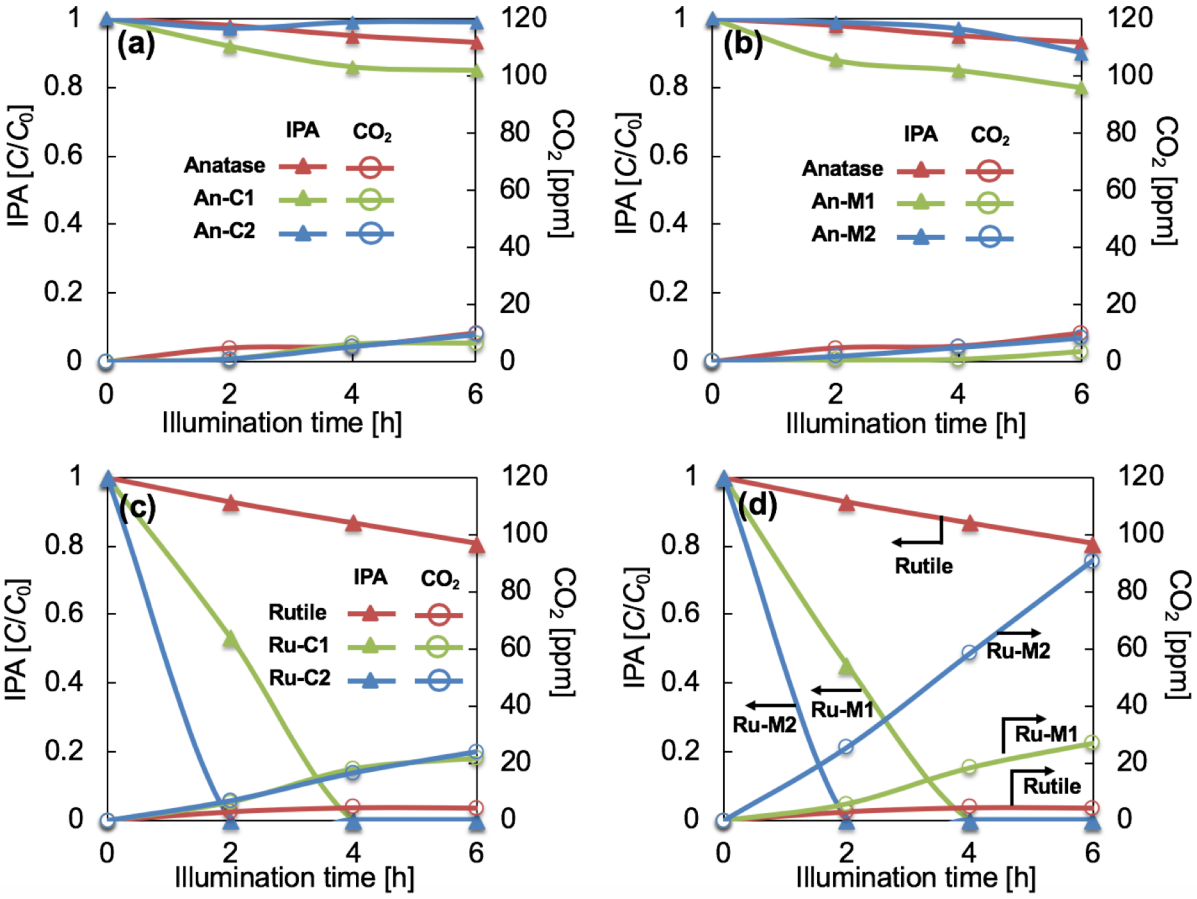

Figure 2.9 Concentration changes of IPA and CO_2 against light illumination time: (a) An-C1 and C2, (b) An-M1 and M2, (c) Ru-C1 and C2, and (d) Ru-M1 and M2.

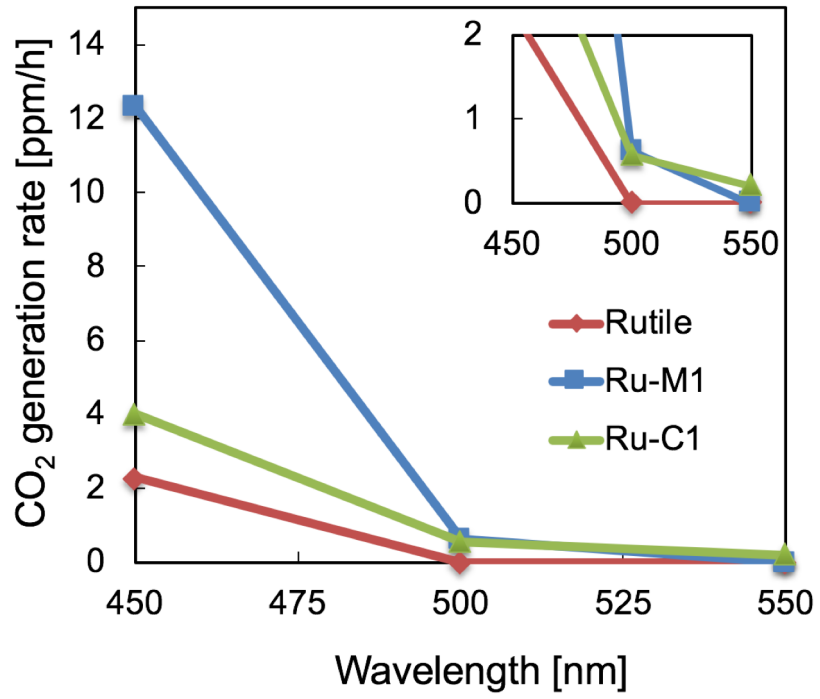

Figure 2.10 Action spectra of IPA decomposition for rutile, Ru-C1, and Ru-M1.

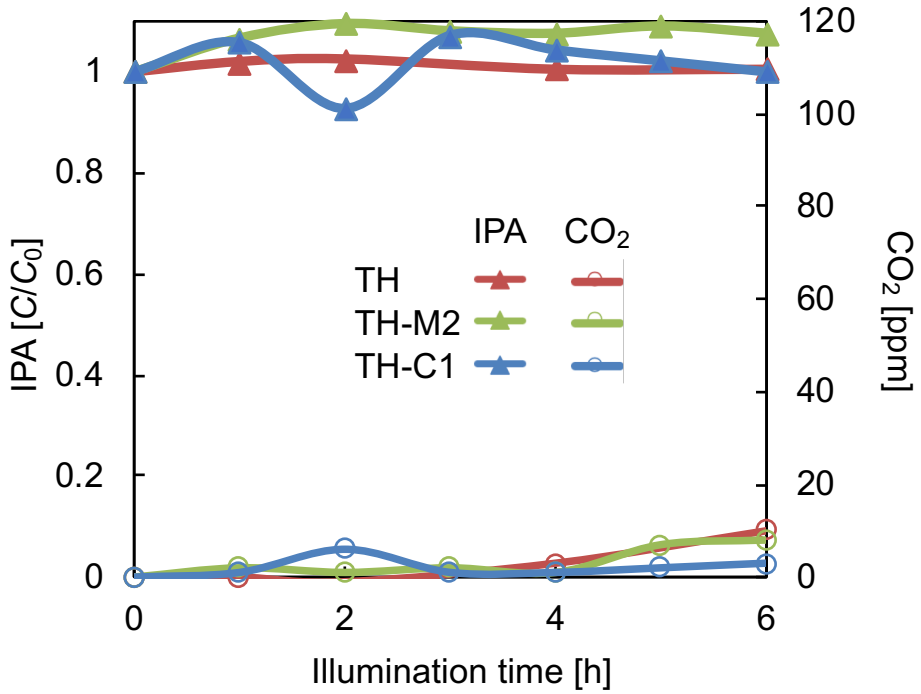

Figure 2.11 Concentration changes of IPA and CO_2 against light illumination time of Fe-modified Ti-HAps.

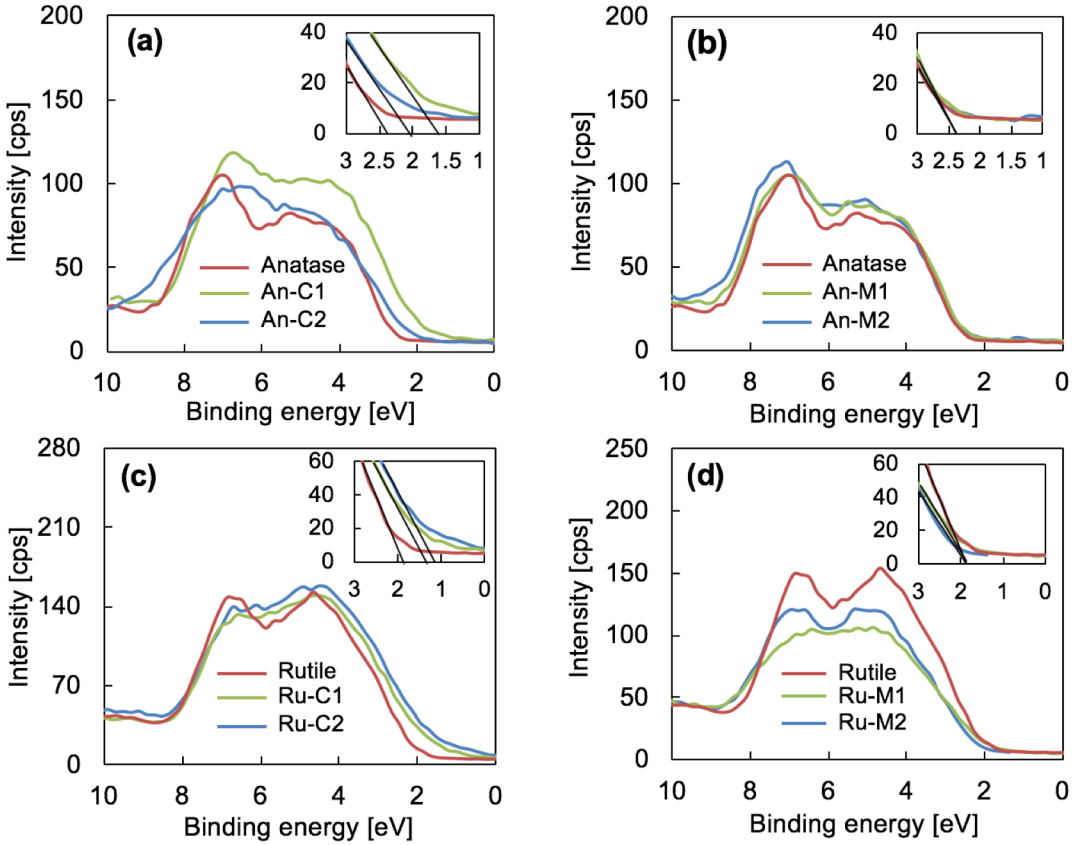

Figure 2.12 XPS spectra of the binding energy of O 2p of the powders: (a) An-C1 and C2, (b) An-M1 and M2, (c) Ru-C1 and C2, and (d) Ru-M1 and M2.

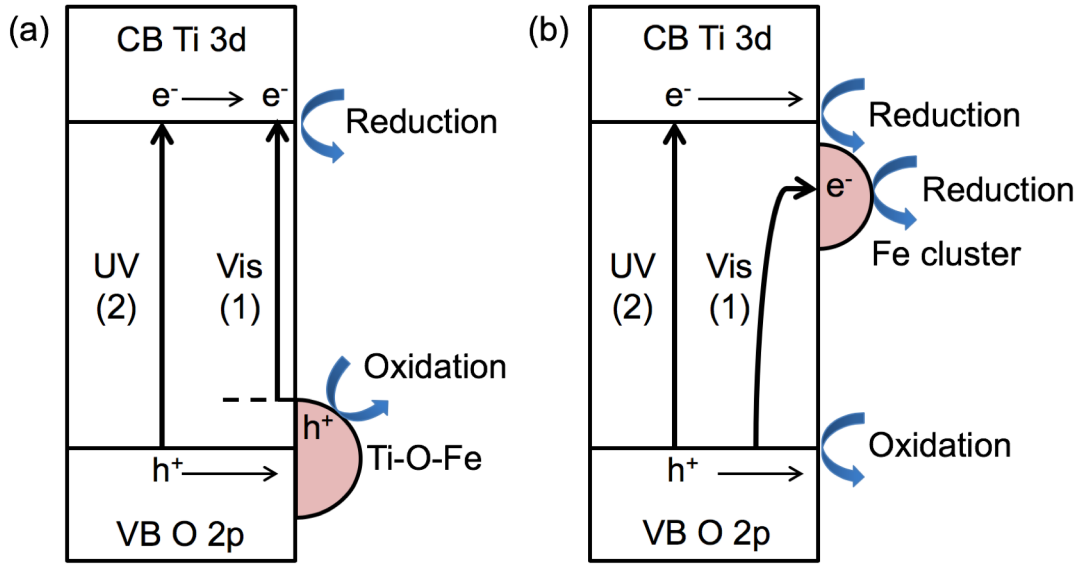

Figure 2.13 Energy diagram of Fe-modified TiO_2 by (a) CCC process and (b) MCG process.

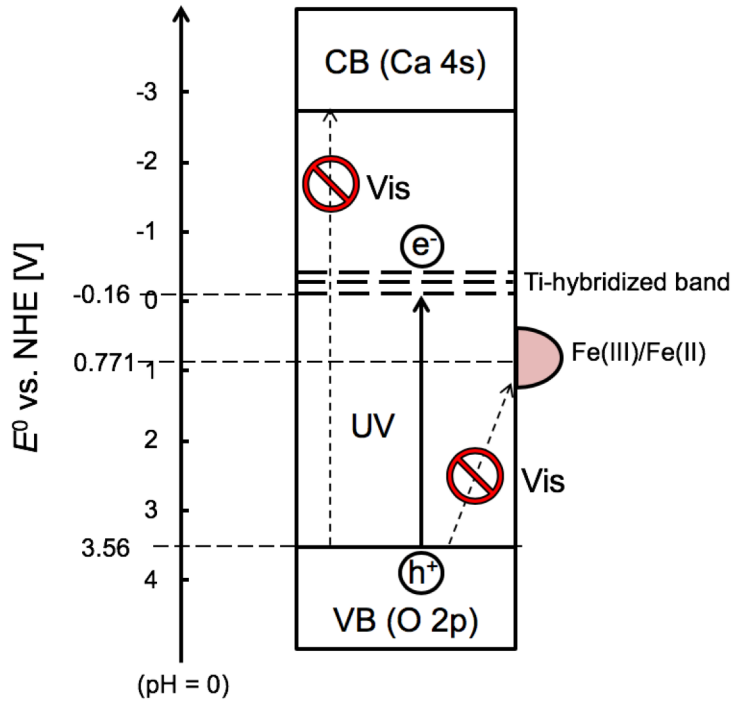

Figure 2.14 Energy diagram of Fe-modified Ti-HAp.

CHAPTER 3

Modification of Ti-HAp surface with a $CaMoO_4$ aqueous solution using impregnation and calcination cycle

3.1. Introduction

Titanium-substituted hydroxyapatite (Ti-HAp, $(Ca_{10-2x}, Ti_x, \square_x)(PO_4)_6(OH)_2$, □: defect in Ca site) possesses photocatalytic activity under UV illumination while retaining surface chemical properties of HAp [1–8]. Consequently, Ti-HAp exhibits good affinity with organic compounds. That affinity gives it characteristically higher adsorption capability than other normal oxides against various organic chemical species [3, 4]. For that reason, Ti-HAp is highly anticipated for anti-bacterial applications [7, 8]. The maximum substitutable Ti amount is limited to ca. 10 mol% of Ca to retain the HAp structure. Therefore, the photocatalytic activity of Ti-HAp itself is restricted [1]. Consequently, the primary photocatalytic activity of Ti-HAp is inferior to that of TiO_2. The high photocatalytic activity of Ti-HAp against various organic compounds is attributable to its excellent adsorption capability on their surface [9]. The enhancement of primary photocatalytic activity of Ti-HAp is demanding. Several attempts have been conducted by surface modification or doping [10, 11], their outcomes fell short of expectations. Although, we have tried various elements doping into either HAp or Ti-HAp, the results were not effective. Enhancement of the primary photocatalytic activity of Ti-HAp has not been achieved to date.

In contrast, MoO_4^{2-} is a tetrahedral oxoanion that is similar in many respects to PO_4^{3-}. Although ion exchange between MoO_4^{2-} and PO_4^{3-} in Ti-HAp is expected to be difficult because of their sizes (P=O, ca. 150 pm; P−O, ca. 160 pm; Mo−O, ca. 170 pm [12, 13]), MoO_4^{2-} might adsorb onto the surface Ca or Ti ion, where it might affect the charge transfer of

the material. For this chapter, we modified Ti-HAp using an aqueous solution of $CaMoO_4$ to avoid unnecessary ion exchange of the Ca sites in Ti-HAp. Then we examined the photocatalytic activity under UV illumination and discussed the role of Mo modification in photocatalytic activity.

3.2. Experimental procedure

3.2.1. Sample preparation and characterization

For this study, commercial Ti-HAp (Hautoform TA, $(Ca_{8.22}, Ti_{0.89}, \square_{0.89})(PO_4)_6(OH)_2$; Fuji Chemical Ind. Co. Ltd., Osaka, Japan) was used as a starting material. Reagent grade calcium molybdate ($CaMoO_4$; Wako Pure Chemical Industries Ltd., Osaka, Japan) was dissolved into distilled water (200 mL, 0.1 mM) at 80°C. After cooling the solution to room temperature, Ti-HAp powder (1 g) was added to the clear $CaMoO_4$ solution and was stirred for 5 min. The powder was filtered and washed several times with distilled water. Then, the powder was dried at 60°C for 24 h in air, followed by heating at 500°C for 1 h in ambient air. This firing was conducted to remove organic compounds and to convert hydroxides to oxides. This temperature was lower than the heating temperature in manufacturing commercial Ti-HAp process. For that reason, it will not provide a remarkable difference in the crystalline phase, morphology, or specific surface area of the starting Ti-HAp. These procedures were repeated several times (Y) to control the chemical composition of the surface. We also prepared samples for comparison using HAp (Taihei Chemical Industrial Co. Ltd., Osaka, Japan) instead of Ti-HAp under the same condition. Before the preparation, HAp powder was heated at 650°C for 1 h in ambient air (same temperature that used for commercial Ti-HAp before modification). The obtained samples are denoted in this report as X-AY, with X representing the base material (either TH for Ti-HAp or H for HAp), A standing for the

solvent (aqueous (A) solution), and Y signifying the repetitions.

Crystalline phases of the obtained samples were investigated using X-ray diffraction (XRD; XRD-6100, Shimadzu Corp., Japan) with Cu Kα radiation. The optical absorption spectra were measured using a UV-vis scanning spectrophotometer (V-650; Jasco Corp., Tokyo, Japan). The powder morphology was observed using a transmission electron microscope (JEM-2010F; JEOL Ltd., Tokyo, Japan). We evaluated the chemical composition using inductively coupled plasma analysis (Prodigy ICP; Teledyne - Leeman Labs, Hudson, NH, U.S.A.). Additionally, we measured the binding energies of the elements using X-ray photoelectron spectroscopy (XPS, ESCA model5500MT; PerkinElmer Inc., U.S.A.) using an Al Kα X-ray line (1486.6 eV). Specific surface areas were measured using Brunauer, Emmett and Teller (BET) method with N_2 (BEL SORP mini; Bel Japan Inc., Japan). Time of flight (TOF) powder neutron diffraction patterns were measured using iMATERIA diffractometer of J-PARC facility, Tokai, Japan [14]. The scattering angles, 2θ, were 155° and 35°. The neutron diffraction data were analyzed by Rietveld refinement using the computer program Z-Rietveld [15]. All refinements were conducted in space group $P6_3/m$ (No. 176) and used isotropic displacement parameter, which were not allowed to vary. The initial atomic positions of HAp were followed the reported value [16]. Then, Ti atoms and Mo atoms were introduced into the structure by substituted at Ca sites or P sites.

3.2.2. Photocatalytic activity, electron spin resonance, and photoluminescence measurements

Photocatalytic activity was evaluated according to the decomposition of gaseous 2-propanol (IPA). The powder samples (40 mg) are embedded homogeneously into a petri dish with area of 8.35 cm^2. Before evaluation, UV pre-illumination (ca. 0.7 mW/cm^2 at 355

nm) onto the sample powder was conducted for one night (more than 8 h) to remove organic compounds that had been adsorbed onto the surface. Then the dish was set at the center of a Pyrex glass vessel with a quartz lid (500 ml in volume). Subsequently, the vessel was sealed, followed by filling of the vessel with air (20 °C, 80% relative humidity). Then, 700 ppm of gaseous IPA was injected into the vessel. It was then stored in the dark. During this dark storage, the IPA concentration was evaluated using gas chromatography (GC-2014 with a flame ionization detector, a methanizer, and a column (Sunpak-A; Shimadzu Corp.); Shimadzu Corp., Tokyo, Japan) to confirm the adsorption equilibrium between the powder and gaseous IPA. After the adsorption equilibrium was confirmed (one night), light illumination was conducted. Then we applied UV illumination using a UV illuminator (LA-410UV-1; Hayashi Watch Works, Tokyo, Japan) equipped with a Hg-Xe lamp through a liquid light guide with no filter. The UV illumination intensity was adjusted to 1 mW/cm^2. During this light illumination, IPA and CO_2 concentrations were measured every 1 h using the same gas chromatography. A schematic illustration of photocatalytic activity measurements and the light source spectra are presented in **Fig. 3.1**.

For electron spin resonance (ESR) measurements, the sample powder was placed in a quartz glass sample tube with a Young vacuum joint and a stopcock. Then the air was evacuated from the sample tube. Measurements were taken at 90–100 K using an ESR spectrometer (EMXnano; Bruker Analytik, Germany) under light using a UV illuminator (LA-410UV-1; Hayashi Watch Works, Tokyo, Japan) equipped with a 200 W Hg-Xe lamp. The ESR measurement conditions were microwave frequency of 9.62 GHz, microwave power of 1 mW, and field modulation of 0.05 mT. The photoluminescence (PL) emission spectra were measured using a fluorescence spectrophotometer (F-7100; Hitachi Ltd., Japan) with a 150 W Xe lamp as an excitation light source. The excitation wavelength was 280 nm. The

scanning rate was 1200 nm/min. The PMT voltage was 700 V. Widths of excitation emission slits were 5.0 nm.

3.2.3. Density functional theory calculation

To elucidate the role of the MoO_x-modified Ti-HAp, we specifically examined a room-temperature equilibrated system and its related electronic structure. Ti-HAp has the $P6_3/m$ space group (No. 176), with the lattice parameter and bond angle defined respectively as $a = b = 9.4212$ Å, $c = 6.8847$ Å, $\alpha = \beta = 90°$, and $\gamma = 120°$. The photocatalytic system was modeled by placing the Mo-modified Ti-HAp slab substrate in a supercell. The exposed surface of the Mo-modified Ti-HAp was selected as the (001) surface. The supercell contained the photocatalyst substrate composed of 1 Mo, 8 Ti, 72 Ca, 47 P, 225 O, and 33 H atoms with 16 Mo atoms forming a metallic cluster added to the surface. The exposed surface area on the slab was $2a \times 2b \times \sin(120°)$ (= 307.47 $Å^2$). The supercell thickness was set as 25.0 Å, whereas the slab representing the substrate occupied about $2c$ (13.7694 Å) of the total supercell thickness. The remaining empty space is available to accommodate the Mo metallic cluster, 2-propanol (IPA), oxygen, and nitrogen. Then the structure equilibrated to 300 K was obtained by dynamic simulation within the Car–Parrinello Molecular Dynamic (CPMD) framework [17] by exposing the model to 300 K conditions for about 0.64 picoseconds. The electronic structure of the Mo-modified Ti-HAp was obtained by solving a Kohn–Sham equation with local spin density approximation using first-principles method.

3.3. Results and discussion

3.3.1. Characteristics of obtained samples

Figure 3.2 presents XRD patterns of Ti-HAp before and after Mo modification. All

peaks in the XRD patterns of the obtained samples were identified as a HAp structure with $P6_3/m$ (No.176) space group. Differences in intensity among the peaks before and after the Mo modification were not remarkable. The specific surface areas of all samples were almost equivalent (35–39 m^2/g).

To investigate the structure changes in Ti-HAp after the Mo-modification, Rietveld refinement was conducted for Ti-HAp and TH-A3 based on the neutron diffraction data using the computer program Z-Rietveld [15]. From the refinement results, it was suggested that Ti atoms are substituted with Ca atoms in both Ca(I) site and Ca(II) site similar to the reported result [18]. However, we were unable to identify the ratio of Ti atoms in Ca(I) and Ca(II) because it depended on the Ca deficient positions. Therefore, we compared the refinement results of Ti-HAp and TH-A3 by assuming that there was no Ti and Mo atom present in both sample. **Figure 3.3** shows the result of fitting between the observed and calculated for neutron diffraction patterns of Ti-HAp and TH-A3 without Ti and Mo atoms in the structure. The detailed refinement parameters and atomic positions are listed in **Table 3.1**. These samples exhibit similar results in both lattice parameters and atomic positions suggesting that Ti-HAp and TH-A3 possess almost identical crystal structure. For TH-A3, when Mo was substituted with Ca or P, the R_{wp} factor increased indicated that the possibilities of ion exchange between Mo and Ca or Ti at Ca sites, and ion exchange between MoO_4^{2-} and PO_4^{3-} at P site were low. Therefore, Mo modification did not change the structure of Ti-HAp suggested that there was no Mo-doping into the Ti-HAp structure and that the modified Mo atoms exists as a different form.

Figure 3.4 portrays TEM images of Ti-HAp obtained before and after three Mo modifications (TH-A3). Both samples have rod-like morphology with 50–80 nm average particle length. A cluster-like area with size of 1–2 nm was observed on the TH-A3 powder

surface (denoted by circles and arrows in **Fig. 3.4(b)** and **3.4(c)**). However, analysis of the chemical compositions of these parts using EDS was not feasible because of insufficient durability against damage by the focused electron beam. Based on the processing procedures, the chemical composition (described below), and their morphology, it was inferred that clusters observed in TEM were $CaMoO_4$ or MoO_x.

Figure 3.5 presents UV-Vis spectra of Ti-HAp before and after Mo modification. No absorption band except for the absorption band of Ti-HAp was observed. It is noteworthy that the absorption edge of crystalline $CaMoO_4$ is on the smaller wavelength side than that of Ti-HAp (see **Fig. 3.6**). The bandgaps of the samples calculated from UV-vis spectra by assuming direct transition were 3.72 eV for all samples, which were approximately equal to the reported values for Ti-HAp [6, 18]. Detailed inspection of the valence band (O 2p) top of Ti-HAp and TH-A5 obtained by XPS revealed that they are more positive (0.480 eV) against those of TiO_2, as shown in **Fig. 3.7**, for which the band position was clarified in our earlier study [19]. Therefore, the valence band position of Ti-HAp was estimated from the bandgap energy as 3.560 V (vs. NHE, pH = 0); the Ti-hybridized band was estimated approximately -0.160 V (vs. NHE, pH = 0).

Table 3.2 presents chemical compositions obtained from ICP analysis. At first, we conducted XPS analysis for the Mo characterization. However, because of the very low concentration, the peak intensity against the background noise level was insufficient. Reliable elucidation related to the amount and valence was infeasible. Therefore, we confirmed Mo concentration using ICP analysis in this study. For the peak of Ti 2p and O 1s, no change was found after the Mo-modification. The Mo concentration in the table was the atomic ratio against Ti in Ti-HAp. It is noteworthy that the atomic ratio between Ca and Ti (Ca/Ti) was almost constant (9.1~9.4) in these samples. The concentration of Mo increased concomitantly

with increasing modification time up to three times the original concentration. Subsequently, the concentration of Mo decreased gradually, which might indicate that the excessive amount of Mo or Ti-HAp surface dissolved into the $CaMoO_4$ solution. Some molybdenum oxides possess a certain solubility against water (ca. 0.5 g/ 100 mL water at 300 K for MoO_3). Therefore, the cluster might dissolve into water if it is MoO_x. However, to date, we have insufficient confidence about the reason for the Mo concentration presented in **Table 3.2**. Investigation of the effects of the impregnation time period might provide some information. This work should be addressed in future studies.

3.3.2. Photocatalytic activity and density functional calculation

Figures 3.8(a) and **3.8(b)**, respectively portray the concentration change of IPA and CO_2 against the UV illumination time. The value of C_0 presented on the y-axis of **Fig. 3.8(a)** shows the initial concentration of IPA before UV illumination. The practical average value of C_0 is around 622 ppm. The IPA concentration reaches zero within 6 h for Ti-HAp, within 3 h for TH-A1, and within 2 h for the remaining samples. Although little difference was observed among TH-A2 to TH-A5, the CO_2 generation rates of these samples differed because several steps exist in the decomposition pathway from IPA to CO_2 by photocatalytic oxidation [20–23]. **Table 3.2** shows that the CO_2 generation rate (K_{CO2}) at the initial stage was calculated in the linear range of 0–6 h of the relation between the CO_2 generation and the UV illumination time. The highest CO_2 generation rate of the MoO_x-modified Ti-HAp (131 ppm/h) was about nine times higher than that of Ti-HAp (14 ppm/h). **Figure 3.9** presents the relation between the Mo amount and the CO_2 generation rate. From this relation, the photocatalytic activity under UV illumination of the MoO_x-modified Ti-HAp was found to be enhanced as the Mo concentration increased. **Figure 3.10** shows that this photocatalytic

activity was not degraded significantly through at least three repeated measurements. Although the degree of activity increase was less remarkable (5 times) than IPA, similar trend was obtained also on the decomposition of acetaldehyde (**Fig. 3.11**) under the same condition. This difference should be attributable to the difference in adsorption capability against gaseous species and their decomposition pathway [24].

Further detailed experimentation revealed that MoO_x-modified HAps (specific surface area of ca. 29 m^2/g) prepared using the same procedures as those used for MoO_x-modified Ti-HAps exhibit little absorption in UV-vis spectra and decomposition activity (see **Fig. 3.12** and **3.13**). These results imply that Mo modified using this treatment does not provide photocatalytic activity by itself, but that it efficiently enhances the photocatalytic activity of Ti-HAp under UV illumination.

For computer modeling, we specifically examined the structure of Mo-modified Ti-HAp with a 16-atom Mo cluster placed on the surface. In a bulk metallic state, Mo crystallizes in the form of a body-centered cubic structure belonging to the space group $Im\bar{3}m$ (No. 229). The reported unit cell lattice constant is 3.1461 Å, the shortest Mo–Mo distance being 2.7246 Å [25]. For the Ti-HAp structure, Ca atoms were substituted with Ti atoms in both the Ca(I) site and Ca(II) site at 10 mol% of Ca atoms [18]. In addition, one unit of tetrahedral PO_4^{3-} was substituted with tetrahedral MoO_4^{2-} in the Ti-HAp structure. When the simulation approaches thermal equilibrium, the Mo cluster displaces closer to the O atom at the surface. Eventually, Mo atoms of the cluster are adsorbed to O atoms of Ti-HAp, forming a stable Mo–O oscillating dynamically around 2.16 Å [26] and keeping the Mo cluster anchored to the surface. The initial shape of the Mo cluster changed, accompanied by shrinkage of the Mo–Mo distance from 2.7 Å to about 2.3–2.7 Å. Details of the electronic properties were investigated for the equilibrated system. **Figure 3.14** presents the atomic configuration of the

surface in the system.

A projection of eigen wavefunction onto atomic orbitals produced the result presented in **Fig. 3.15**. The conduction band comprises Ca 4s orbitals, whereas the lowest unoccupied band is composed predominantly by Ti 3d and Mo 4d contributions. **Figure 3.15(d)** portrays the occupied states of Mo 4d orbitals, which are situated in the energy range from the O 2p band to the middle of Ti-HAp band gap energy. From these energy band levels, one can infer that an electron can be feasibly excited from the valence band (O 2p orbitals) to the Ti 3d unoccupied band, which is hybridized with the unoccupied Mo 4d band then transferred to Mo 4d orbitals of the Mo metallic cluster. Therefore, the excited electron is separated from the hole in the valence band, providing carrier separation [27].

Among the Mo 4d components, two positions of Mo atoms exist in this system. The first position is a Mo atom forming MoO_4^{2-} tetrahedral that substituted with PO_4^{3-} tetrahedral in Ti-HAp structure. The second position is Mo atoms forming the Mo metallic cluster. **Figures 3.15(g)** and **3.15(h)** respectively present the contributions of Mo 4d orbitals of Mo1, which is located inside the Ti-HAp slab layer as MoO_4^{2-} tetrahedral structure, and Mo4, which is on the Mo metallic cluster. The Mo 4d components of Mo1 are located only in the unoccupied state from -0.8 to 3.0 eV. However, the Mo 4d components of Mo4, which represent all 4d components of the metallic Mo cluster (**Fig. 3.15(d)**), are located in the energy range of -4.0 to 3.0 eV, indicating that only the Mo atoms forming the Mo metallic cluster are involved in the increase of photocatalytic activity. These results suggest that Mo-doping by exchanging PO_4^{3-} with MoO_4^{2-} tetrahedral does not increase photocatalytic activity. Moreover, we can infer that an electron excited from O 2p (valence band) to Ti-Mo hybridized band can transfer to the Mo cluster. Consequently, the excited electron is separated from the hole, providing efficient carrier separation.

For this study, we specifically examined two extreme cases: Mo^{6+} (MoO_4^{2-}) and Mo^0 (metallic) because the intermediate state can be inferred from the results. In the case of Mo^{5+} or Mo^{4+}, electrons are injected to the d-band of MoO_x. The d-levels filled by the injected electron should appear around the highest occupied level in **Fig. 3.15**. **Figure 3.16** presents electronic structure of Mo species obtained by projection onto atomic orbitals of the MoO_x-modified Ti-HAp. **Figure 3.16(b)** is on the 4d component of Mo1 of MoO_4 tetrahedral (same as **Fig. 3.15(g)**). The valence state of Mo in the MoO_4 was calculated as ~+6. **Figure 3.16(a)** is on that of MoO_3 which was artificially prepared by moving only one oxygen atom from a MoO_4 to the vicinity of Ca position with taking care so as not to bringing much stress to the system and, as a result of this moving, MoO_3 was exposed at the surface of Ti-HAp. The valence state of Mo in MoO_3 was calculated as ~+5. The electrons in MoO_3 are clearly injected to Mo 4d orbitals like Mo metallic cluster. In the case of $CaMoO_4$, which includes Mo^{6+}, the electronic structure is expected to be similar to the tetrahedral MoO_4^{2-} doped into Ti-HAp, which has already been demonstrated in our simulation model by the Mo (marked by number 1) O_4 structure. Actually, the MoO_4 structure is located in the lower part in the outer range of **Fig. 3.14**. These results imply that the Mo 4d band can be partially occupied by electrons, if the structure of MoO_x^{n-} ($x < 4$), which means Mo^{m+} ($m < 6$), can exist on the surface. Also, the highest occupied level of the MoO_x^{n-} can approach or coincide with the Ti 3d band bottom. Therefore, MoO_x^{n-} ($x < 4$) can also involve the increase of photocatalytic activity. Consequently, according to this calculation, the cluster seems to be MoO_x.

3.3.3. Electron spin resonance and photoluminescence measurements

Figure 3.17 portrays ESR spectra and the effect of UV illumination for Ti-HAp and MoO_x-modified Ti-HAp (TH-A3). Both samples gave the signal in the dark at 344 mT (g =

1.999) corresponding to that of oxygen vacancy or crystalline defects [28, 29], suggesting some defects that arise from the substitution of Ti atom into the Ti-HAp structure. From UV illumination, the signal of adsorbed oxygen radical was observed at 334 mT (g = 2.057) [30, 31] for both samples, indicating that a slight amount of adsorbed oxygen molecules exists on the sample surface. Signals attributable to trapped holes and trapped electrons were observed respectively at 341 and 343 mT (g = 2.014 and 2.004) and 346 mT (g = 1.988) [32, 33] for both samples. For the TH-A3 sample, the signal of Mo(V) was observed at 358 mT (g = 1.924) [34] under UV illumination, as presented in **Fig. 3.17(b)**. As described above, because of the quite low Mo concentration against Ti, evaluation of the valence of Mo in the cluster by XPS was not feasible. However, based on the starting materials and processing conditions (firing at 500°C in ambient air atmosphere), one can expect that the clusters are $CaMoO_4$ or MoO_x and that their dominant valence should be Mo(VI). The ESR results indicate that Mo(VI) of the cluster was reduced to Mo(V) by receiving the photo-excited electrons, probably from the Ti-hybridized band. This electron transfer process provides charge separation that enhances the photocatalytic activity. It is noteworthy that this Mo(V) signal was not observed for MoO_x-modified HAps even under UV illumination, which means that this charge transfer is specific to MoO_x-modified Ti-HAp.

Figure 3.18 presents the PL emission spectra of Ti-HAp and MoO_x-modified Ti-HAp examined at wavelengths of 300–600 nm. For all samples, the PL emission spectra appear at wavelengths of 300–590 nm. The PL emission peaks visible at wavelengths of 370–550 nm are attributable to excitonic PL, which mainly result from surface oxygen vacancies and defects of Ti-HAp particles [35, 36]. Actually, Ti-HAp possesses many defects at Ca sites because of the charge compensation maintained when Ca was substituted with Ti. Therefore, the crystal defects might involve its recombination. After Mo-modification, TH-A2 and

TH-A3 showed lower PL emission intensities near the band–band PL peak (335 nm for the bandgap energy of 3.72 eV), which indicates that the recombination rate of photoinduced electron–hole pairs near the Ti-hybridized band decreased. That decrease in turn suggests that the electrons in the valence band were excited to the Ti-hybridized band. Thereafter, they migrate to the cluster, which suppresses the recombination of electron–hole pairs.

3.3.4. Feasible electron transfer mechanism

Figure 3.19 presents a schematic illustration of the expected charge transfer mechanism of MoO_x-modified Ti-HAp. Under UV illumination, the electrons in the valence band are excited to the Ti-hybridized band. Then the excited electrons can transfer to the cluster because the potential of Ti-hybridized band (E^0 = -0.160 V, vs. NHE, pH = 0) is lower than that of Mo(VI)/Mo(V) (E^0 = 0.400 V, vs. NHE, pH = 0) [37] or MoO_3/MoO_2 (E^0 = 0.320 V, vs. NHE, pH = 0) [38]. It is noteworthy that Mo(IV) is inert for ESR analysis and that Mo(V) is not stable in an ambient air atmosphere. The electrons transferred from the Ti-hybridized band to the clusters can reduce oxygen (O_2/H_2O_2, E^0 = 0.695 V, vs. NHE, pH = 0 [39]) similarly to Cu(II)-modified TiO_2 and WO_3 [40], although photoinduced holes remain in the valence band, where they can oxidize organic compounds such as IPA and acetone. This result represents one plausible explanation for the electron transfer to oxygen. Further detailed investigations must prove this pathway. However, this process suppresses recombination of the photoinduced electron–hole pairs, causing the increase in photocatalytic activity. According to the UV-Vis spectra, the direct electron transfer from the valence band to the cluster via interfacial charge transfer seems unlikely to occur, probably because of the bonding nature of PO_4^{3-}, as described in an earlier report [11]. The present study revealed that 0.4–0.5 mol% is an optimum concentration for Mo-modification (**Fig. 3.9**). A plausible

explanation of this amount is an appropriate concentration for the balance between oxidation and reduction sites in the surface of Ti-HAp. The overall activation mechanism for Mo modification is apparently similar to the case of Cu modification [11]. However, Mo modification was more efficient than the case of Cu modification. Chemical affinity onto the Ti-HAp surface (MoO_4^{2-} is a similar tetrahedral oxoanion with PO_4^{3-}), the redox potential position, the firing procedure (firing is not done in the case of Cu modification), and the concentration of modified elements are candidate factors for this difference. The contribution of these factors to the activity difference between Cu and Mo modifications must be addressed in future studies.

Because molybdenum oxides possess a certain solubility against water, it is inappropriate to compare photocatalytic activity measurements using water purification. Moreover, the preparation of thin films using Mo-doped Ti-HAp powder with sufficient density, strength and repeatability onto the electrodes was not easy. Therefore, we have not conducted photocurrent experiments, but conducted PL and ESR measurements in this study to discuss the mechanism.

This study demonstrated that Mo modification is an effective strategy to enhance the photocatalytic activity of Ti-HAp. Results reported in the literature reveal that MoO_3 itself possesses antibacterial properties [41–44]. Therefore, this material might exhibit antibacterial and antivirus properties both in the dark and under UV illumination. Detailed investigations of this property will be undertaken in future studies.

3.4. Summary

For this study, we modified Ti-HAp with $CaMoO_4$ aqueous solution and evaluated UV light photocatalytic activity by the decomposition of gaseous IPA. After Mo modification, the

crystal structure, morphology, light absorption, and specific surface area were almost identical. Small (ca. 1 nm) clusters were observed on the surface of MoO_x-modified Ti-HAp. The MoO_x-modified Ti-HAp exhibited higher photocatalytic activity than Ti-HAp did. The photocatalytic activity of the MoO_x-modified samples increased concomitantly with increasing Mo concentration until 0.5% against Ti. Computer modeling indicated that MoO_4^{2-}doping into Ti-HAp structure plays no important role for activity increase. Results of ESR and PL analyses elucidated that the electron transfer from Ti 3d band to the MoO_x (Mo^{n+} ($n < 6$)) or Mo metallic cluster via wavefunction hybridization between the Ti 3d and the Mo 4d orbitals can suppress the recombination of photoinduced electron–hole pairs.

References

[1] M. Wakamura, K. Hashimoto, T. Watanabe, Photocatalysis by calcium hydroxyapatite modified with Ti(IV): albumin decomposition and bactericidal effect, *Langmuir*, **19** (2003) 3428−3431.

[2] K. Kandori, M. Oketani, M. Wakamura, Decomposition of proteins by photocatalytic Ti(IV)-doped calcium hydroxyapatite particles, *Colloids Surf. B: Biointerfaces*, **102** (2013) 908−914.

[3] K. Kandori, T. Kurodam, M. Wakamura, Protein adsorption behaviors onto photocatalytic Ti(IV)-doped calcium hydroxyapatite particles, *Colloids Surf. B: Biointerfaces*, **87** (2011) 472−479.

[4] K. Kandori, M. Oketani, M. Wakamura, Effects of Ti(IV) substitution on protein adsorption behaviors of calcium hydroxyapatite particles, *Colloids Surf. B: Biointerfaces*, **101** (2013) 68−73.

[5] N. Yoshida, T. Ishida, C. Saiki, M. Wakamura, H. Osaki, K. Hashimoto, T. Watanabe, Preparation of transparent thin film of novel apatite-based photocatalyst, *Chem. Lett*., **34** (2005) 1666−1667.

[6] A. Tsuruoka, T. Isobe, S. Matsushita, M. Wakamura, A. Nakajima, Comparison of photocatalytic activity and surface friction force variation on Ti-doped hydroxyapatite and anatase under UV illumination, *J. Photochem. Photobiol. A: Chem*., **311** (2015) 160−165.

[7] M. Nakazawa, M. Yamada, M. Wakamura, H. Egusa, K. Sakurai, Activation of osteoblastic function on titanium surface with titanium-doped hydroxyapatite nanoparticle coating: an in vitro study, *Int. J. Oral & Maxillofacial Implants*, **32** (2017) 779−791.

[8] M. Wakamura, Novel photocatalytic titanium apatite for environmental purification technology, J. *Soc. Inorg. Mater. Jpn.,* **13** (2006) 516−519. [in Japanese]

[9] Q. Li, X. Feng, X. Zhang, H. Song, J. Zhang, J. Shang, W. Sun, T. Zhu, M. Wakamura, M. Tsukada, Y. Lu, Photocatalytic degradation of bisphenol A using Ti-substituted hydroxyapatite, *Chinese J. Catal.*, **35** (2014) 90−98.

[10] M. Wakamura, H. Tanaka, Y. Naganuma, N. Yoshida, T. Watanabe, Surface structure and visible light photocatalytic activity of titanium-calcium hydroxyapatite modified with Cr(III), *Adv. Powder Technol.*, **22** (2011) 498−503.

[11] M. Nishikawa, W. J. Yang, Y. Nosaka, Grafting effects of Cu^{2+} on the photocatalytic activity of titanium-substituted hydroxyapatite, *J. Mol. Catal. A Chem.*, **378** (2013) 314−318.

[12] J. Herzfeld, R. G. Griffin, R. A. Haberkorn, Phosphorus-31 chemical-shift tensors in barium diethyl phosphate and urea-phosphoric acid: model compounds for phospholipid head-group studies, *Biochemistry*, **17** (1978) 2711−2718.

[13] F. D. Hardcastle, I. E. Wachs, Determination of molybdenum-oxygen bond distances and bond orders by Raman spectroscopy, *J. Raman Spectroscopy*, **21** (1990) 683−691.

[14] T. Ishigaki, A. Hoshikawa, M. Yonemura, T. Morishima, T. Kamiyama, R. Oishi, K. Aizawa, T. Sakuma, Y. Tomota, M. Arai, M. Hayashi, K. Ebata, Y. Takano, K. Komatsuzaki, H. Asano, Y. Takano, T. Kasao, IBARAKI materials design diffractometer (iMATERIA)−versatile neutron diffractometer ar J−PARC, *Nucle. Instru. Met. Phys. Res. A*, **600** (2009) 189−191.

[15] R. Oishi, M. Yonemura, Y. Nishimaki, S. Torii, A. Hoshikawa, T. Ishigaki, T. Morishima, K. Mori, T. Kamiyama, Rietveld analysis software for J−PARC, *Nucle. Instru. Met. Phys. Res. A*, **600** (2009) 94−96.

[16] M.I. Kay, R.A. Young, Crystal structure of hydroxyapatite, *Nature*, **204** (1964) 1051−1053.

[17] R. Car, M. Perrinello, Unified approach for molecular dynamics and density-functional theory, *Phys. Rev. Lett*., **55** (1985) 2471−2474.

[18] M. Tsukada, M. Wakamura, N. Yoshida T. Watanabe, Band gap and photocatalytic properties of Ti-substituted hydroxyapatite: comparison with anatase-TiO_2, *J. Mol. Catal. A Chem.*, **338** (2011) 18−23.

[19] K. Pruethiarenun, T. Isobe, S. Matsushita, J. Ye, A. Nakajima, Comparative study of photoinduced wettability conversion between $[PW_{12}O_{40}]^{3-}$/brookite and $[SiW_{12}O_{40}]^{4-}$/brookite hybrid films, *Mater. Chem. Phys*., **144** (2014) 327−334.

[20] P. R. Harvey, R. Rudham, S. Ward, Photocatalytic oxidation of liquid propan-2-ol by titanium dioxide, *J. Chem. Soc. Faraday Trans*., **79** (1983) 1381−1390.

[21] Y. Ohko, K. Hashimoto, A. Fujishima, Kinetics of photocatalytic reactions under extremely low-intensity UV illumination on titanium dioxide thin films, *J. Phys. Chem. A*, **101** (1997) 8057−8062.

[22] A. Mylonas, A. Hiskia, E. Androulaki, D. Dimotikali, E. Papaconstantinou, New aspect of the mechanism of photocatalytic oxidation of organic compounds by polyoxometalates in aqueous solutions. The selective photooxidation of propan-2-ol to propanone: the role of OH radicals, *Phys. Chem. Chem. Phys*., **1** (1999) 437−440.

[23] S. A. Larson, J. A. Widegren, J. L. Falconer, Transient studies of 2-propanol photocatalytic oxidation on titania, *J. Catal.,* **157** (1995) 611−625.

[24] A. Fujishima, T. N. Rao, D.A.Tryk, Titanium dioxide photocatalysis, *J. Photochem. Photobiol. C.*, **1** (2000) 1−21.

[25] W. Li, G. D. Meitzner, R. W. Borry III, E. Iglesia, Raman and X-ray absorption studies

of Mo species in Mo/H-ZSM5 catalysts for non-oxidative CH_4 reactions, *J. Catal*., **191** (2000) 373−383.

[26] M. Chen, U. V. Waghmare, C. M. Friend, E. Kaxiras, A density functional study of clean and hydrogen-covered α-MoO_3 (010): Electronic structure and surface relaxation, *J. Chem. Phys*., **109** (1998) 6854−6860.

[27] M. Oshikiri, J. H. Ye, M. Boero, Inhomogeneous RVO_4 photocatalyst systems (R = Y, Ce, Pr, Nd, Sm, Eu, Gd, Tb, Dy, Ho, Er, Tm, Yb, Lu), *J. Phys. Chem. C*, **118** (2014) 8331−8341.

[28] H. Monma, S. Ueno, T. Kanazawa, Properties of hydroxyapatite prepared by the hydrolysis of tricalcium phosphate, *J. Chem. Tech. Biotechnol*., **31** (1981) 15−24.

[29] I. Nakamura, N. Neigishi, S. Kutsuna, T. Ihara, S. Sugihara, K. Takeuchi, Role of oxygen vacancy in the plasma-treated TiO_2 photocatalyst with visible light activity for NO removal, *J. Mol. Catal. A Chem.*, **161** (2000) 205−212.

[30] P. H. Kasai, Electron spin resonance studies of γ- and X-ray-irradiated zeolites, *J. Chem. Phys*., **43** (1965) 3322−3327.

[31] J. H. Lunsford, ESR of adsorbed oxygen species, *Catal. Rev*., **8** (1973) 135−157.

[32] Y. Nakaoka, Y. Nosaka, ESR Investigation into the effects of heat treatment and crystal structure on radicals produced over irradiated TiO_2 powder, *J. Photoch. Photobio. A*, **110** (1997) 299−305.

[33] J. M. Coronado, A. J. Maira, J.C. Conesa, K. L. Yeung, V. Augugliaro, J. Soria, EPR study of the surface characteristics of nanostructured TiO_2 under UV irradiation, *Langmuir*, **17** (2001) 5368−5374.

[34] K. C. Khulbe, R. S. Mann, M. Ternan, Electron spin resonance studies of the surface chemistry of molybdenum-alumina catalysts, *Can. J. Chem.*, **56** (1978) 1769−1772.

[35] J. Liqiang, Y. Fulong, H. Haige, X. Baifu, C. Weimin, F. Honggang, Relationships of surface oxygen vacancies with photoluminescence and photocatalytic performance of ZnO nanoparticles, *Sci. Chin. B*, **48** (2005) 25−30.

[36] D. Aronov, A. Karlov, G. Rosenman, Hydroxyapatite nanoceramics: Basic physical properties and biointerface modification*, J. Euro. Cer. Soc.*, **27** (2007) 4181−4186.

[37] Lange's Handbook of Chemistry 12th edition, Ed. J. A. Dean, McGrow-Hill Inc., New York (1976) pp6−12.

[38] Kagaku Binnran Third edition, Ed. The Chemical Society of Japan, Maruzen, Tokyo Japan, ppII--475 (1988) [in Japanese].

[39] I. V. Kozhevnikov, Catalysis by heteropoly acids and multicomponent polyoxometalates in liquid-phase reactions, *Chem. Rev.*, **98** (1998) 171−198.

[40] Y. Nosaka, S. Takahashi, H. Sakamoto, A. Y. Nosaka, Reaction mechanism of Cu(II)-grafted visible-light responsive TiO_2 and WO_3 photocatalysts studied by using ESR spectroscopy and chemiluminescence photometry, *J. Phys. Chem. C*, **115** (2011) 21283−21290.

[41] C. Zollfrank, K. Gutbrod, P. Wechsler, J. P. Guggenbichler, Antimicrobial activity of transition metal acid MoO_3 prevents microbial growth on material surfaces, *Mater. Sci. Eng. C*, **32** (2012) 47–54.

[42] M. Mizutani, K. Sunada, T. Isobe, S. Matsushita, A. Nakajima, Anti-bacterial and photocatalytic activities of $(Mo_{0.5}, W_{0.5})O_3$ with $Cu(Mo_{0.5}, W_{0.5})O_4$ prepared by impregnation method and mechanochemical processing, *J. Jpn. Soc. Colour Mater.,* **91** (2018) 89−93.

[43] K. Krishnamoorthy, M. Premanathan, M. Veerapandian, S. J. Kim, Nanostructured molybdenum oxide-based antibacterial paint: effective growth inhibition of various

pathogenic bacteria, *Nanotechnology*, **25** (2014) 315101(10pp).

[44] C. C. Mardare, A. W. Hassel, Investigations on bactericidal properties of molybdenum-tungsten oxides combinatorial thin film material libraries, *ACS Comb. Sci.,* **16** (2014) 631−639.

Table 3.1 The detailed refinement parameters and atomic positions.

		Ti-HAp	TH-A3
$a = b$ (Å)		9.4186	9.4196
c (Å)		6.8834	6.8811
Ca(I)	x	0.3333	0.3333
	y	0.6667	0.6667
	z	0.0067	0.0066
	B (Å^2)	0.666	0.666
Ca(II)	x	0.2431	0.2449
	y	0.9951	0.9949
	z	0.2500	0.2500
	B (Å^2)	0.328	0.328
P	x	0.3940	0.3959
	y	0.3672	0.3681
	z	0.2500	0.2500
	B (Å^2)	0.192	0.192
O(I)	x	0.3282	0.3289
	y	0.4845	0.4848
	z	0.2500	0.2500
	B (Å^2)	0.295	0.295
O(II)	x	0.5907	0.5905
	y	0.4652	0.4655
	z	0.2500	0.2500
	B (Å^2)	0.496	0.496
O(III)	x	0.3409	0.3421
	y	0.2572	0.2581
	z	0.0714	0.0703
	B (Å^2)	0.632	0.632
O(H)	x	0	0
	y	0	0
	z	0.1968	0.1950
	B (Å^2)	0.875	0.875
H	x	0	0
	y	0	0
	z	0.0572	0.0555
	B (Å^2)	1.750	1.750
R_{wp} (%)		2.80	2.79

Table 3.2 Chemical compositions obtained from ICP analysis and the CO_2 generation rate.

Sample name	Mo/Ti [mol%]	K_{CO2} [ppm/h]
Ti-HAp	-	14
TH-A1	0.16	44
TH-A2	0.33	82
TH-A3	1.21	112
TH-A4	1.10	121
TH-A5	0.91	121
TH-A6	0.64	123
TH-A7	0.50	131
TH-A8	0.46	121

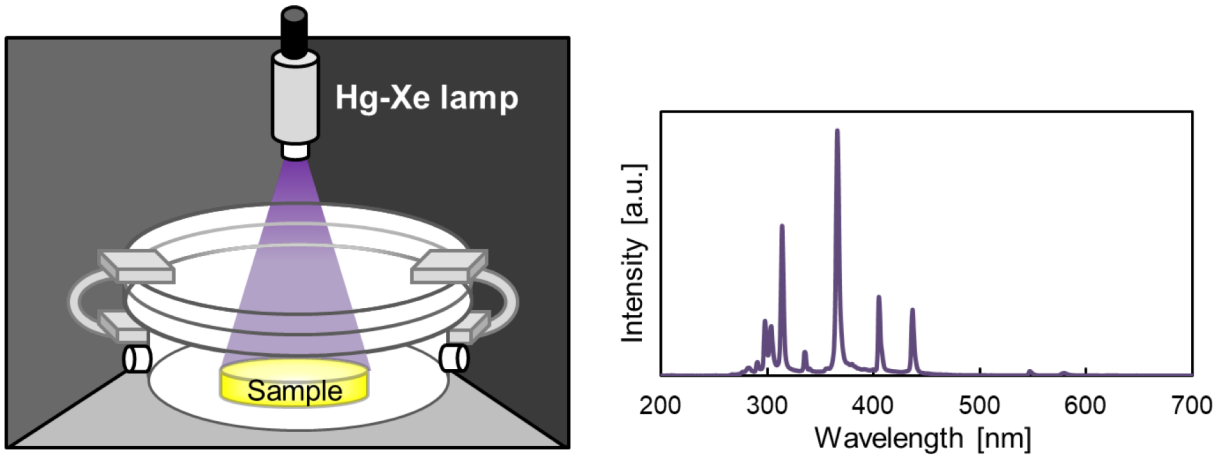

Figure 3.1 Schematic illustration of photocatalytic activity measurement and Hg-Xe lamp spectra

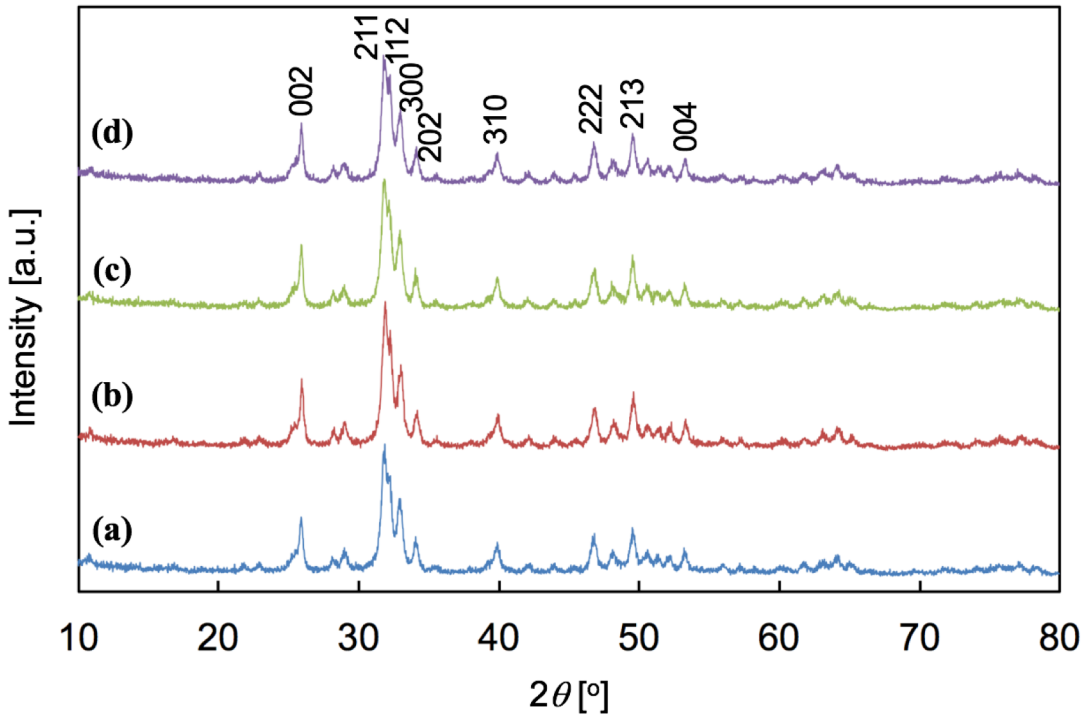

Figure 3.2 XRD patterns of sample powders: (a) Ti-HAp, (b) TH-A1, (c) TH-A3, and (d) TH-A5.

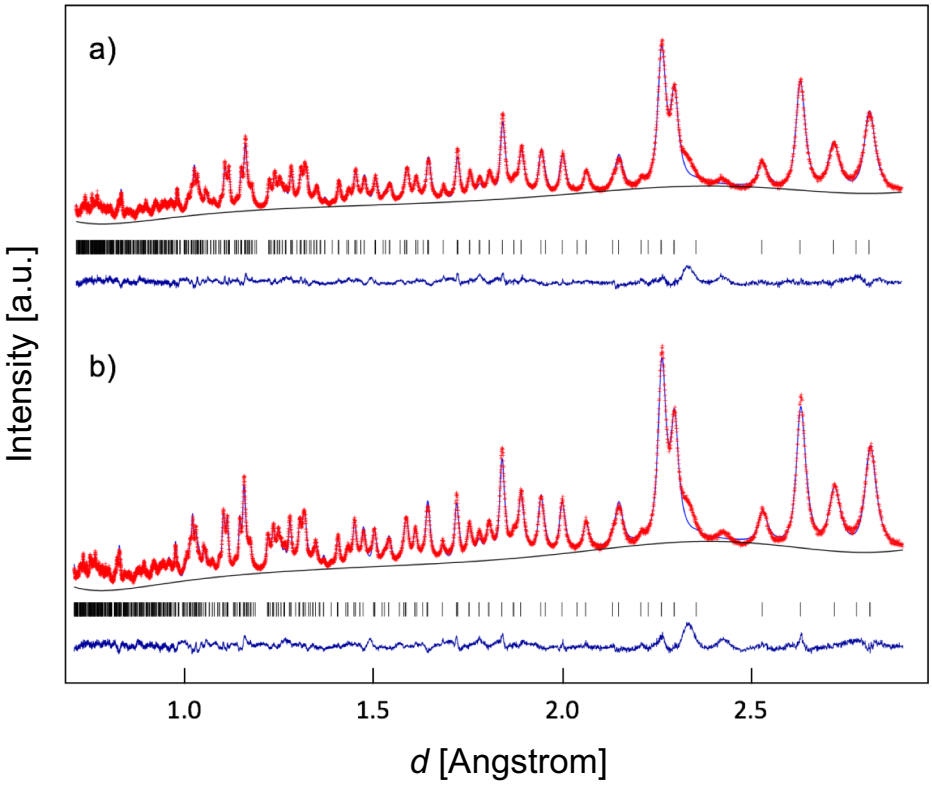

Figure 3.3 Rietveld refinement patterns form neutron diffraction of (a) Ti-HAp and (b) TH-A3 measure at the scattering angle of 155°. Red marks: measured intensity, blue line: calculated intensity. Different (measured-calculated) curve appear at the bottom of the plot.

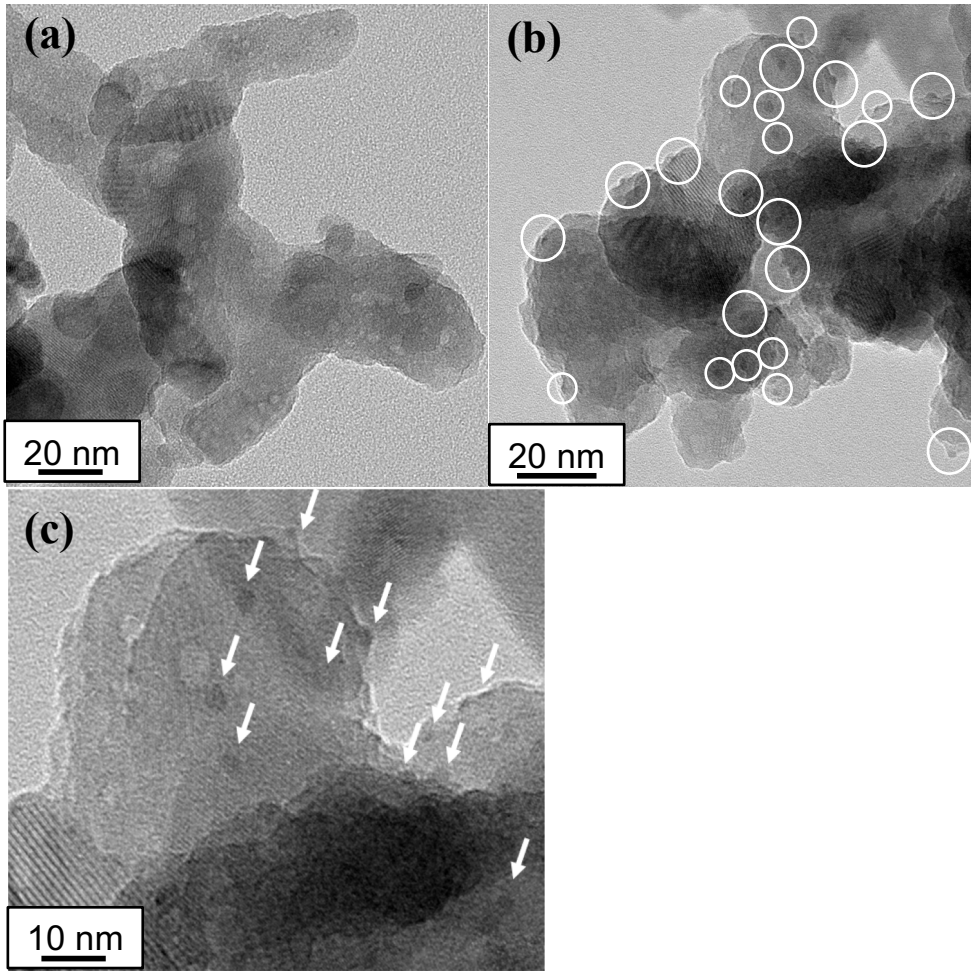

Figure 3.4 TEM micrographs of Ti-HAp particles: (a) before Mo modification, and (b, c) after Mo modification (sample: TH-A3).

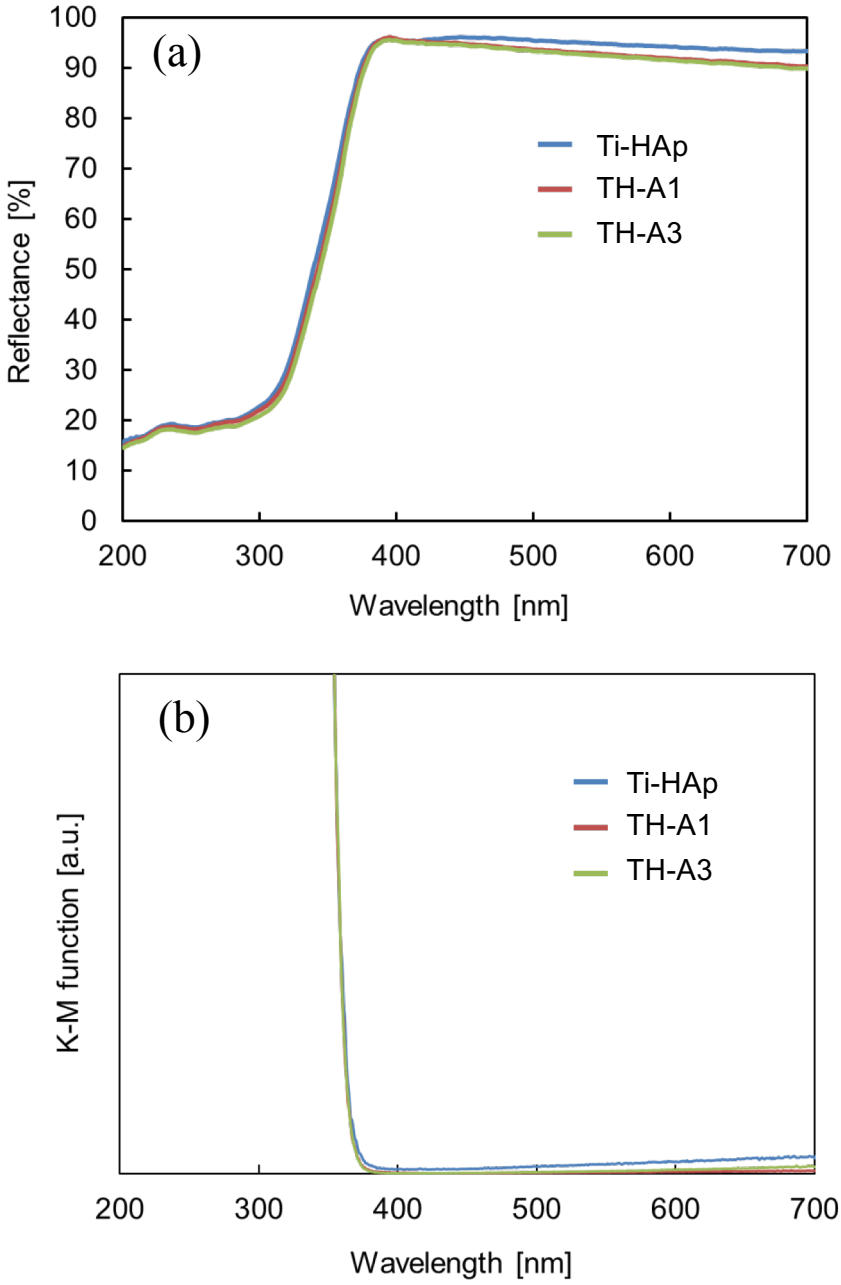

Figure 3.5 UV-vis spectra (a) and Kubelka-Munk function plots (b) of Ti-HAp, TH-A1, and TH-A3.

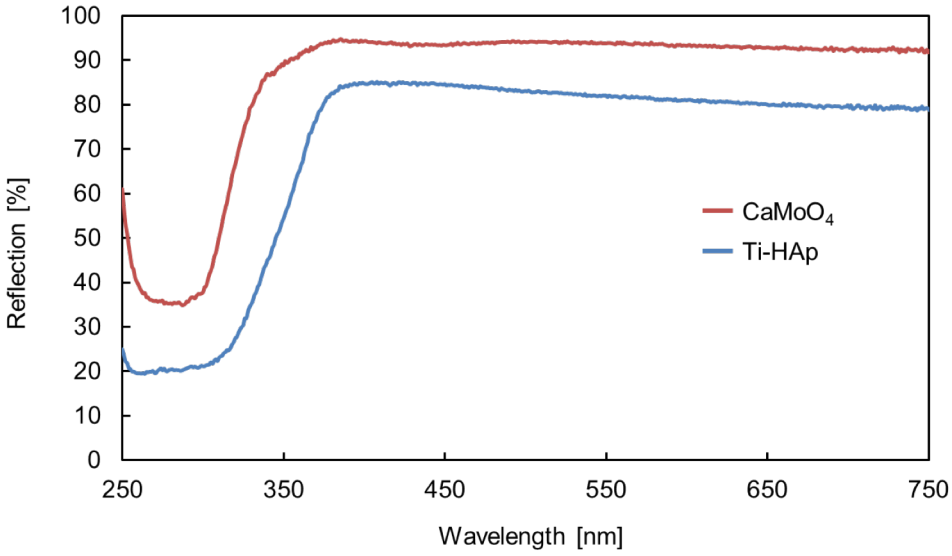

Figure 3.6 UV-vis spectra of $CaMoO_4$ and Ti-HAp.

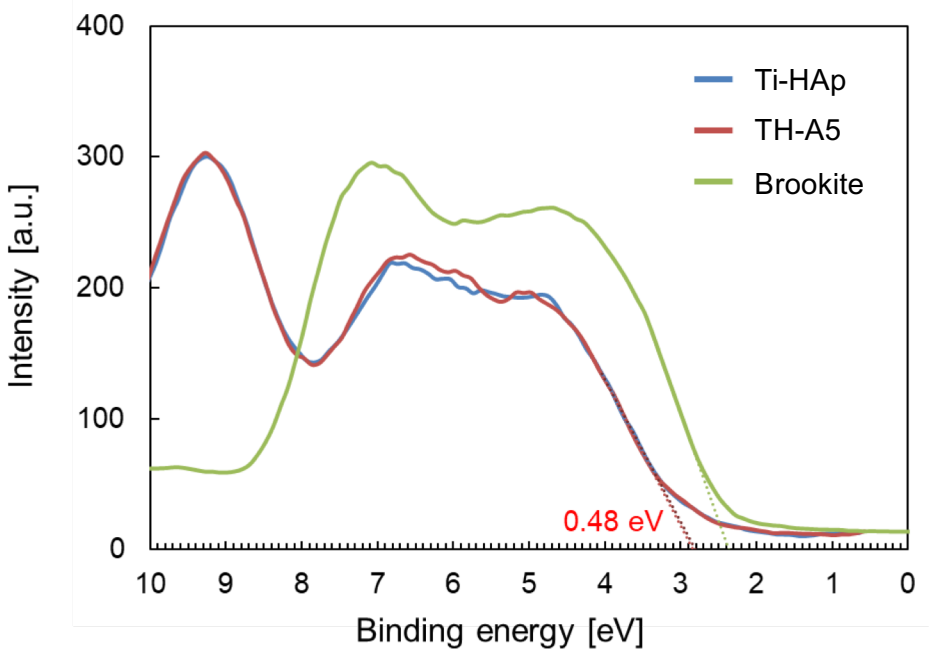

Figure 3.7 XPS spectra of the binding energy of O 2p of the powders.

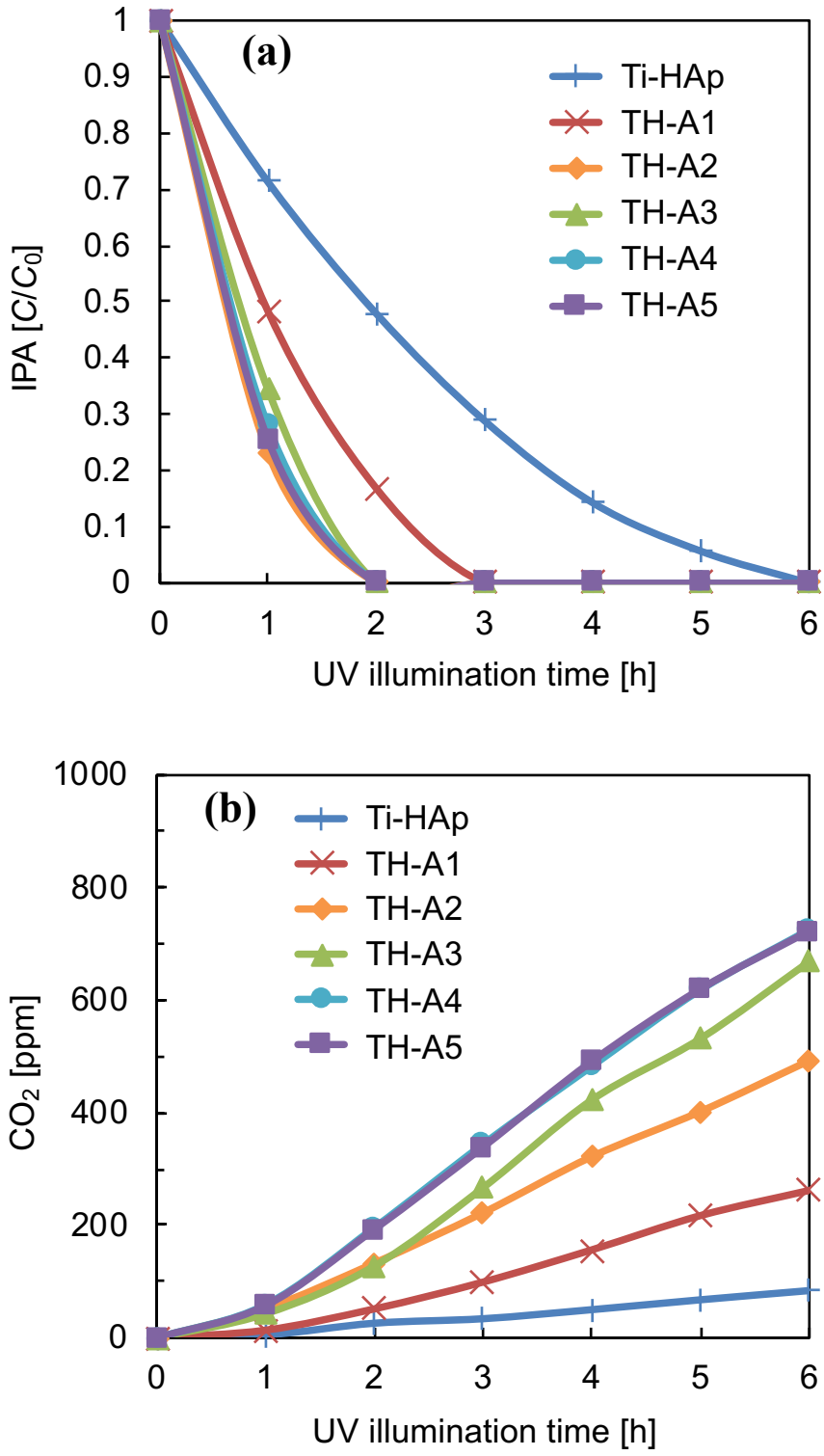

Figure 3.8 Concentration changes of (a) gaseous IPA and (b) CO_2 against UV illumination time.

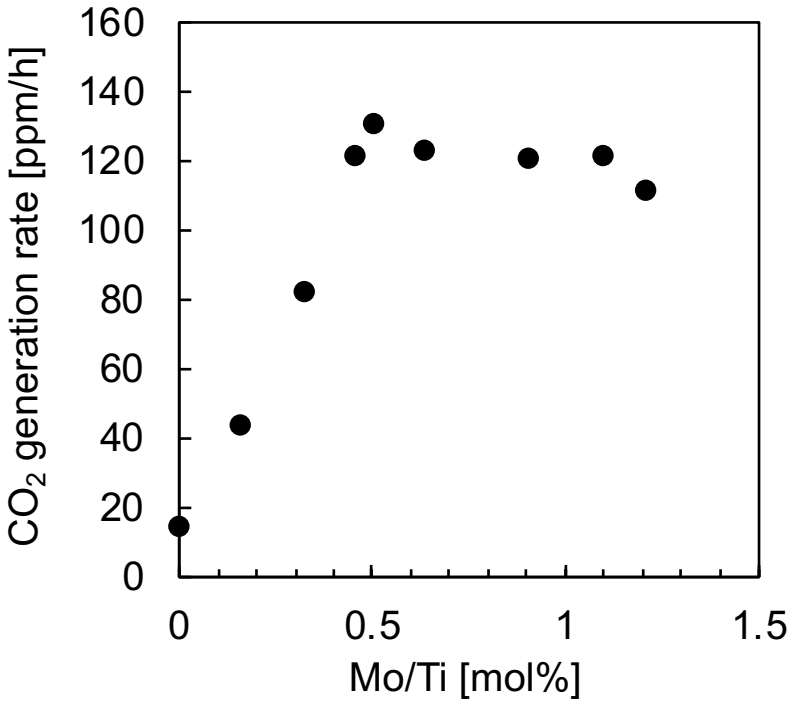

Figure 3.9 Relation between the Mo concentrations and the CO_2 generation rate of all samples.

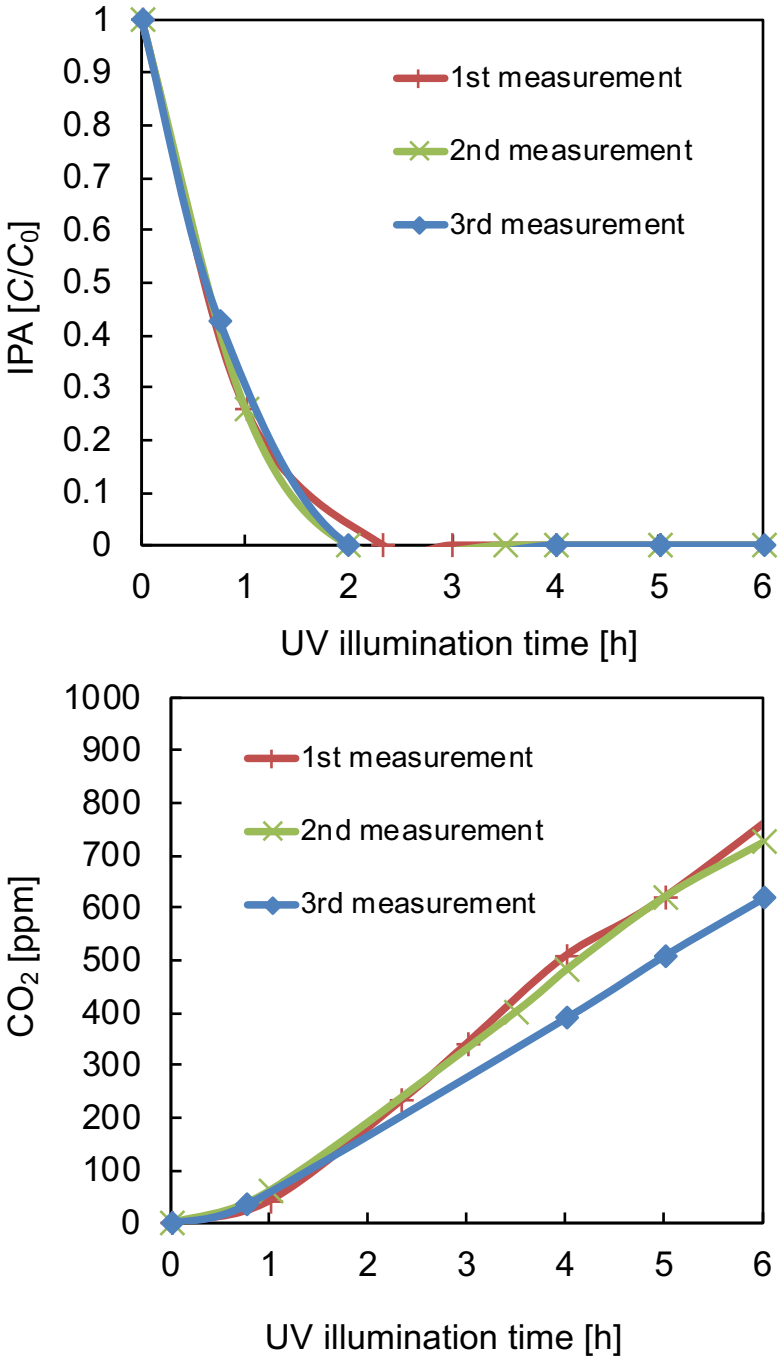

Figure 3.10 Concentration changes of (a) gaseous IPA and (b) CO_2 against UV illumination time of TH-A3 by repeated measurement.

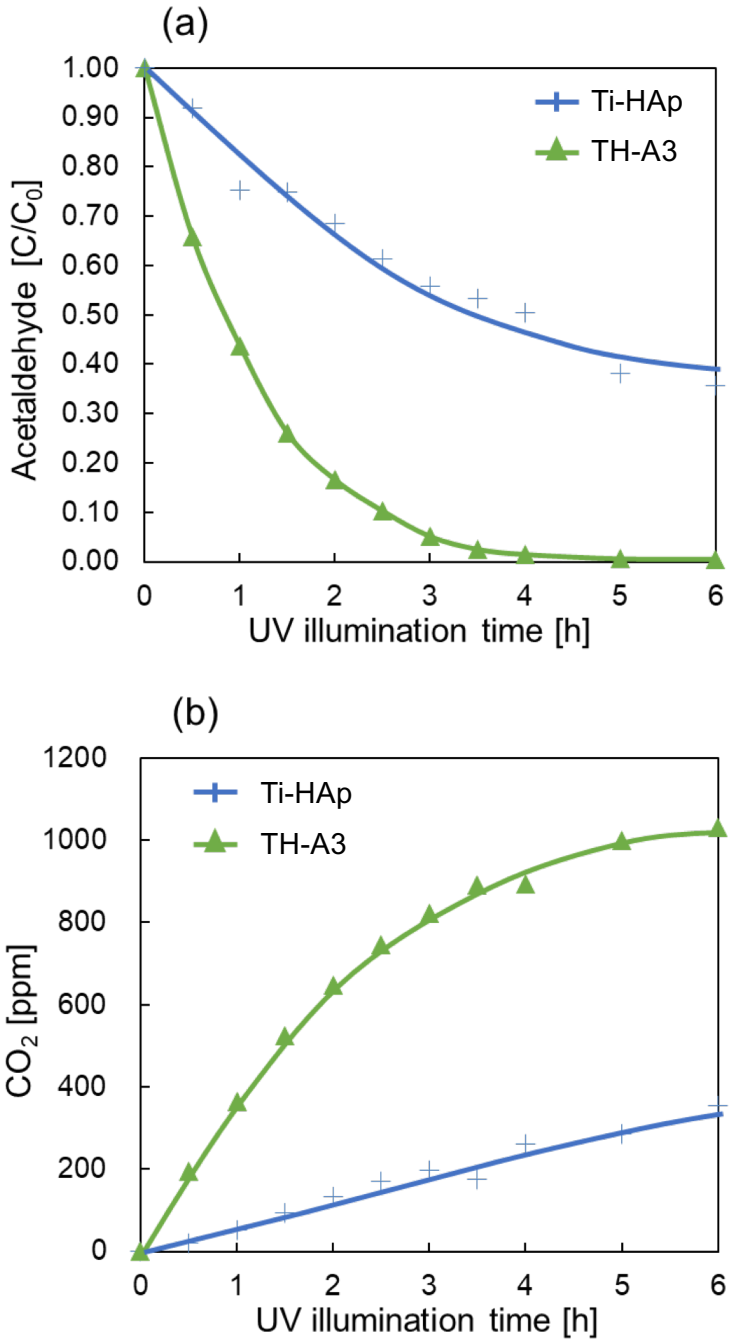

Figure 3.11 Concentration changes of (a) gaseous acetaldehyde and (b) CO_2 against UV illumination time of Ti-HAp and TH-A3.

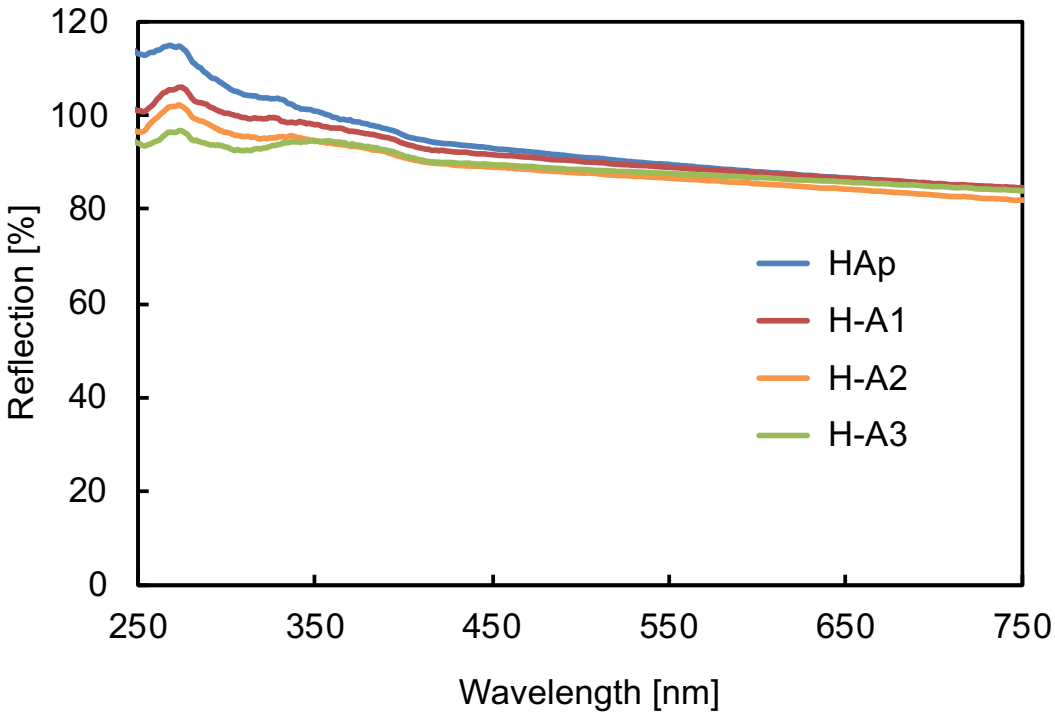

Figure 3.12 UV-vis spectra of Mo-modified HAps.

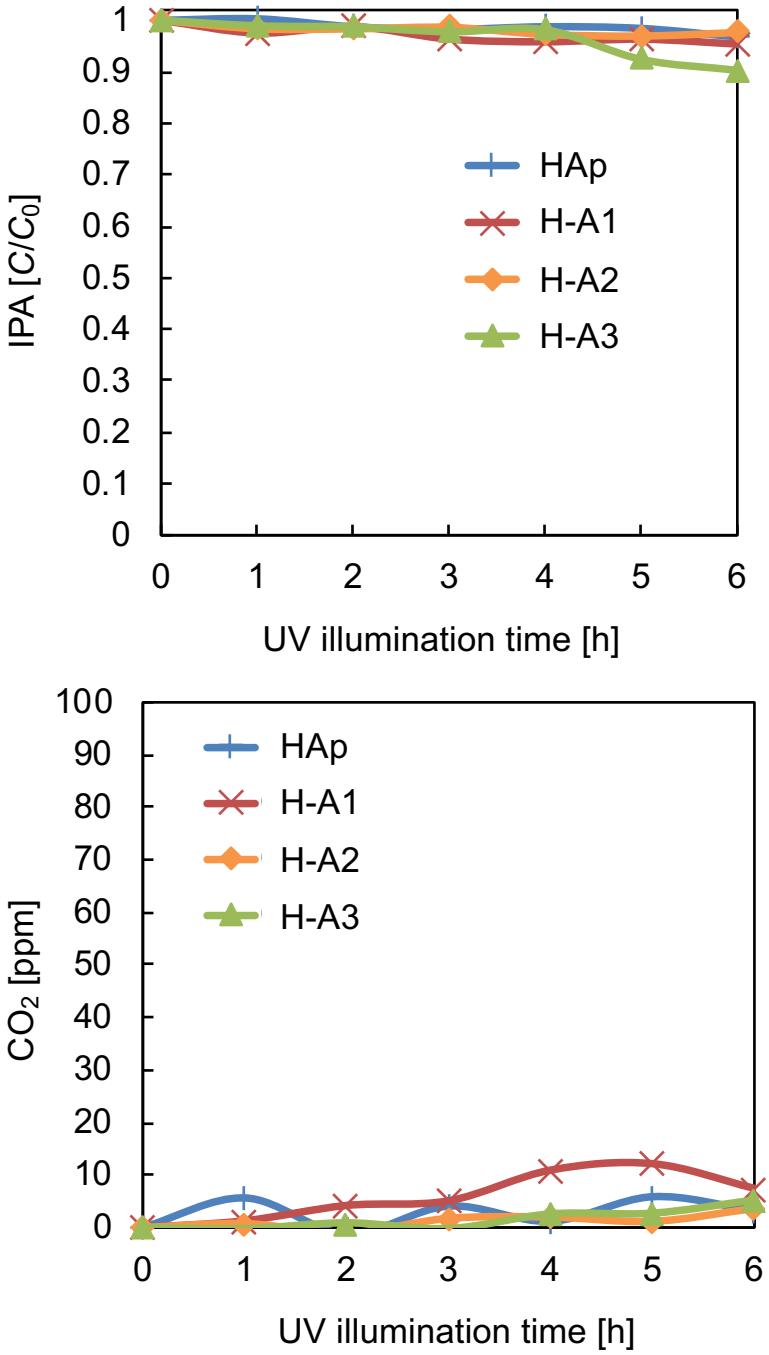

Figure 3.13 Concentration changes of (a) gaseous IPA and (b) CO_2 against UV illumination time for Mo-modified HAp.

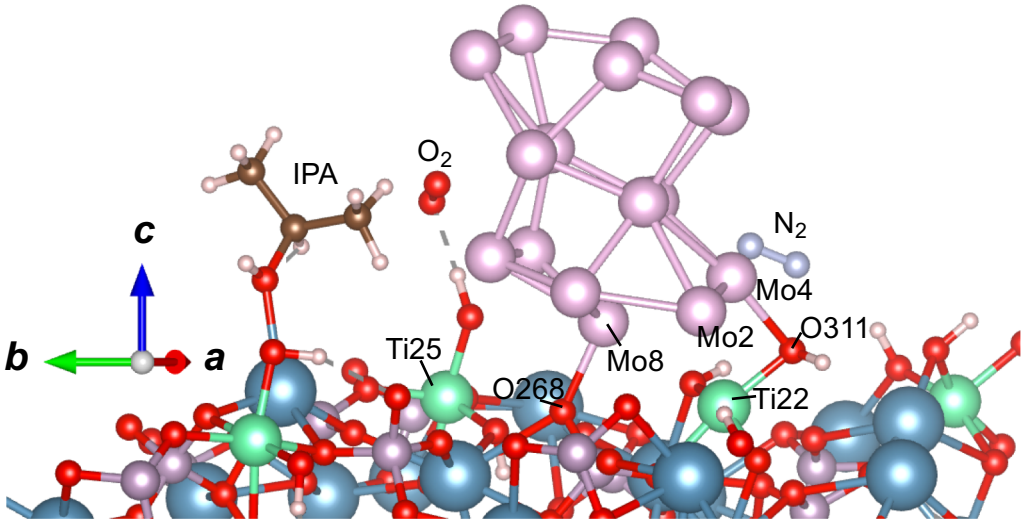

Figure 3.14 Atomic configuration of the Ti-HAp surface with a Mo metallic cluster and IPA adsorbed onto the surface, and O_2 and N_2 molecule near the surface. The color code is red for O, white for H, pink for Mo, green for Ti, purple for P, blue for Ca, gray for N, and brown for C. The model was illustrate by VESTA.

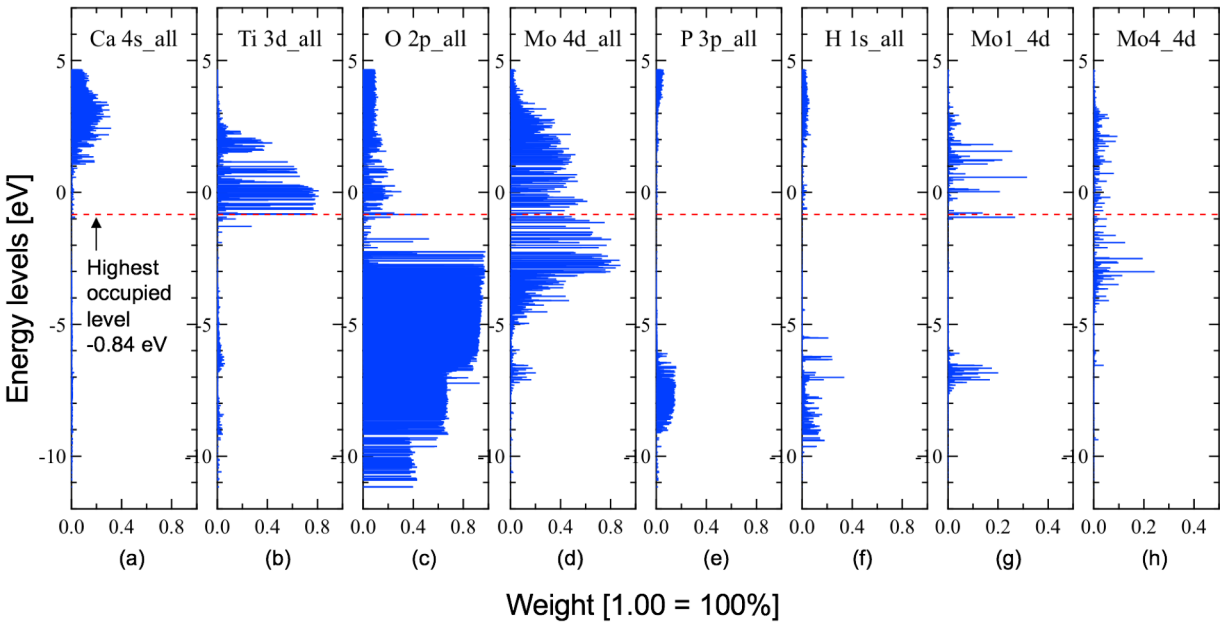

Figure 3.15 Electronic structure obtained by projection onto atomic orbitals of the Mo-modified Ti-HAp at 300 K.

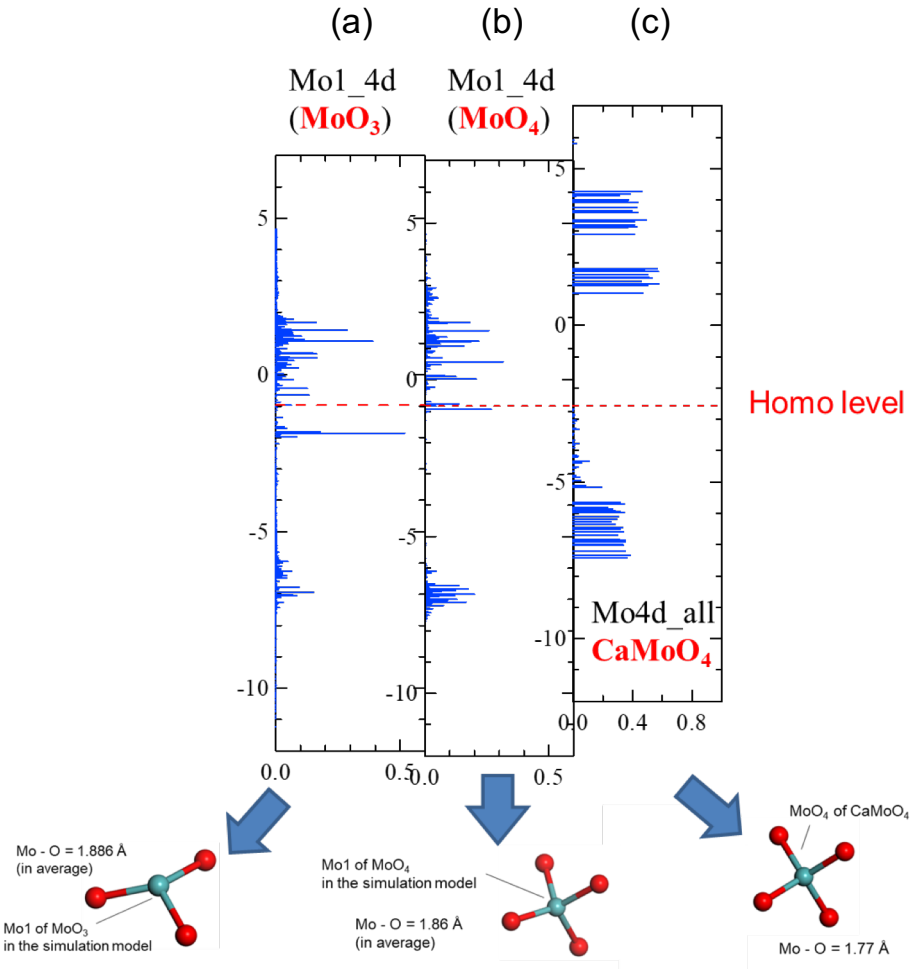

Figure 3.16 (a) and (b) present electronic structure of Mo species obtained by projection onto atomic orbitals of the Mo-modified Ti-HAp. The right structure (c) is on bulk $CaMoO_4$ crystal [*].

[*] Electronic structure was computed by the same procedure as the manuscript at G point using 2 x 2 x 1 super cell of $CaMoO_4$ ($Ca_{16}Mo_{16}O_{64}$) based on the structure reported in the following literature:

Lee, Sang-Gil; Kim, Youn-Joong; Yoo, Seung Jo; Lee, Seok-Hoon; Kim, Jin-Gyu, Journal of Analytical Science and Technology (2012) 3, (1) p128-p134 (ICSD Collection Code 417513).

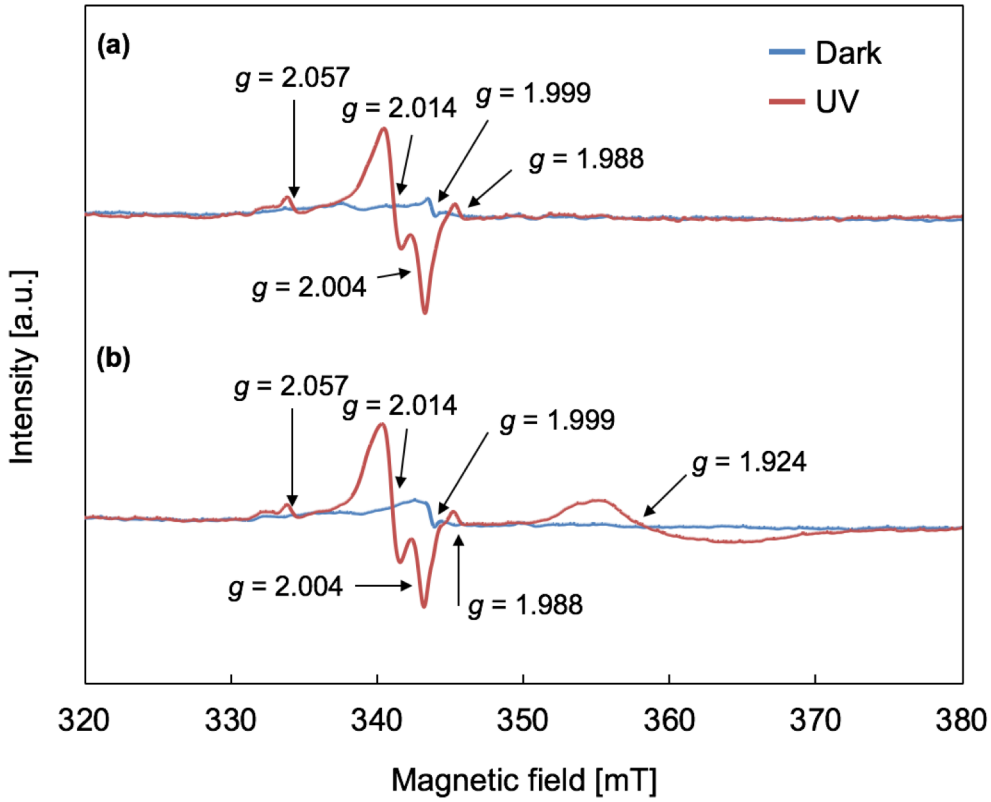

Figure 3.17 ESR spectra of (a) Ti-HAp and (b) TH-A3, showing the effects of UV illumination.

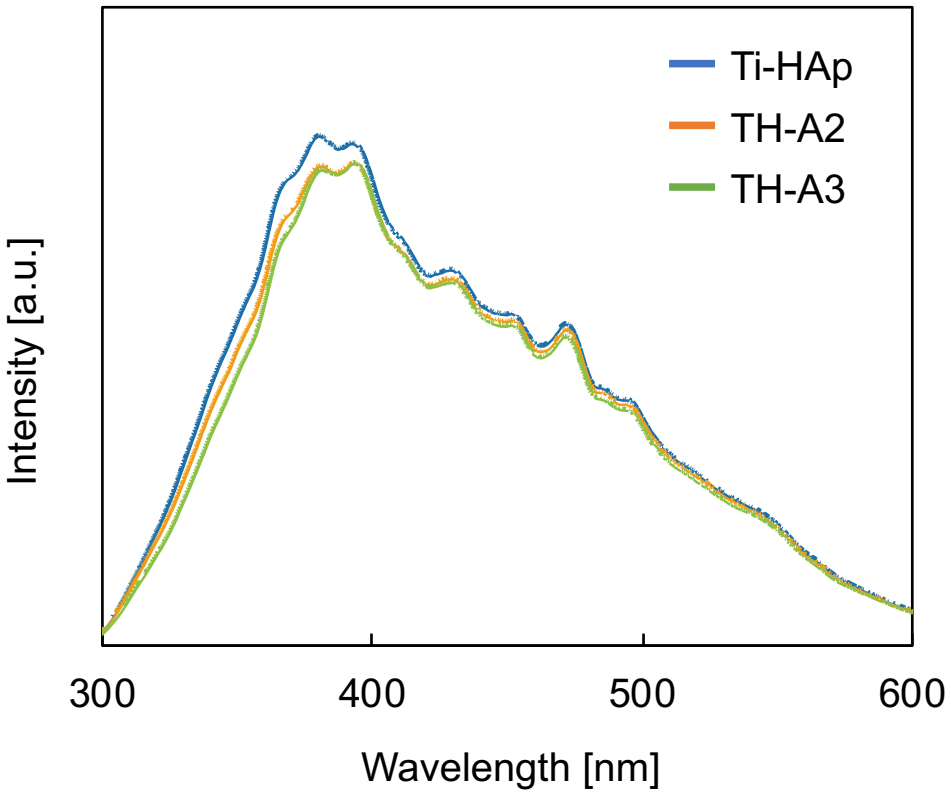

Figure 3.18 PL emission spectra of Ti-HAp, TH-A2, and TH-A3 with excitation wavelength of 280 nm.

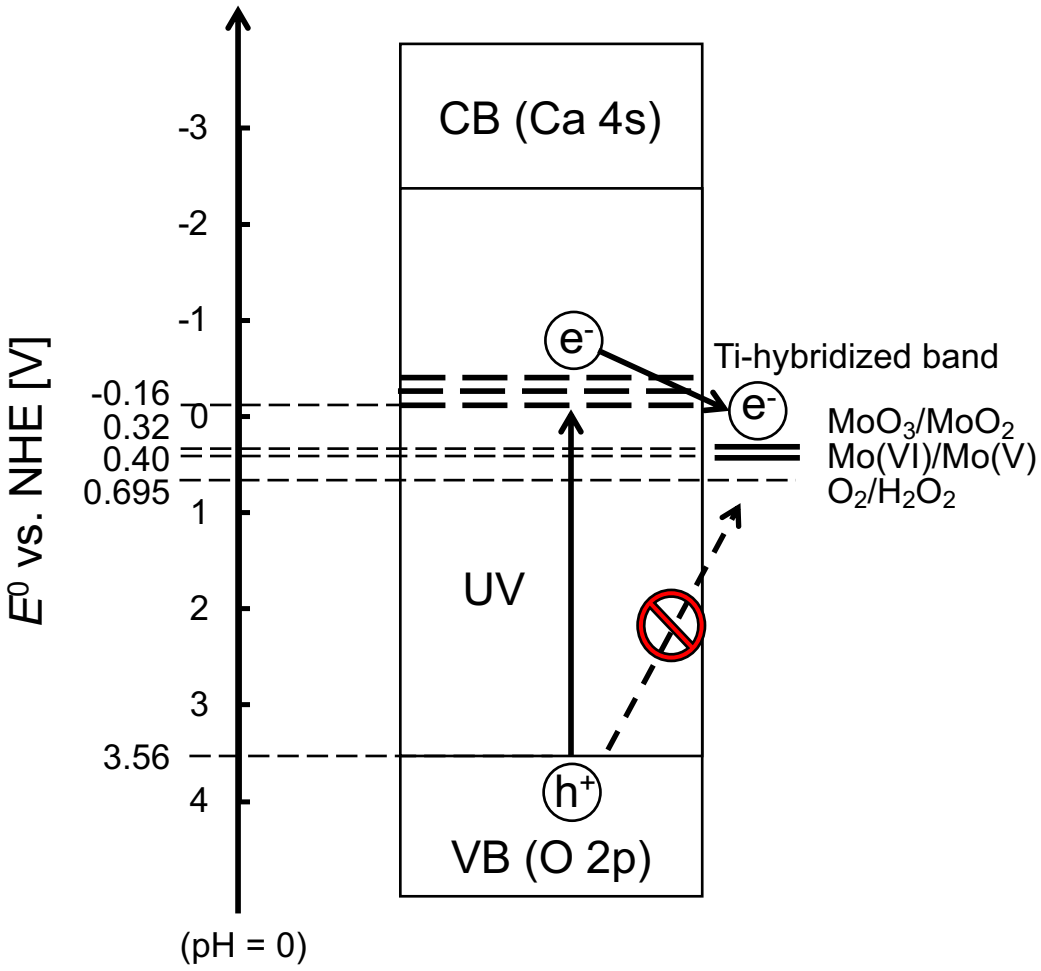

Figure 3.19 Feasible charge transfer process under UV illumination of Mo-modified Ti-HAp.

CHAPTER 4

Modification of Ti-HAp surface with an ethanol solution of molybdenyl acetylacetonate using chemisorption calcination cycle (CCC) technique

4.1. Introduction

In **Chapter 3**, we conducted Mo modification on the Ti-HAp surface by impregnation method using aqueous solution of $CaMoO_4$. The obtained powder was modified with Mo-based clusters. The photocatalytic decomposition activity of the materials against gaseous 2-propanol (IPA) was increased about nine times [1]. Results of density functional theory (DFT) calculations suggest that the modified Mo state is small clusters of MoO_x. However, evidence of the contribution of MoO_x remains insufficient because of the influence of Ca ions from $CaMoO_4$ aqueous solution. Based on the starting materials and preparation procedures, the clusters are expected to be either MoO_x or $CaMoO_4$. Moreover, the modifiable Mo amount was limited because of the low solubility of $CaMoO_4$ or dissolution of MoO_3 in water. Therefore, the maximum activity of MoO_x-modified Ti-HAp remains unclear. Preparation of the MoO_x-modified Ti-HAp by direct modification of MoO_x with control of the surface modification amount is necessary to investigate the potential of this material for wider use.

In **Chapter 2**, we have conducted the chemisorption calcination cycle (CCC) technique, proposed by Tada *et al*., by which chemical bonds adsorb metal complexes. Also by CCC, the organic (ligand) part is oxidized by post-heating to prepared metal oxide clusters or ultrathin films at a molecular scale [2–5]. For this chapter, we prepared MoO_x-modified Ti-HAp using CCC technique for comparison with **Chapter 3** that used an impregnation method with an aqueous solution of $CaMoO_4$ [1]. For CCC technique, a non-aqueous solvent (ethanol) was

used. We were therefore able to avoid both ion exchange of Ca sites in Ti-HAp and the dissolution of MoO_x into water. Subsequently, we examined the photocatalytic activity under UV illumination and discussed the role of Mo modification in photocatalytic activity. We also prepared MoO_x-modified HAp (not Ti-HAp) for comparison.

4.2. Experimental procedure

4.2.1. Sample preparation and characterization

For CCC technique, commercial Ti-HAp (Hautoform TA; Fuji Chemical Ind. Co. Ltd., Osaka, Japan) was used as a starting material. Reagent grade molybdenyl acetylacetonate ($MoO_2(C_5H_8O_2)_2$, $MoO_2(acac)_2$; Fujifilm Wako Pure Chemical Corp., Osaka, Japan) was dissolved into ethanol (10 mL) to produce various concentrations Z: 0.08 mM, 0.8 mM, 4 mM, and 8 mM. After Ti-HAp powder (1 g) was added to the $MoO_2(acac)_2$ ethanol solution, it was mixed and let to stand for 24 h at room temperature. The obtained samples were washed repeatedly using ethanol and were dried at 60°C for 24 h in air with subsequent heating at 500°C for 1 h in ambient air. These procedures repeated several times (Y) to control the chemical composition of the surface. We also prepared samples for comparison using HAp (Taihei Chemical Industrial Co. Ltd., Osaka, Japan) instead of Ti-HAp under the same conditions. Before the preparation, HAp powder was heated at 650°C for 1 h in ambient air (same temperature as commercial Ti-HAp before modification). To simplify the sample name of MoO_x-modified samples using CCC technique, it will be designated as X-EY-Z, with X representing the base material (either TH for Ti-HAp or H for HAp), E standing for the solvent (ethanol (E) solution for CCC technique), Y signifying the repetitions (1, 2, or 3), and Z denoting the $MoO_2(acac)_2$ solution concentration: 0.08 mM, 0.8 mM, 4 mM, or 8 mM).

For impregnation method using aqueous solution of $CaMoO_4$, HAp powder was firing at

650°C for 1 h in ambient air before the preparation. Reagent grade calcium molybdate ($CaMoO_4$; Fujifilm Wako Pure Chemical Corp., Osaka, Japan) was dissolved into distilled water (200 mL, 0.1 mM) at 80°C. Then the solution was allowed to stand at room temperature until cool. Then HAp powder (1 g) was added to the solution and stirred for 5 min at room temperature. After the powder was filtered and washed several times with distilled water, it was dried at 60°C for 24 h in air, followed by heating at 500°C for 1 h in ambient air. These procedures were repeated several times (Y) to adjust the Mo concentration on the surface. Regarding Ti-HAp samples, we prepared the samples as described in **Chapter 3** [1]. To simplify the sample names of MoO_x-modified samples by impregnation method using aqueous solution of $CaMoO_4$, they will be designated as X-AY, with X representing the base material (either TH for Ti-HAp or H for HAp), A denoting the solvent (aqueous (A) solution in this method), and Y representing the repetitions.

The crystalline phases of the obtained samples were evaluated using X-ray diffraction (XRD; XRD-6100; Shimadzu Corp., Japan) with Cu Kα radiation. Specific surface areas were measured using Brunauer, Emmett, and Teller (BET) method with N_2 adsorption (BEL SORP mini; Bel Japan Inc., Japan). Using a UV-vis scanning spectrophotometer (V-650; Jasco Corp., Tokyo, Japan), the optical absorption spectra were evaluated. We observed the powder morphology using a transmission electron microscope (TEM, JEM-2010F; JEOL Ltd., Tokyo, Japan). The chemical compositions of the obtained samples were evaluated using inductively coupled plasma analysis (Prodigy ICP; Teledyne-Leeman Labs, Inc., Hudson, NH, U.S.A.). Additionally, the surface chemical compositions of the elements were measured using X-ray photoelectron spectroscopy (XPS, ESCA 5500MT; PerkinElmer Inc., U.S.A.) with an Al Kα X-ray line (1486.6 eV).

4.2.2. Photocatalytic activity, electron spin resonance, and photoluminescence measurements

Photocatalytic activity was evaluated according to the decomposition of gaseous 2-propanol (IPA) as follows. The sample powder (40 mg) was dispersed homogeneously into a petri dish with area of 8.35 cm^2. After dispersion, the sample dish was kept under UV illumination (ca. 0.7 mW/cm^2 at 355 nm) to remove organic compounds that might had been adsorbed onto the surface. Then the sample dish was placed at the center of a Pyrex glass (500 mL in volume). Subsequently, the vessel was sealed with a quartz lid and was filled with air (20°C, 80% relative humidity). Then gaseous IPA (700 ppm) was injected into the vessel. It was stored in the dark for one night to achieve the adsorption equilibrium between the powder and gaseous IPA. Then UV illumination was applied using a UV illuminator (LA-410UV-1; Hayashi Watch Works, Tokyo, Japan) equipped with a Hg-Xe lamp through a liquid light guide without a filter. The UV illumination intensity was adjusted to 1 mW/cm^2 at 355 nm. The IPA and CO_2 concentrations were measured every 1 h using gas chromatography (GC-2014 with a flame ionization detector (FID), methanizer, and column (Sunpak-A; Shimadzu Corp.); Shimadzu Corp., Tokyo, Japan). A schematic illustration of photocatalytic activity measurements and the spectra of the UV illumination are presented in **Fig. 3.1** in **Chapter 3**.

The electron spin resonance (ESR) spectra were evaluated at 90–100 K using an ESR spectrometer (EMXnano; Bruker Analytik, Germany). The sample powder was placed in a quartz glass sample tube with a Young vacuum joint and a stopcock, followed by evacuation of air from the sample tube. The measurements were taken in the dark and under UV illumination using a UV illuminator (LA-410UV-1; Hayashi Watch Works, Tokyo, Japan) equipped with a 200 W Hg-Xe lamp. The microwave frequency was approximately 9.62 GHz.

The microwave powder was fixed at 1 mW. The field modulation was 0.05 mT. The number of scan was 30 times. The photoluminescence (PL) emission spectra were measured using a fluorescence spectrophotometer (F-7100; Hitachi Ltd., Tokyo, Japan). The PL measurements were taken with 280 nm excitation wavelength using a 150 W Xe lamp with 5.0-nm-wide excitation slits, 1200 nm/min scanning speed, and 700 V PMT voltage.

4.3. Results and discussion

4.3.1. Characteristics of obtained samples

Figure 4.1 shows XRD patterns of Ti-HAp and HAp obtained before and after Mo modification by CCC technique. No marked difference in intensity was found among the peaks for all samples. The XRD patterns showed only the peaks attributable to a HAp structure with $P6_3/m$ (No. 176) space group. This result was similar to that obtained for MoO_x-modified Ti-HAp samples prepared by impregnation method using an aqueous solution of $CaMoO_4$ in **Chapter 3** [1]. The specific surface areas of all samples were almost equivalent (35–39 m^2/g for MoO_x-modified Ti-HAp samples, and 27–32 m^2/g for MoO_x-modified HAp samples), except for the samples prepared using $MoO_2(acac)_2$ ethanol solution with concentration of 8 mM, which provided lower specific surface area (33 m^2/g for TH-E2-8mM, 28 m^2/g for TH-E3-8mM, and 25 m^2/g for H-E2-8mM) as listed in **Table 4.1** and **Table 4.2**.

Figure 4.2 presents TEM images of Ti-HAp before and after three cycles of Mo modifications by CCC technique using $MoO_2(acac)_2$ ethanol solution with 8 mM concentration (TH-E3-8mM). Rod-like morphology with 50–80 nm average particle length was observed for both samples. In **Chapter 3**, a cluster-like area (1–2 nm) was identified on the surface of MoO_x-modified Ti-HAp (TH-A3) prepared through impregnation method using aqueous solution of $CaMoO_4$ [1]. In this work, extremely small MoO_x clusters of less than 1

nm size were formed onto Ti-HAp prepared using CCC technique (represented by circles in **Fig. 4.2(c)**), suggesting suppression of the growth of MoO_x clusters during post-heating, probably because of strong chemisorption of $MoO_2(acac)_2$ onto the Ti-HAp surface [3]. Because of insufficient durability against damage by the focused electron beam and the extremely small cluster size, analysis of the chemical compositions of these parts using EDS was not feasible.

Figure 4.3(a) portrays UV-vis spectra of Ti-HAp before and after Mo modification. All samples showed only the absorption band of Ti-HAp. From the Kubelka–Munk function, the bandgaps of all samples were 3.72 eV, which was calculated by assuming direct transition. These values were approximately equal to the values reported for Ti-HAp [1, 6, 7]. **Figure 4.3(b)** presents UV-vis spectra of HAp before and after Mo modification. The bandgap of HAp was greater than 6 eV, which is approximately equal to the reported value of HAp [6]. This bandgap indicates that HAp has no absorption in this measurement condition. The new absorption band was observed in the UV range (ca. 250–350 nm) after Mo modification. The light absorption of MoO_x-modified HAps increased increasing Mo modification cycle or concentration of the $MoO_2(acac)_2$ ethanol solution. The UV-vis spectra of crystalline MoO_3 (Fujifilm Wako Pure Chemical Corp., Osaka, Japan) was measured for comparison with MoO_x-modified HAp (see **Fig. 4.4**). The result indicates that the new absorption band is attributable to the quantum size effect of the intrinsic bandgap absorption of MoO_3 [8, 9].

Results of XPS analysis revealed the surface atomic ratios (%) of Mo against Ca, P, and Ti [Mo/(Mo+Ca+P+Ti)] for the samples as 1.9(TH-E1-4mM), 3.0(TH-E1-8mM), 4.5(TH-E2-8mM), 1.9(H-E1-4mM), 3.2(H-E1-8mM), and 5.2(H-E2-8mM). Results show that the same conditions of CCC technique provided almost equal Mo surface concentrations for Ti-HAp and HAp. However, XPS analysis was insufficient for the other samples because of

the very low Mo concentration. The peak intensity was on the same level of background noise. Therefore, the Mo concentrations of all samples were evaluated using ICP analysis. Chemical compositions obtained from ICP analysis are presented in **Table 4.1** and **Table 4.2**. It is noteworthy that the atomic ratio between Ti and P (Ti/P) was constant (0.16–0.18) among MoO_x-modified Ti-HAp samples and that the atomic ratio of Ca to P (Ca/P) was constant (1.58–1.62) among MoO_x-modified HAp samples. Therefore, comparison of Mo concentration among MoO_x-modified Ti-HAp and MoO_x-modified HAp was shown as the atomic ratio of Mo against P. The Mo concentration increased concomitantly with increasing Mo modification cycle or the $MoO_2(acac)_2$ ethanol solution concentration. In fact, Mo modification by CCC technique provided a wider range of Mo concentrations than that found from those prepared through impregnation method using aqueous solution of $CaMoO_4$ in **Chapter 3** [1].

4.3.2. Photocatalytic activity

Figures 4.5(a) and **4.5(b)** respectively present the concentration changes of gaseous IPA and CO_2 against UV illumination time of MoO_x-modified Ti-HAp. The initial concentration of IPA (C_0) before UV illumination is shown on the y-axis of **Fig. 4.5(a)**. The practical average value of C_0 is around 520 ppm, indicating that this Mo modification does not affect absorption capability against IPA. After UV illumination, the IPA concentration reached zero within 6 h for Ti-HAp before Mo-modification (TH). The MoO_x-modified Ti-HAp samples showed a higher IPA decomposition rate than that of TH except for TH-E2-8mM and TH-E3-8mM (not portrayed in **Fig. 4.5(a)**), which have high Mo concentration. It is noteworthy that the decomposition pathway from IPA to CO_2 by photocatalytic oxidation includes several steps [10–13]. To compare the photocatalytic activity among these samples,

the CO_2 generation rate (K_{CO2}) at the initial stage (0–6 h) was calculated in the linear range from the relation between the CO_2 generation and the UV illumination time as shown in **Table 4.1**. The highest CO_2 generation of MoO_x-modified Ti-HAp (177 ppm/h) was almost 13 times higher than that of Ti-HAp (14 ppm/h). However, TH-E2-8mM and TH-E3-8mM respectively provided lower CO_2 generation rates than that of Ti-HAp: 8 ppm/h and 5 ppm/h.

Figures 4.5(c) and **4.5(d)** respectively portray the concentration changes of gaseous IPA and CO_2 against UV illumination time of MoO_x-modified HAp. The practical average value of C_0 is around 635 ppm, which means that this Mo modification does not affect absorption capability against IPA. The bare HAp exhibited almost no decomposition activity because of its bandgap (>6 eV). Photon energy from the Hg-Xe lamp (**Fig. 3.1** in **Chapter 3**) was insufficient to excite electrons in the valence band of HAp. However, MoO_x-modified HAp provided a decrease of IPA concentration under UV illumination. The CO_2 generation rate increased concomitantly with increasing Mo concentration, as listed in **Table 4.2**.

Figure 4.6 presents the relation between the Mo concentration and the CO_2 generation rates of all samples. For MoO_x-modified Ti-HAp prepared using CCC technique, the photocatalytic activity under UV illumination increased concomitantly with increasing Mo concentration up to about 0.72 mol% against P. The increasing trend of the photocatalytic activity in this range of Mo concentration was similar to that of MoO_x-modified Ti-HAp found in **Chapter 3** prepared through impregnation method using an aqueous solution of $CaMoO_4$ (see **Fig. 4.7**) [1]. The slight difference might be attributable to the contribution of solution/precipitation, which leads to difference in the cluster size distribution in aqueous media for samples of the earlier study. By increasing the Mo concentration further to more than 0.72 mol% against P, the photocatalytic activity decreased markedly because the excessive amount of MoO_x clusters covered the activated site of Ti-HAp. Regarding

MoO_x-modified HAp by CCC technique, the photocatalytic activity under UV illumination increased concomitantly with increasing Mo concentration. It is noteworthy that MoO_3 possesses photocatalytic activity under UV illumination [14, 15]. When using Mo modification onto HAp, the photocatalytic activity of MoO_x cluster was enhanced because of the excellent affinity against organic compounds of HAp [16, 17]. In addition, due to the wide bandgap energy of HAp, HAp is transparent under UV illumination. All of the photon energy from the Hg-Xe lamp was absorbed by MoO_x clusters on HAp. Unlike MoO_x-modified Ti-HAp, Ti-HAp absorbed most of the photon energy from the Hg-Xe lamp. Only small amount of the photon energy was absorbed by MoO_x clusters on Ti-HAp surface. From these results, we can consider that the photocatalytic activity of TH-E samples with Mo concentration more than 2 mol% against P (TH-E2-8mM and TH-E3-8mM) were lower than that of H-E2-8mM.

4.3.3. Electron spin resonance and photoluminescence measurements

Figure 4.8(a) shows ESR spectra and the effects of UV illumination for MoO_x-modified Ti-HAp by CCC technique (TH-E1-4mM). In the dark, the signal at 344 mT (g = 1.999) was observed. This signal was attributed to oxygen vacancies and crystalline defects [18, 19], suggesting that some defects exist in the Ti-HAp structure by the substitution of Ti ion. Under UV illumination, the sample produced the signal at 334 mT (g = 2.057), which corresponds to that of absorbed oxygen radical [20, 21]. That signal indicates that some slight amount of adsorbed oxygen molecules remains on the sample surface. Signals corresponding to trapped holes were observed at 341 and 343 mT (g = 2.014 and 2.004) [22, 23]. A signal attributable to trapped electrons observed at 346 mT (g = 1.988) [41, 42] for Ti-HAp and TH-A3 [1] was absent for this sample. Regarding MoO_x-modified Ti-HAp (TH-E1-4mM), the signal

corresponding to Mo(V) was observed at 358 mT (g = 1.924) [24] under UV illumination. A similar trend was obtained also for MoO_x-modified Ti-HAp prepared through impregnation method using aqueous solution of $CaMoO_4$ [1] (see **Fig. 4.9**). This result suggests that the Mo species of MoO_x-modified Ti-HAp prepared using CCC technique and impregnation method using aqueous solution of $CaMoO_4$ would be the same. It is noteworthy that Mo(VI) is inert for ESR analysis. According to the Mo modification by CCC technique, one can expect that the initial state of the clusters is MoO_x with Mo(VI) as the dominant valence state, which was confirmed by XPS analysis. Under UV illumination, the photoinduced electrons in Ti-hybridized band transferred to MoO_x clusters and reduced Mo(VI) to Mo(V). From the ESR spectra of TH-E1-4mM, the intensity of Mo(V) signal and trapped holes signal were stronger than that of TH-A3 (**Fig. 4.9**). Furthermore, the signal of trapped electrons was absent, suggesting a smooth electron transfer from Ti-hybridized band to MoO_x clusters. This electron transfer process suppresses the recombination of the photoinduced electron and hole pairs that provide higher photocatalytic activity. A similar ESR result of TH-E1-8mM was obtained under the same measurement conditions (**Fig. 4.9**). Slight differences are expected to be attributable to differences in the Mo concentration.

Figures 4.8(b–d) depict ESR spectra and some effects of UV illumination for HAp and MoO_x-modified HAp (H-A3 and H-E1-8mM). In the dark, a signal attributable to oxygen vacancies or crystalline defects was observed at 344 mT (g = 1.999) [18, 19] for all samples. Results suggest that some defects occur during manufacturing using a commercial HAp process (Ca/P ratio is not 1.67). Under UV illumination, HAp, H-A3, and H-E1-8mM gave the signal at 334 mT (g = 2.057), which corresponds to that of absorbed oxygen radical [20, 21]. That signal indicates that some amount of adsorbed oxygen molecules remains on the sample surface. However, the difference in the intensity of that signal does not affect the

photocatalytic activity of these samples. A signal of Mo(V) was observed at 358 mT (g = 1.924) [24] under UV illumination only for the H-E1-8mM sample, as presented in **Fig. 4.8(d)**. The plausible reason for the absence of the signal of Mo(V) for H-A3 might be the very low Mo concentration. As described above, the initial state of clusters is MoO_x with Mo(VI) as the dominant valence state. The ESR results indicate that Mo(VI) was reduced to Mo(V). Considering little difference in UV-Vis spectra by Mo modification in Ti-HAp and the PO_4^{3-} bonding nature, direct electron transition from the valence band of HAp to the MoO_x cluster is expected to be infeasible [25]. The expected reason for the appearance of Mo(V) under UV illumination for H-E1-8mM is self-reduction by photocatalytic decomposition of adsorbed organic compound through an internal electron transfer of MoO_x from the highest occupied molecular orbital (HOMO) to the lowest unoccupied molecular orbital (LUMO) under UV illumination [26]. This reason may correspond also for MoO_x-modified Ti-HAp by CCC technique (TH-E1-4mM and TH-E1-8mM, in **Fig. 4.8(a)** and **4.9(c)**, respectively). Despite the similar Mo concentration of TH-E1-8mM and H-E1-8mM, TH-E1-8mM provided higher intensity of Mo(V) signal than that of H-E1-8mM because the electron transfer from Ti-hybridized band to MoO_x clusters occurred in addition to the self-reduction of MoO_x clusters. However, because of significant activity difference between MoO_x-modified Ti-HAp and MoO_x-modified HAp, we can consider that dominant charge transfer pathway between these two samples are different.

Figure 4.10 portrays PL emission spectra of Ti-HAp and MoO_x-modified Ti-HAp observed at 300–600 nm wavelengths. It is apparent that all samples exhibit PL emission spectra in the range of 300–590 nm. The PL emission peaks attributable to the excitonic PL were observed at wavelengths of 370–550 nm. The substitution of Ti ion at Ca sites creates many surface oxygen vacancies and crystalline defects in Ti-HAp particles, which might

involve excitonic PL emissions [27, 28]. After Mo modification, the intensities of PL emission peaks near the band–band PL peak (335 nm for the bandgap of 3.72 eV) were lower for both TH-E1-4mM and TH-A3. The slightly difference in PL emission intensities might be attributable to the differences in the Mo concentration and the cluster size distribution. These results suggest that the recombination of photoinduced electron and hole pairs near the Ti-hybridized band was suppressed by charge transfer of electrons from Ti-hybridized band to MoO_x clusters. Unfortunately, the PL measurement of MoO_x-modified HAp was insufficient because of its wide bandgap (>6 eV). The PL emission peaks were attributable solely to excitonic PL from surface oxygen vacancies and crystalline defects in the HAp structure [27, 28]. The band–band PL emission peaks were not observable in these samples.

4.3.4. Feasible electron transfer mechanism

As the results showed, we can expect that the charge transfer mechanisms of MoO_x-modified Ti-HAp by CCC technique and impregnation method using aqueous solution of $CaMoO_4$ are the same. **Figure 4.11(a)** presents a schematic illustration of the expected charge transfer mechanism of MoO_x-modified Ti-HAp. As described in **Chapter 3** [1], the electrons in the valence band are excited to Ti-hybridized band under UV illumination. Then the photoinduced electrons in Ti-hybridized band can transfer to MoO_x cluster. It is noteworthy that the potential of Ti-hybridized band (E^0 = -0.160 V, vs. NHE, pH = 0) [1] is lower than that of Mo(VI)/Mo(V) (E^0 = 0.400 V, vs. NHE, pH = 0) [29] or MoO_3/MoO_2 (E^0 = 0.320 V, vs. NHE, pH = 0) [30], which suggests that the electron transfer pathway is feasible. After the electron transfer to the clusters, the photoinduced electrons can reduce oxygen by two-electron reduction (O_2/H_2O_2, E^0 = 0.695 V, vs. NHE, pH = 0) [31, 32]. Then the photoinduced holes remaining in the valence band can oxidize organic compounds such as

IPA and acetone. Therefore, this electron transfer provides charge separation of the photoinduced electron and hole pairs, which enhances the photocatalytic activity in this system. However, the direct electron transfer from the valence band to the cluster via interfacial charge transfer is insufficient probably because the valence band of Ti-HAp is composed of the covalent bonding of PO_4^{3-}, as described in an earlier report [25]. Using CCC technique, Mo concentration can be increased to more than obtainable using impregnation method with an aqueous solution of $CaMoO_4$. The optimal Mo concentration to achieve the highest photocatalytic activity is approximately 0.72 mol% against P, which is higher than in **Chapter 3** [1]. The further increase of Mo concentration to more than 0.72 mol% against P decreased the photocatalytic activity because the excessive amount of MoO_x clusters covered the activated site of Ti-HAp and because the primary photocatalytic activity of MoO_x cluster is lower than that of Ti-HAp. Results show that the Mo concentration at about 0.72 mol% against P is an appropriate concentration for the distribution of MoO_x clusters onto Ti-HAp surface without covering the activated site of Ti-HAp and the effective enhancement of charge separation.

Figure 4.11(b) presents the expected charge transfer pathway of MoO_x-modified HAp. Because of the wide bandgap of HAp, electrons in the valence band are unable to excite to the conduction band of HAp under UV illumination. Moreover, like Ti-HAp, the direct electron transfer from the valence band to MoO_x clusters is also insufficient because of the covalent bonding of PO_4^{3-}. Therefore, a plausible explanation of the decomposition of IPA under UV illumination of MoO_x-modified HAp is the photocatalytic activity of MoO_x clusters on the HAp surface [14, 15]. Under UV illumination, the electrons in the HOMO level are excited to the LUMO level of the MoO_x clusters. Then the excited electrons in LUMO level can reduce oxygen. The photoinduced holes in the HOMO level can oxidize organic compounds such as

IPA and acetone.

From XPS results, TH-E1-4mM and H-E1-4mM possessed the almost the same Mo surface atomic ratio (~ 1.9%). However, CO_2 generation rates are 177 ppm/h and 11.6 ppm/h, respectively. Although specific surface area of TH-E1-4mM is 30% greater than that of H-E1-4mM, this activity difference is remarkable indicated that the adsorption capability difference does not play an important role in the photocatalytic activity increase of MoO_x-modified Ti-HAp. The activity difference between MoO_x-modified Ti-HAp and MoO_x-modified HAp suggests that the mechanisms governing the photocatalytic activity of these two materials differ. Thus, the MoO_x cluster makes no great contribution to the overall photocatalytic activity increase of MoO_x-modified Ti-HAp.

These experimentally obtained results confirm that the Mo state of MoO_x-modified Ti-HAp prepared using impregnation method with the aqueous solution of $CaMoO_4$ in **Chapter 3** [1] was MoO_x. Differences between CCC technique and the impregnation method using aqueous solution of $CaMoO_4$ would be the Mo concentration and the distribution of MoO_x clusters on the sample surface. Detailed characterization on the cluster structure using CCC technique and using impregnation of aqueous solution of $CaMoO_4$ should be undertaken in future studies.

4.4. Summary

For this chapter, we modified Ti-HAp and HAp by CCC technique and impregnation method using an aqueous solution of $CaMoO_4$. Then we evaluated UV light photocatalytic activity by decomposition of gaseous IPA. The crystal structure, morphology, light absorption, and specific surface area of MoO_x-modified Ti-HAps were almost identical after Mo modification. The photocatalytic activity increased with concomitantly increasing Mo

concentration until 0.72 mol% against P; then it decreased considerably. Results of ESR and PL analysis suggest that the electron transfer from the Ti-hybridized band to MoO_x clusters leads to charge separation of photoinduced electron and hole pairs. Results were similar for both Mo modification methods: the Mo state of MoO_x-modified Ti-HAp by impregnation method using aqueous solution of $CaMoO_4$ was also MoO_x. For MoO_x-modified HAp, a new absorption band was observed in the UV range. This absorption band change was attributable to the quantum size effect of the MoO_x cluster. Then MoO_x-modified HAp exhibited photocatalytic activity under UV illumination because of the photoexcitation of MoO_x clusters. However, the photocatalytic activity of MoO_x cluster does not play an important role in the entire activity increase of MoO_x-modified Ti-HAp.

References

[1] N. Jiraborvornpongsa, T. Isobe, S. Matsushita, M. Oshikiri, M. Wakamura, K. Fujii, M. Yashima, A. Nakajima, Preparation and photocatalytic activity of Mo-modified Ti-doped HAp, *Appl. Catal. B Environmental*, **243** (2019) 448−454.

[2] H. Tada, Q. Jin, H. Nishijima, H. Yamamoto, M. Fujishima, S. Okuoka, T. Hattori, Y. Sumida, H. Kobayashi, Titanium(IV) dioxide surface-modified with iron oxide as a visible light photocatalyst, *Angew. Chem. Int. Ed.*, **50** (2011) 3501−3505.

[3] Q. Jin, M. Fujishima, A. Iwaszuk, M. Nolan, H. Tada, Loading effect in copper(II) oxide cluster-surface-modified titanium(IV) oxide on visible- and UV-light activities, *J. Phys. Chem. C*, **117** (2013) 23848−23857.

[4] Q. Jin, T. Ikeda, M. Fujishima, H. Tada, Nickel(II) oxide surface-modified titanium(IV) dioxide as a visible-light-active photocatalyst, *Chem. Commun.*, **47** (2011) 8814−8816.

[5] M. Nolan, A. Iwaszuk, H. Tada, Molecular metal oxide cluster-surface modified titanium(IV) dioxide photocatalysts, *Aust. J. Chem.*, **65** (2012) 624−632.

[6] M. Tsukada, M. Wakamura, N. Yoshida, T. Watanabe, Band gap and photocatalytic properties of Ti-substituted hydroxyapatite: comparison with anatase-TiO_2, *J. Mol. Catal. A Chem*, **338** (2011) 18−23.

[7] A. Tsuruoka, T. Isobe, S. Matsushita, M. Wakamura, A. Nakajima, Comparison of photocatalytic activity and surface friction force variation on Ti-doped hydroxyapatite and anatase under UV illumination, *J. Photochem. Photobiol. A: Chem.*, **311** (2015) 160−165.

[8] D. O. Scanlon, G. W. Watson, D. J. Payne, G. R. Atkinson, R. G. Egdell, D. S. L. Law, Theoretical and experimental study of the electronic structures of MoO_3 and MoO_2, *J. Phys. Chem. C*, **114** (2010) 4636−4645.

[9] M. Anpo, T. Shima, S. Kodama, Y. Kubokawa, Photocatalytic hydrogenation of CH_3CCH with H_2O on small-particle TiO_2: size quantization effects and reaction intermediates, *J. Phys. Chem*., **91** (1987) 4305−4310.

[10] P. R. Harvey, R. Rudham, S. Ward, Photocatalytic oxidation of liquid propan-2-ol by titanium dioxide, *J. Chem. Soc. Faraday Trans.* 1, **79** (1983) 1381−1390.

[11] Y. Ohko, K. Hashimoto, A. Fujishima, Kinetics of photocatalytic reactions under extremely low-intensity UV illumination on titanium dioxide thin films, *J. Phys. Chem. A*, **101** (1997) 8057−8062.

[12] A. Mylonas, A. Hiskia, E. Androulaki, D. Dimotikali, E. Papaconstantinou, New aspect of the mechanism of photocatalytic oxidation of organic compounds by polyoxometalates in aqueous solutions. The selective photooxidation of propan-2-ol to propanone: The role of OH radicals, *Phys. Chem. Chem. Phys*., **1** (1999) 437−440.

[13] S. A. Larson, J. A. Widegren, J. L. Falconer, Transient studies of 2-propanol photocatalytic oxidation on titania, *J. Catal*., **157** (1995) 611−625.

[14] A. Arfaoui, S. Touihri, A. Mhamdi, A. Labidi, T. Manoubi, Structural, morphology, gas sensing and photocatalytic characterization of MoO_3 and WO_3 thin films prepared by the thermal vacuum evaporation technique, *Appl. Sur. Sci*., **357** (2015) 1089−1096.

[15] A. Chithambararaj, N. S. Sanjini, S. Velmathi, A. C. Bose, Preparation of h-MoO_3 and α-MoO_3 nanocrystals: comparative study on photocatalytic degradation of methylene blue under visible irradiation, *Phys. Chem. Chem. Phys.*, **15** (2015) 14761−14769.

[16] T. Nonami, H. Hase, K. Funakoshi, Apatite-coated titanium dioxide photocatalyst for air purification, *Catal. Today*, **96** (2004) 113−118.

[17] M. Hu, Z. Yao, X. Liu, L. Ma, Z. He, X. Wang, Enhancement mechanism of hydroxyapatite for photocatalytic degradation of gaseous formaldehyde over

TiO_2/hydroxyapatite, *J. Taiwan Ins. Chem. Eng.*, **85** (2018) 91−97.

[18] H. Monma, S. Ueno, T. Kanazawa, Properties of hydroxyapatite prepared by the hydrolysis of tricalcium phosphate, *J. Chem. Tech. Biotechnol*., **31** (1981) 15−24.

[19] I. Nakamura, N. Neigishi, S. Kutsuna, T. Ihara, S. Sugihara, K. Takeuchi, Role of oxygen vacancy in the plasma-treated TiO_2 photocatalyst with visible light activity for NO removal, *J. Mol. Catal. A: Chem.*, **161** (2000) 205−212.

[20] P. H. Kasai, Electron spin resonance studies of γ- and X-ray-irradiated zeolites, *J. Chem. Phys*., **43** (1965) 3322−3327.

[21] J. H. Lunsford, ESR of adsorbed oxygen species, *Catal. Rev*., **8** (1973) 135−157.

[22] Y. Nakaoka, Y. Nosaka, ESR investigation into the effects of heat treatment and crystal structure on radicals produced over irradiated TiO_2 powder, *J. Photoch. Photobio. A: Chem.*, **110** (1997) 299−305.

[23] J. M. Coronado, A. J. Maira, J. C. Conesa, K. L. Yeung, V. Augugliaro, J. Soria, EPR study of the surface characteristics of nanostructured TiO_2 under UV irradiation, *Langmuir*, **17** (2001) 5368−5374.

[24] K. C. Khulbe, R. S. Mann, M. Ternan, Electron spin resonance studies of the surface chemistry of molybdenum-alumina catalysts, *Can. J. Chem*., **56** (1978) 1769−1772.

[25] M. Nishikawa, W. Yang, Y. Nosaka, Grafting effects of Cu^{2+} on the photocatalytic activity of titanium-substituted hydroxyapatite, *J. Mol. Catal. A Chem*., **378** (2013) 314−318.

[26] H. J. Wagner, P. Driessen, C. F. Schwerdtfeger, EPR of Mo^{5+} in amorphous MoO_3 thin films, *J. Non-Cryst. Solids*, **34** (1979) 335−338.

[27] J. Liqiang, Y. Fulong, H. Haige, X. Baifu, C. Weimin, F. Honggang, Relationships of surface oxygen vacancies with photoluminescence and photocatalytic performance of

ZnO nanoparticles, *Sci. Chin. B*, **48** (2005) 25−30.

[28] D. Aronov, A. Karlov, G. Rosenman, Hydroxyapatite nanoceramics: Basic physical properties and biointerface modification, *J. Euro. Cer. Soc*., **27** (2007) 4181−4186.

[29] Lange's Handbook of Chemistry 12th edition, Ed. J. A. Dean, McGrow-Hill Inc., New York, pp6−12 (1976).

[30] Kagaku Binnran Third edition, Ed. The Chemical Society of Japan, Maruzen, Tokyo Japan, ppII--475 (1988) [in Japanese].

[31] I. V. Kozhevnikov, Catalysis by heteropoly acids and multicomponent polyoxometalates in liquid-phase reactions, *Chem. Rev*., **98** (1998) 171−198.

[32] Y. Nosaka, S. Takahashi, H. Sakamoto, A. Y. Nosaka, Reaction mechanism of Cu(II)-grafted visible-light responsive TiO_2 and WO_3 photocatalysts studied by using ESR spectroscopy and chemiluminescence photometry, *J. Phys. Chem. C*, **115** (2011) 21283−21290.

Table 4.1 Chemical compositions obtained from ICP analysis, the CO_2 generation rate, and specific surface area of Mo-modified Ti-HAp [*] The Mo/Ti ratio, K_{CO2}, and SSA of TH-A samples were obtained from the samples prepared in Chapter 3.

Sample name	Mo/Ti* [mol%]	Mo/P [mol%]	K_{CO2}* [ppm/h]	SSA* [m^2/g]
TH (Ti-HAp)	-	0	14	39
TH-A1	0.16	0.026	44	36
TH-A2	0.33	0.055	82	35
TH-A3	1.21	0.207	112	37
TH-A4	1.10	0.186	121	38
TH-A5	0.91	0.154	121	37
TH-A6	0.64	0.114	123	39
TH-A7	0.50	0.088	131	39
TH-A8	0.46	0.078	121	37
TH-E1-0.08mM	0.09	0.014	36	38
TH-E2-0.08mM	0.17	0.027	48	37
TH-E3-0.08mM	0.25	0.039	66	36
TH-E1-0.8mM	0.85	0.132	81	36
TH-E2-0.8mM	1.63	0.261	103	37
TH-E3-0.8mM	2.47	0.399	116	35
TH-E1-4mM	4.36	0.720	177	38
TH-E1-8mM	7.64	1.230	73	36
TH-E2-8mM	14.02	2.269	8	33
TH-E3-8mM	18.82	3.045	5	28

Table 4.2 Chemical compositions obtained from ICP analysis, the CO_2 generation rate, and specific surface area of Mo-modified HAp

Sample name	Mo/P [mol%]	K_{CO2} [ppm/h]	SSA [m^2/g]
H (HAp)	0	0.5	32
H-A1	0.022	1.2	27
H-A2	0.029	0.6	27
H-A3	0.034	0.9	31
H-E1-0.8mM	0.123	1.9	28
H-E2-0.8mM	0.279	5.8	29
H-E1-4mM	0.649	11.6	29
H-E1-8mM	1.258	43.0	30
H-E2-8mM	2.434	30.5	25

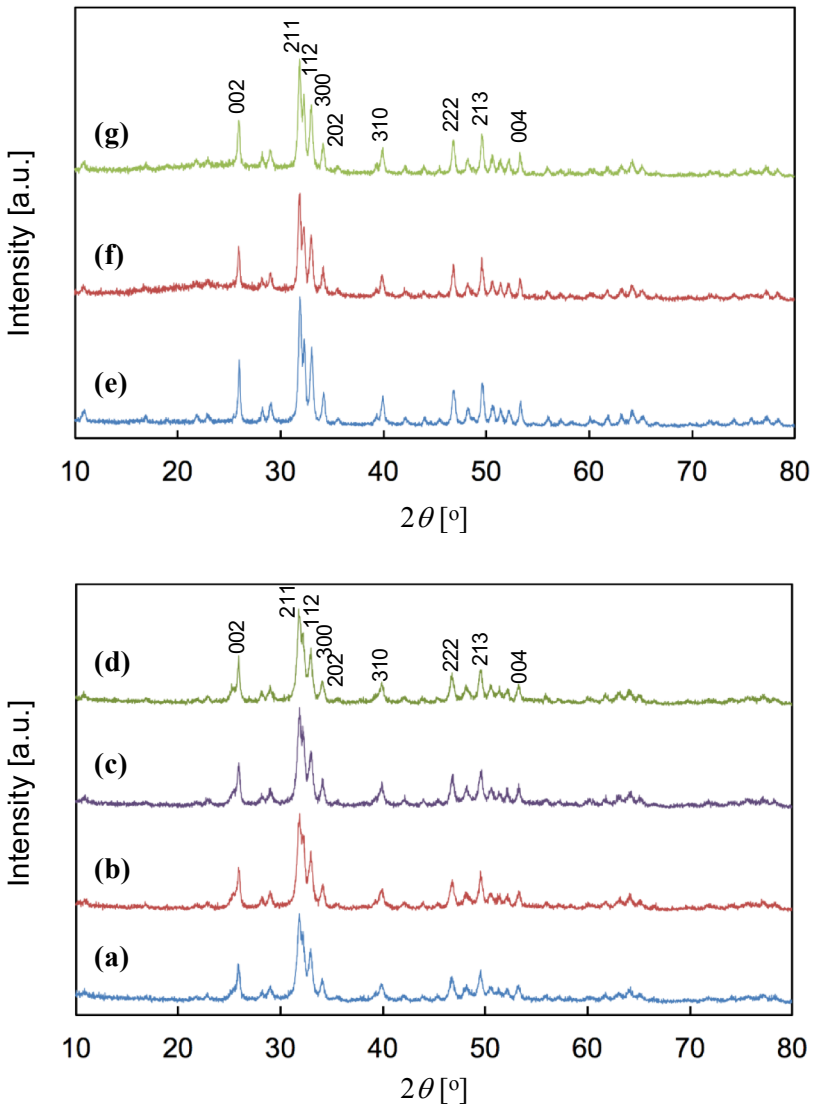

Figure 4.1 XRD patterns of sample powders: (a) Ti-HAp, (b) TH-E1-8mM, (c) TH-E2-8mM, (d) TH-E3-8mM, (e) HAp, (f) H-E1-8mM, and (g) H-E2-8mM.

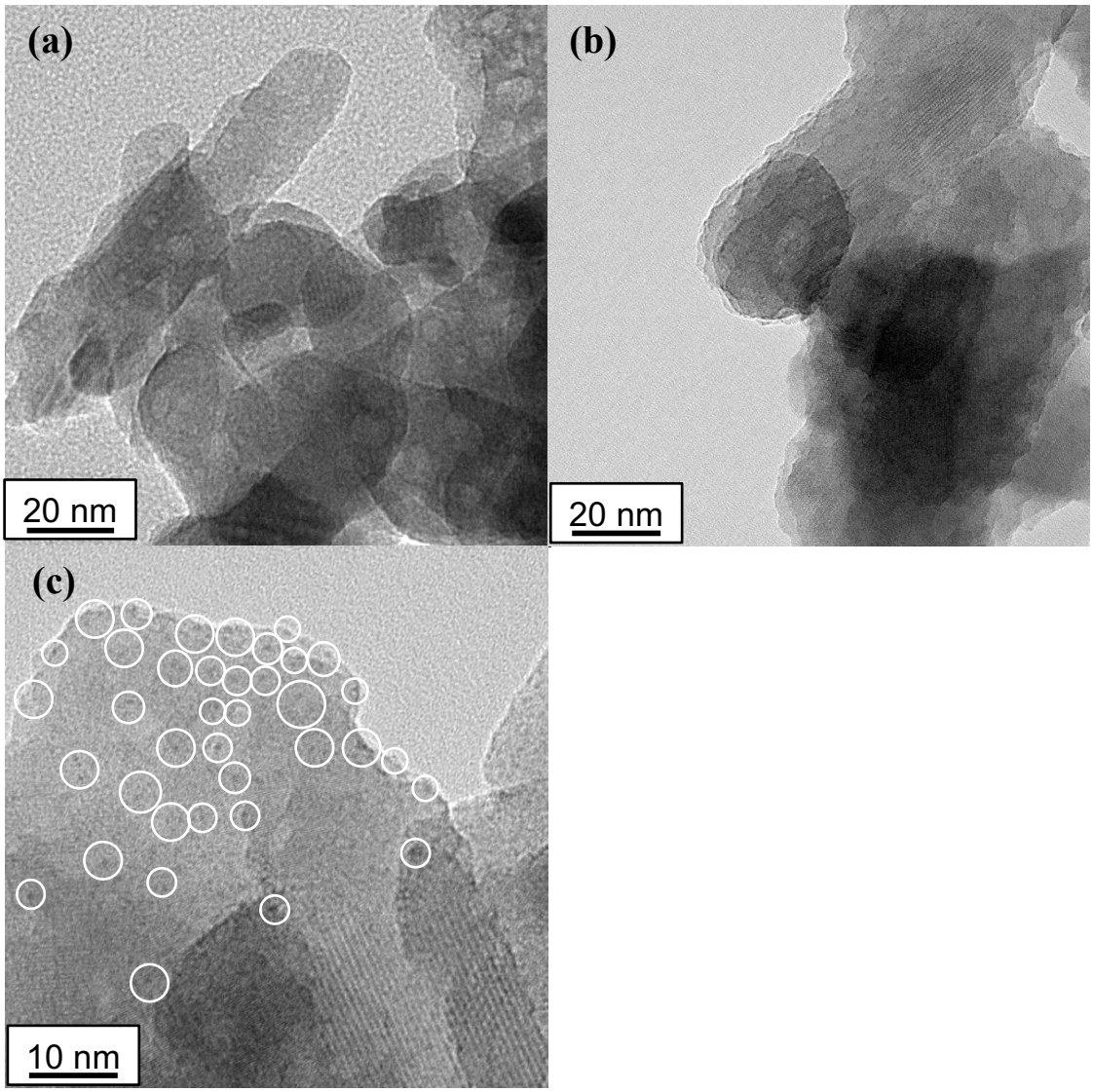

Figure 4.2 TEM micrographs of Ti-HAp particles: (a) before Mo-modification and (b, c) after Mo-modification (sample: TH-E3-8mM).

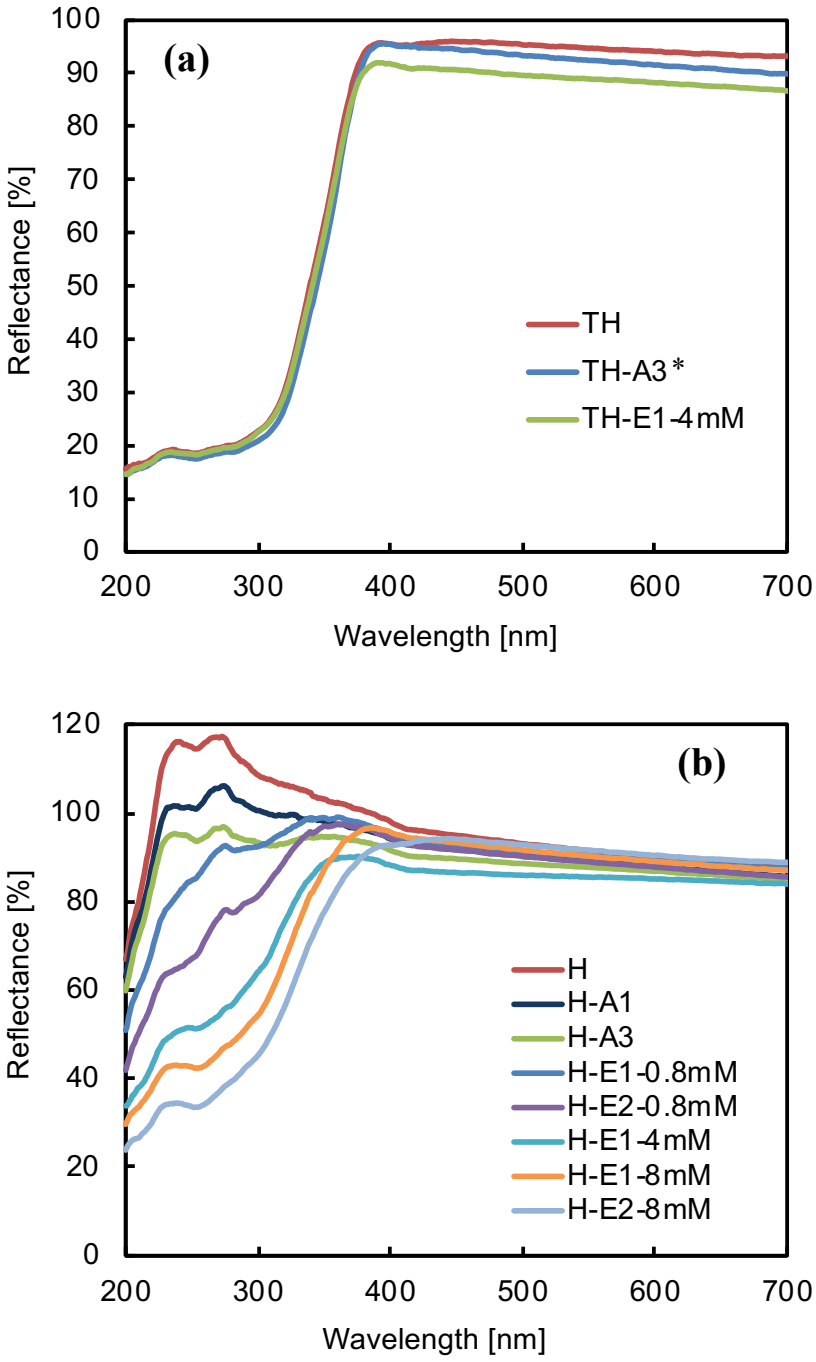

Figure 4.3 UV-vis spectra of (a) Mo-modified Ti-HAp and (b) Mo-modified HAp [*] TH-A3 was obtained from the sample prepared in Chapter 3.

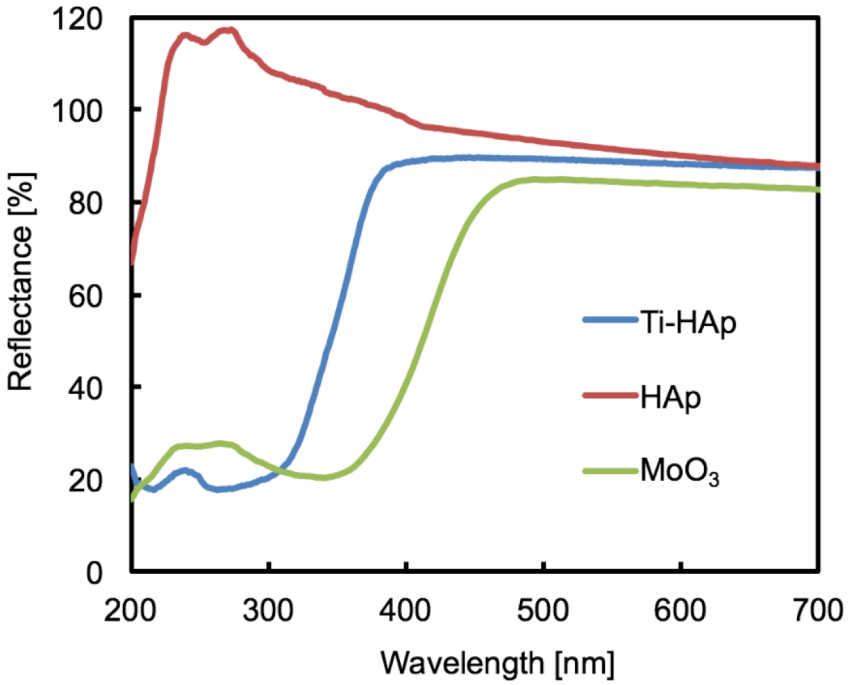

Figure 4.4 UV-vis spectra of Ti-HAp, HAp, and MoO_3.

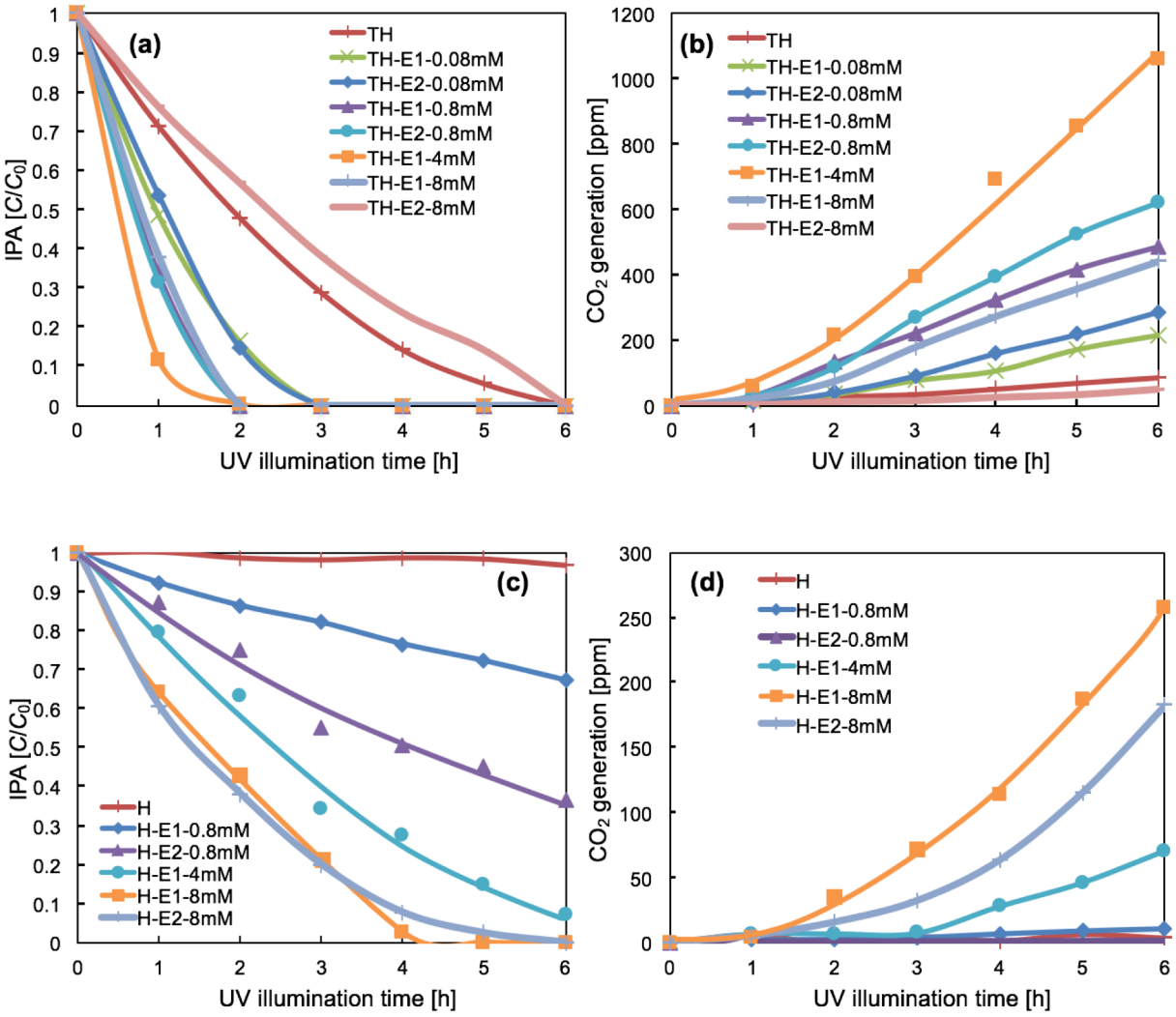

Figure 4.5 Concentration changes of (a) gaseous IPA of Mo-modified Ti-HAp, (b) CO_2 of Mo-modified Ti-HAp, (c) gaseous IPA of Mo-modified HAp, and (d) CO_2 of Mo-modified HAp against UV illumination time.

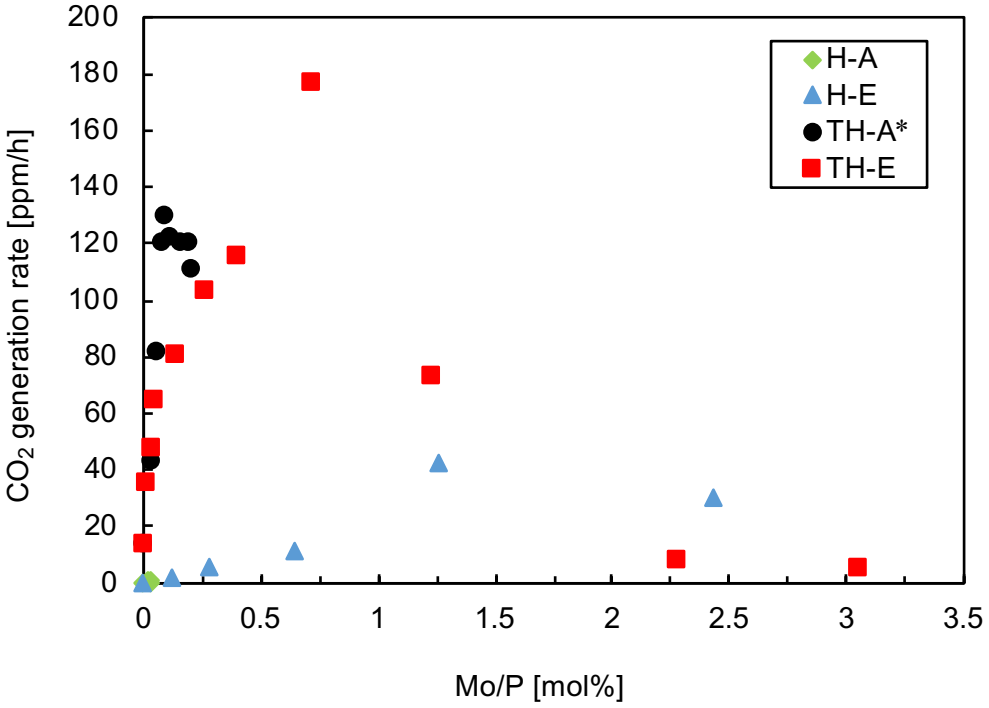

Figure 4.6 Relation between the Mo concentrations and the CO_2 generation rates of all samples [*] Data of TH-A (black circle) were obtained form samples prepared in Chapter 3.

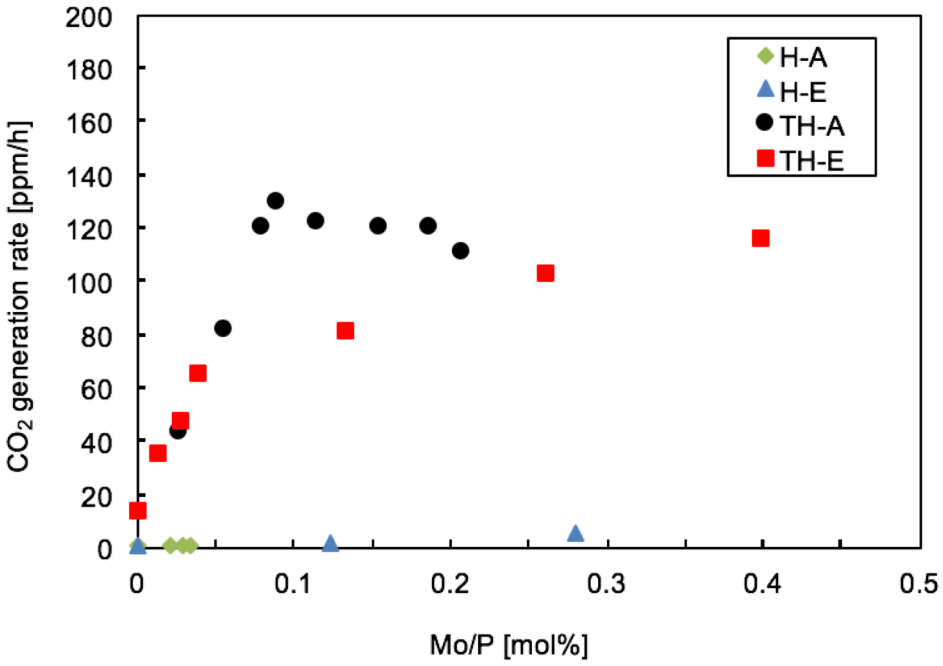

Figure 4.7 Relation between the Mo concentrations and the CO_2 generation rate of samples (enlarged figure) [*] The data of TH-A (black circle) were obtained from the samples prepared in Chapter 3.

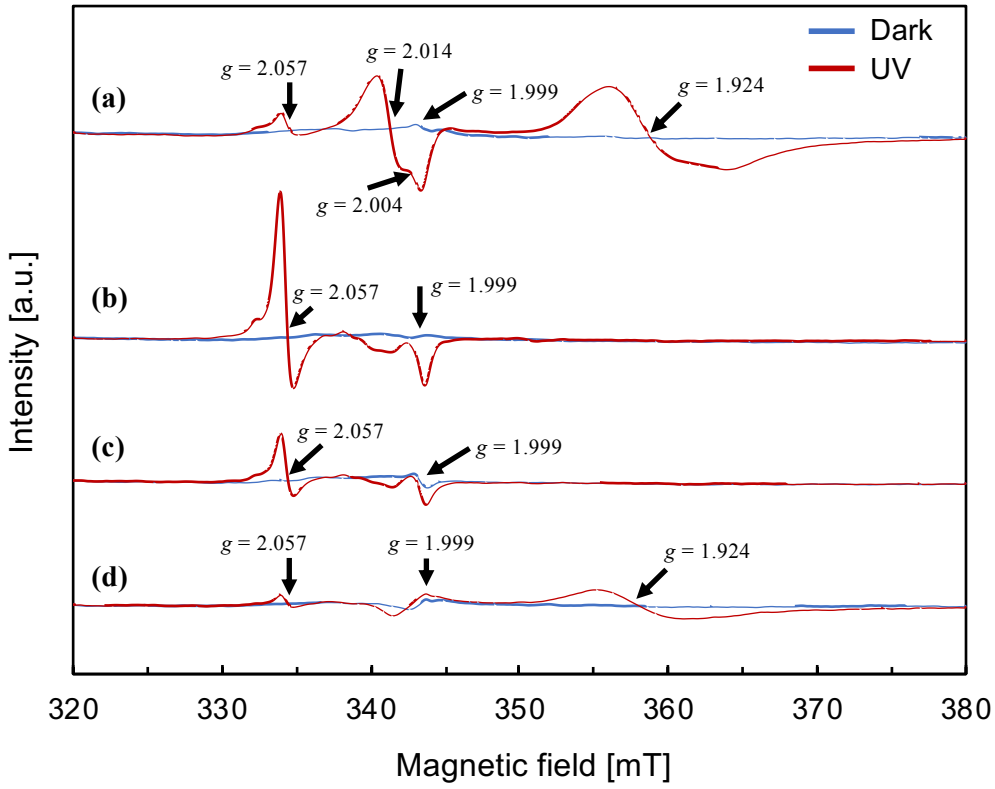

Figure 4.8 ESR spectra of (a) TH-E1-4mM, (b) HAp, (c) H-A3, and (d) H-E1-8mM showing UV illumination effects.

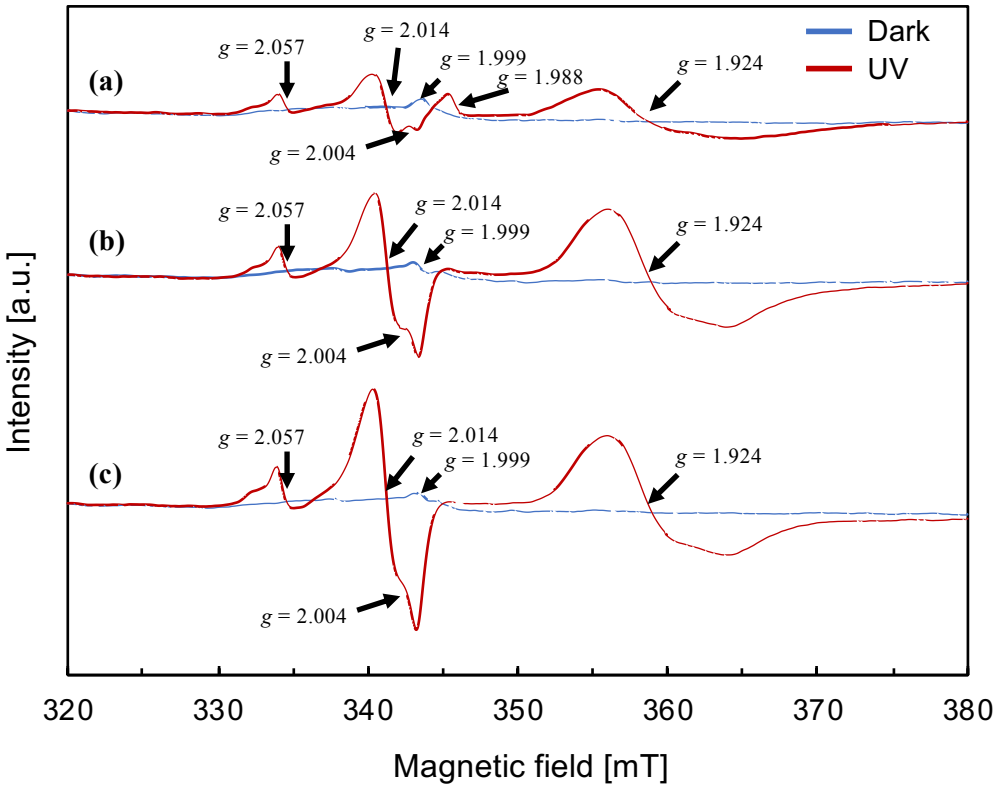

Figure 4.9 ESR spectra of (a) TH-A3, (b) TH-E1-4mM, and (c) TH-E1-8mM [*] The data of TH-A3 was obtained from the sample prepared in Chapter 3.

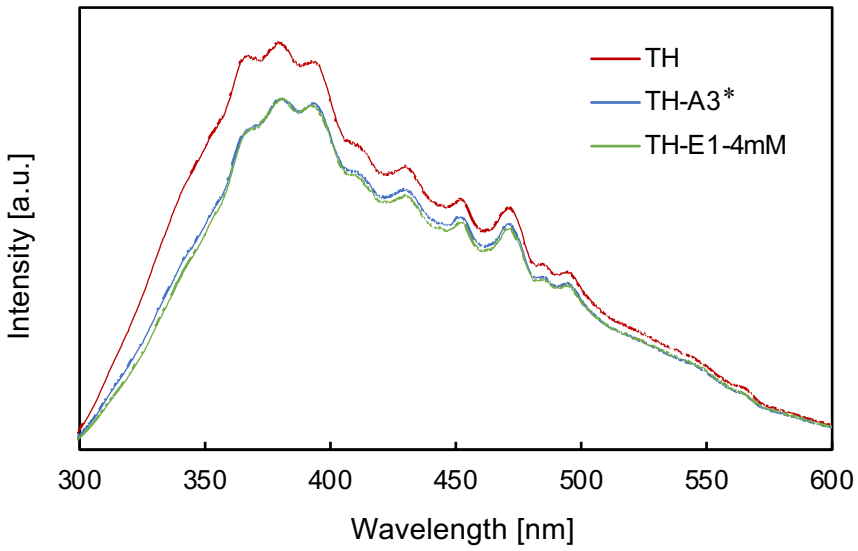

Figure 4.10 PL emission spectra of Ti-HAp, TH-A3, and TH-E1-4mM with excitation wavelength of 280 nm [*] TH-A3 was obtained from a sample prepared in Chapter 3.

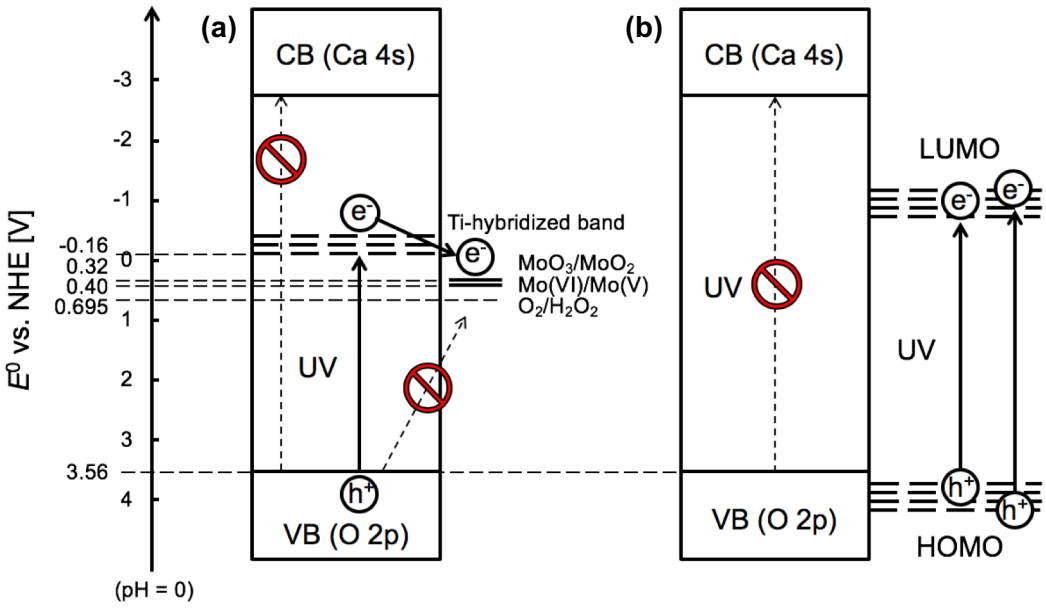

Figure 4.11 Feasible charge transfer process under UV illumination of (a) Mo-modified Ti-HAp and (b) Mo-modified HAp.

CHAPTER 5

Summary

5.1. Results and conclusions

CHAPTER 1

Background and objective of this research are mentioned in this chapter. Recently, photocatalytic materials have received more attention due to its applications for environmental purification. Titanium dioxide (TiO_2) is one of the most well-studied photocatalytic material due to its high oxidation power, low toxicity, and good chemical stability. Despite its promising properties, TiO_2 has low affinity against organic compounds, which makes it has low photocatalytic activity. On the other hand, hydroxyapatite (HAp), which has high affinity against organic compounds, is a candidate for high photocatalytic activity material. Due to its wide bandgap energy (> 6 eV), HAp could not provide photocatalytic activity. To reduce bandgap energy of HAp, titanium atoms were doped at calcium sites of hydroxyapatite. Titanium-doped hydroxyapatite (Ti-HAp) possesses high affinity against organic compound and photocatalytic activity under UV illumination. The maximum dopable Ti amount is ca. 10 mol% of Ca to retain hydroxyapatite structure. Therefore, the photocatalytic activity of Ti-HAp is restricted. Consequently, the primary photocatalytic activity of Ti-HAp is inferior to that of TiO_2. Several attempts have been conducted to enhance photocatalytic activity of Ti-HAp, but their outcomes fell short of expectations. In this study, Ti-HAp particles were modified with Mo-base solutions (either $CaMoO_4$ or $MoO_4(C_5H_7O_2)_2$). The photocatalytic activity of MoO_x-modified Ti-HAp increased several times compared with bare Ti-HAp.

CHAPTER 2

In this chapter, anatase and rutile phases of TiO_2 with almost identical specific surface area were modified with Fe-base solutions using two different modification processes (impregnation method using aqueous solution of $FeCl_3$ or chemisorption calcination cycle (CCC) using organic solution of $Fe(C_5H_7O_2)_3$). Their photocatalytic activities under visible illumination were evaluated by the decomposition of gaseous IPA to CO_2. The Fe-modified rutile powders exhibited high visible light photocatalytic activity. The binding energy of O 2p by XPS analysis revealed that the valence band top of the samples prepared from CCC decreases concomitantly with increasing Fe concentration. Results suggest that a difference in modification process engenders different mechanisms of photocatalytic activity for Fe-modified TiO_2 under visible light. In case of impregnation method using $FeCl_3$, the electrons in valence band are transferred directly to Fe(III) ions via IFCT, producing Fe(II) ions capable of reducing oxygen by multi-electron reduction processes. On the other hand, CCC technique, the electrons are excited from the surface d sub-band, yielded by mixing between the surface Fe(III) levels and O 2p by the Ti–O–Fe interfacial bond to the conduction band of TiO_2. Because of the smaller initial bandgap, Fe modification by both processes is expected to be more effective for rutile than for anatase.

These Fe modification processes were employed on Ti-HAp particles. However, the Fe-modified Ti-HAp did not provide the visible light photocatalytic activity. The direct electron transfer from the valence band to Fe cluster via IFCT is insufficient because the valence band of Ti-HAp comprises the covalent bonding of PO_4^{3-}. The valence electrons are localized between P and O atoms, leading to the difficulty in electronic excitation from O atom to Fe atom.

CHAPTER 3

In this chapter, we modified Ti-HAp with $CaMoO_4$ aqueous solution and evaluated UV light photocatalytic activity by the decomposition of gaseous IPA. After Mo modification, the crystal structure, morphology, light absorption, and specific surface area were almost identical. Small (ca. 1–2 nm) clusters were observed on the surface of MoO_x-modified Ti-HAp. The MoO_x-modified Ti-HAp exhibited higher photocatalytic activity than that of Ti-HAp. The photocatalytic activity of the MoO_x-modified samples increased concomitantly with increasing Mo concentration until 0.5% against Ti. Computer modeling indicated that MoO_4^{2-} doping into Ti-HAp structure plays no important role for activity increase. Results of ESR and PL analyses elucidated that the electron transfer from Ti 3d band to the MoO_x (Mo^{n+} ($n < 6$)) or Mo metallic cluster via wavefunction hybridization between the Ti 3d and the Mo 4d orbitals can suppress the recombination of photoinduced electron–hole pairs.

CHAPTER 4

In this chapter, we modified Ti-HAp and HAp by CCC technique and impregnation method using an aqueous solution of $CaMoO_4$. Then we evaluated UV light photocatalytic activity by decomposition of gaseous IPA. The crystal structure, morphology, light absorption, and specific surface area of MoO_x-modified Ti-HAps were almost identical after Mo modification. The photocatalytic activity increased with concomitantly increasing Mo concentration until 0.72 mol% against P; then it decreased considerably. Results of ESR and PL analysis suggest that the electron transfer from the Ti-hybridized band to MoO_x clusters leads to charge separation of photoinduced electron and hole pairs. Results were similar for both Mo modification methods: the Mo state of MoO_x-modified Ti-HAp by impregnation method using aqueous solution of $CaMoO_4$ was also MoO_x. For MoO_x-modified HAp, a new

absorption band was observed in the UV range. This absorption band change was attributable to the quantum size effect of the MoO_x cluster. Then MoO_x-modified HAp exhibited photocatalytic activity under UV illumination because of the photoexcitation of MoO_x clusters. However, the photocatalytic activity of MoO_x cluster does not play an important role in the entire activity increase of MoO_x-modified Ti-HAp.

5.2. Key success to enhance photocatalytic activity of Ti-HAp

The photocatalytic degradation of IPA under UV illumination of Ti-HAp increased several times by surface modification with MoO_x cluster. The photoinduced electrons in Ti-hybridized band can transfer to MoO_x cluster which has more positive potential than that of Ti-hybridized band. The photoinduced electrons in MoO_x cluster can reduce oxygen via multielectron reduction, while the photoinduced holes remain in the valence band, which they can oxidize organic compounds such as IPA and acetone. This charge transfer process promotes charge separation of the photoinduced electron and hole pairs, resulting in the increase in photocatalytic activity. However, the direct electron transfer from the valence band to MoO_x cluster via interfacial charge transfer is insufficient, probably because the valence band of Ti-HAp comprises the covalent bonding of PO_4^{3-}. Based on the starting materials, the cluster can be either MoO_3 or $CaMoO_4$. The density functional theory (DFT) calculation can be used to clarify the cluster state. From the result, the valence state of Mo in MoO_3 was calculated as ~+5 corresponding to the observed Mo(V) signal under UV illumination from ESR measurement. The Mo 4d orbitals of MoO_3 was filled by the injected electron from Ti 3d orbitals of Ti-hybridized band, which appeared below Ti 3d orbital. It indicated that the photoinduced electron in Ti-hybridized band can transfer to MoO_3 cluster. According to this calculation the cluster seems to be MoO_3.

The oxide cluster for surface modification should have following properties. First, its redox potential should locate between the potential of Ti-hybridized band and oxygen reduction. The photoinduced electrons can transfer from Ti-hybridized band to oxide cluster, subsequently transfer to oxygen via oxygen reduction. Second, the oxide cluster modification should not affect the surface chemical property of Ti-HAp. Ti-HAp should retain its high adsorption capability after surface modification. Third, the oxide cluster should have enough stability throughout the photocatalytic reaction. The repeatability of the catalyst is required.

The surface modification with oxide cluster provides remarkable improvement of the photocatalytic activity of Ti-HAp. The fundamental finding in this research can be applied to other oxide clusters for the surface modification of Ti-HAp from its electron structure and ionic radius. Recently, we found that the surface modification of WO_x also enhances the photocatalytic activity of Ti-HAp because tungsten is similar in many respects to molybdenum. They belong to the same group in the periodic table. Both WO_x and MoO_x clusters have six oxygen coordination number. The ionic radius and bonding length of WO_x and MoO_x clusters are similar. Furthermore, the redox potentials of W(VI)/W(V) or W(VI)/W(IV) are located between the potential of Ti-hybridized band and oxygen reduction similar to MoO_x modification. Therefore, the charge transfer process is also feasible for WO_x modification. Based on these finding, it is deduced that the existence of electron state between VB and the Ti-hybridized band (hopefully slightly lower than the Ti-hybridized band) in Ti-HAp is an important requirement for the effective cluster for modification. The DFT calculation suggested that the cluster with an insufficient coordination state with oxygen would be a candidate material.

Further detailed investigation of oxide cluster structure should be conducted by X-ray absorption fine structure (XAFS) analysis to figure out the configuration and local

coordination environment that might be useful for the identification of other oxide cluster with similar structure. The DFT calculation can be used to calculate the electronic structure which explain the possible charge transfer mechanism. Moreover, the DFT calculation can be applied to identify other oxide cluster that suitable for surface modification without conducting an experiment which can save time and resource. For the practical usage, the preparation procedure should be optimized to obtain the maximum performance material with the simplest preparation procedure. The chemisorption calcination cycle (CCC) technique might be the promising candidate for surface modification. It provides oxide cluster at molecular scale with high distribution. Furthermore, CCC process can adjust the modifiable amount of oxide cluster by changing the solution concentration without repetition of the entire process, which can save time and cost. The sequential modification system using a spray dram and a rotary kiln should reduce the entire process time and overcome the volume limitation for CCC technique. The content of this research paves the way to development of Ti-HAp with high photocatalytic performance.

List of publications

1. Noppakhate Jiraborvornpongsa, Toshihiro Isobe, Sachiko Matsushita, Akira Nakajima, "Comparative study on visible light photocatalytic activity of Fe-modified TiO_2 powders", *Journal of the Ceramic Society of Japan*, **124** (2016) 781−786. (**CHAPTER 2**)
2. Noppakhate Jiraborvornpongsa, Toshihiro Isobe, Sachiko Matsushita, Mitsutake Oshikiri, Masato Wakamura, Kotaro Fujii, Masatomo Yashima, Akira Nakajima, "Preparation and photocatalytic activity of Mo-modified Ti-doped HAp", *Applied Catalysis B: Environmental*, **243** (2019) 448−454. (**CHAPTER 3**)
3. Noppakhate Jiraborvornpongsa, Toshihiro Isobe, Sachiko Matsushita, Akira Yamaguchi, Masahiro Miyauchi, Masato Wakamura, Akira Nakajima, "Effect of MoO_x modification on photocatalytic activity of hydroxyapatite and Ti-doped hydroxyapatite", *Advanced Powder Technology*, **30** (2019) 1617−1624. (**CHAPTER 4**)

List of presentations

1. Noppakhate Jiraborvornpongsa, Toshihiro Isobe, Sachiko Matsushita, Masato Wakamura, Akira Nakajima, "Preparation and photocatalytic activity of Mo-doped Ti-HAp", *The Ceramic Society of Japan Annual Meeting 2017*, Japan, 2017 March 17−19th (Oral, domestic)
2. Noppakhate Jiraborvornpongsa, Toshihiro Isobe, Sachiko Matsushita, Masato Wakamura, Akira Nakajima, "Preparation and photocatalytic activity of Mo-doped Ti-HAp", *The 12th Pacific Rim Conference on Ceramic and Glass Technology*, USA, 2017 May 21−26th (Oral, international)
3. Noppakhate Jiraborvornpongsa, Toshihiro Isobe, Sachiko Matsushita, Masato Wakamura, Akira Nakajima, "Preparation and photocatalytic activity of Mo-doped Ti-HAp", *90th JSCM anniversary conference*, Japan, 2017 October 17−18th (Oral, international)
4. Noppakhate Jiraborvornpongsa, Toshihiro Isobe, Sachiko Matsushita, Kotaro Fujii, Masatomo Yashima, Mitsutake Oshikiri, Masato Wakamura, Akira Nakajima, "Preparation and photocatalytic activity of Mo-modified Ti-HAp (2)", *The 31st Fall Meeting of The Ceramic Society of Japan*, Japan, 2018 September 5−7th (Oral, domestic)

Acknowledgements

I would like to express my appreciation to all those who support me to complete this study. First of all, I would like to thank my supervisor Prof. Akira Nakajima for his guidance, encouragement and valuable discussion throughout my study. I also would like to thank Associate Prof. Sachiko Matsushita and Associate Prof. Toshihiro Isobe for their support, encouragement and advice.

I would like to thank Prof. Masahiro Miyauchi and Assistance Prof. Akira Yamaguchi for granting permission for me to use equipment in their laboratory and their valuable discussion. I would like to express my thank to Assistant Prof. Tetsuo Kishi for granting permission for me to use equipment in his laboratory. I would like to express my appreciation to Prof. Masatomo Yashima and Assistant Prof. Kotaro Fujii for their cooperation with sample characterization and meaningful discussion. I would like to express my thank to Prof. Toru Ishigaki and Associate Prof. Akinori Hoshikawa of Ibaraki University for the assistance in the neutron diffraction measurements. I am grateful for the computational calculation support from Dr. Mitsutake Oshikiri and his kindly hospitality during an internship at National Institute for Materials Science (NIMS). I wish to express my thank to staff members of the Center of Advanced Materials Analysis at the Tokyo Institute of Technology for helpful cooperation with sample characterization. And I also would like to express my appreciate to Associate Prof. Pornapa Sujaridworakun who recommended me to take a doctoral degree in Nakajima-Matsushita at Tokyo Institute of Technology.

I give my thanks to all member in Nakajima-Matsushita Laboratory for their hospitality, friendship, opinions and advices. Many thanks to all of my Thai Tokodai friends who always support each other. I also would like to thank my family for their support and encouragement.

Finally, I would like to express my deeply appreciation to MEXT scholarship. The scholarship covers tuition fees and living expenses for full time while living in Japan.

June 2019

Noppakhate JIRABORVORNPONGSA